Influence of RF heating and MHD instabilities on the fast-ion distribution in ASDEX Upgrade

Markus Weiland

München 2016

Influence of RF heating and MHD instabilities on the fast-ion distribution in ASDEX Upgrade

Markus Weiland

Dissertation

der Fakultät für Physik
der Ludwig-Maximilians-Universität München

durchgeführt am
Max–Planck–Institut für Plasmaphysik,
Garching bei München

vorgelegt von
Markus Weiland
aus München

München, den 29. Januar 2016

Prüfungsvorsitz:	Prof. Dr. Andreas Burkert
Erstgutachter:	Prof. Dr. Hartmut Zohm
Zweitgutachter:	Prof. Dr. Harald Lesch
weiterer Prüfer:	Prof. Dr. Piero Martin

Tag der mündlichen Prüfung: 7. Juni 2016

Zusammenfassung

Schnelle, supra-thermische Ionen stellen einen leistungsstarken Mechanismus zur Plasmaheizung dar. Durch Coulombstöße geben sie ihre Energie an das Hauptplasma ab, während sie selbst abgebremst werden. In aktuellen Plasmaexperimenten werden schnelle Ionen durch Neutralteilcheninjektion und Ionenzyklotronresonanzheizung (ICRH) erzeugt. In zukünftigen Fusionsreaktoren wird das selbstständige Brennen des gezündeten Plasmas durch schnelle α-Ionen aus Fusionsreaktionen ermöglicht. Darüberhinaus können schnelle Ionen benutzt werden, um Plasmastrom und -rotation zu treiben. Für den Erfolg zukünftiger Fusionsanlagen (wie ITER und DEMO) ist es daher entscheidend, die Physik schneller Ionen zu verstehen, um deren sicheren Einschluss zu gewährleisten.

Die vorliegende Arbeit beschäftigt sich mit theoretischen und experimentellen Aspekten. Ein Modell zur raschen Berechnung der Verteilungsfunktion schneller Ionen wurde entwickelt, basierend auf einer Kombination bereits existierender Codes und analytischen Lösungen. Der vergleichsweise niedrige numerische Aufwand ermöglicht es, die Verteilungsfunktion der schnellen Ionen für viele Plasmaentladungen zu rechnen, was dazu benutzt wird, um die Rekonstruktion des Plasmagleichgewichts zu verbessern.

Die experimentellen Untersuchungen zur Physik schneller Ionen wurden am Tokamak ASDEX Upgrade mittels einer FIDA (Fast Ion D-Alpha) Diagnostik durchgeführt. Diese Diagnostikmethode benutzt Ladungsaustauschreaktionen, um die Ionen unter Beibehaltung ihres Impulses in neutrale Atome umzuwandeln. Deren Lichtemission wird durch optische Elemente in der Maschine gesammelt und mit Spektrometern analysiert. Im Spektrum erkennt man schnelle Ionen an ihrer starken Doppler-Verschiebung und die Form des Spektrums erlaubt Rückschlüsse über die Geschwindigkeitsverteilung. Da die Doppler-Verschiebung durch eine Projektion des Ionengeschwindigkeitsvektors auf die Sichtlinie gegeben ist, sind Sichtlinien aus verschiedenen Beobachtungsrichtungen nötig, um den ganzen Geschwindigkeitsraum abzudecken. Deshalb wurde die FIDA Diagnostik von drei auf fünf Sichtliniengruppen ausgebaut und das Spektrometer wurde modifiziert, um eine gleichzeitige Beobachtung von blau- und rotverschobenem Licht zu ermöglichen. Diese Erweiterungen erlauben es, die 2D Geschwindigkeitsverteilung der schnellen Ionen an mehreren wohldefinierten Messpositionen tomografisch zu rekonstruieren.

Diese erweiterten Möglichkeiten werden benutzt, um den Transport schneller Ionen durch Plasmainstabilitäten zu untersuchen. Die Geschwindigkeitsabhängigkeit der Umverteilung während Sägezahninstabilitäten wurde gemessen. Es zeigt sich, dass schnelle Ionen mit hohem Geschwindigkeitsanteil senkrecht zum Magnetfeld schwächer umverteilt werden als andere schnelle Ionen, und physikalische Erklärungen hierfür werden diskutiert. Ferner wird der Transport schneller Ionen durch Alfvén Eigenmoden (AE) untersucht, wobei signifikante Umverteilung durch eine AE Kaskade gefunden wird.

Darüber hinaus wird die Beschleunigung von schnellen Deuteriumionen durch ICRH an der zweiten Harmonischen der Zyklotronfrequenz untersucht. Dies ist ein wichtiges Thema für zukünftige Fusionsanlagen, in denen Absorption der zweiten Harmonischen als ICRH-Schema geplant ist – im Gegensatz zu heutigen Anlagen, die Absorption der Grundfrequenz durch eine Plasmaminorität benutzen. Die physikalischen Grundlagen dieses zukünftigen ICRH-Schemas müssen daher untersucht und verstanden werden, um sicherzustellen, das theoretische Vorhersagen für ITER korrekt sind. Untersuchungen mit der FIDA-Tomografie zeigen Hochenergieanteile in der Verteilungsfunktion, die durch Absorption der zweiten Harmonischen erklärt werden können, und Vergleiche mit theoretischen Modellen werden diskutiert.

Abstract

Fast, supra-thermal ions provide a powerful mechanism to heat fusion plasmas. Through Coulomb collisions with the thermal bulk plasma, they slow down and transfer their energy to the plasma. In present-day devices, fast ions are generated by neutral beam injection (NBI) and ion cyclotron resonance heating (ICRH). In future fusion reactors, the dominant heating source, which allows the ignition of a burning plasma, will be fast α-particles resulting from fusion reactions. In addition to plasma heating, fast ions can be utilized to drive plasma currents and rotation. It is therefore crucial for the success of future fusion devices (such as ITER and DEMO) to understand the physics of fast ions and ensure their safe confinement.

This thesis focuses both on modeling and experimental aspects. A model to calculate the NBI fast-ion distribution rapidly has been developed. It is based on a combination of existing codes and analytic solutions. Due to the comparably low numerical effort, it can be used to calculate the fast-ion distribution in a large set of discharges, which is used to e.g. improve plasma equilibrium reconstructions.

Experimentally, the physics of fast ions is investigated at the tokamak ASDEX Upgrade, using a FIDA (Fast-Ion D-Alpha) spectroscopy diagnostic. This diagnostic technique is based on charge-exchange reactions, that convert the ions into neutral atoms (keeping their momenta). The light emission from these neutral atoms can be collected by optics in the machine and analyzed with spectrometers. Here, the fast-ion contribution can be identified due to large Doppler shifts, and the shape of the spectrum yields information about the velocity distribution. The Doppler shift is given by a projection of the ion velocity vector onto the line of sight, such that observation from different viewing angles is needed to cover the entire velocity space. Therefore, the FIDA diagnostic has been upgraded from three viewing arrays to five, and the spectrometer has been redesigned to measure blue and red Doppler shifts simultaneously. These upgrades allow a tomographic reconstruction of the 2D fast-ion velocity distribution at several well-defined measurement positions. The tomography has been successfully tested analyzing different fast-ion populations in plasmas free of instabilities.

These enhanced diagnostic capabilities are used to study fast-ion transport caused by plasma instabilities. In particular, the velocity-space dependence of the fast-ion redistribution during sawtooth crashes is investigated. It is found, that fast ions with high velocity components perpendicular to the magnetic field are less affected by sawtooth crashes than other fast ions, and theoretical explanations for these observations are discussed. In addition, radial redistribution by Alfvén eigenmodes is analyzed. Significant radial fast-ion redistribution is found in the presence of a reversed-shear Alfvén eigenmode cascade.

Furthermore, the acceleration of fast deuterium beam ions by 2nd harmonic ion cyclotron heating is investigated. This is important, because future fusion devices are foreseen to use 2nd harmonic absorption as heating scheme, in contrast to 1st harmonic minority ICRH, which is used in most present-day devices. Hence, the physic principles of 2nd harmonic absorption must be investigated and well understood in order to ensure, that theoretical predictions for e.g. ITER are correct. In the tomographic reconstruction of FIDA signals, clear high energy tails due to 2nd harmonic ICRH are seen, and comparisons to theoretical codes are presented.

Contents

1 Introduction

The ambitious goal of nuclear fusion research is to establish a new, clean and widely available energy source. In order to fuse two atomic nuclei, it is necessary to overcome the Coulomb barrier, i.e. the electro-static repulsion of the positively charged nuclei. The most promising fusion reaction is the fusion of the hydrogen isotopes deuterium and tritium. It has the highest reaction cross-section, and the reactivity peaks already at comparably low energies of 70 keV. Such energies can be reached easily with particle accelerators, but net energy production is not possible in that way, because the cross-section for elastic collisions is orders of magnitude larger than the cross-section for fusion reactions. Thus, a concept is needed, where the particles that underwent an elastic collisions are not lost but remain in the system: A confinement in a thermal ensemble is needed. Typical necessary temperatures are then in the range of about 200 million degrees Celsius, such that a conventional confinement by a material is not possible.

Besides inertial confinement, the confinement with magnetic fields is the most promising and best developed approach at present. Here, it is exploited that light elements are fully ionized at such high temperatures. A so-called plasma arises: A state of matter where the electrons and ions move freely. In total, the plasma is neutral (which is called quasi-neutrality), but each individual particle (with charge q) is influenced by magnetic ($\vec{B}$) and electric ($\vec{E}$) fields via the Lorentz force $\vec{F} = q(\vec{E} + \vec{v} \times \vec{B})$. In a magnetic field, the Lorentz force forces charged particles to gyrate (i.e. circulate) around the magnetic field line. Thus, magnetic fields can be used to guide plasma particles.

The tokamak principle

The best developed principle for magnetic confinement is the tokamak, whose basic layout is shown in figure 1.1. The magnetic field lines are closed by bending them toroidally. This prevents particle losses as they occur at the boundaries of simpler, linear devices. The main magnetic field in the toroidal direction is produced by magnetic field coils. For the confinement to work, an additional poloidal field is needed to compensate particle drifts that arise due to the toroidal curvature. This poloidal field is created by a plasma current $\vec{j}$, which flows in the toroidal direction and has to be induced by a central transformer coil located in the middle of the torus. The superposition of both field components results in helically twisted field lines, which lie in nested surfaces that are called flux surfaces. The innermost surface in this set of nested surfaces degenerates into a toroidally bent line, which is called the magnetic axis or plasma center. To quantify the (inverse) strength of field line twisting, the so-called safety factor q is introduced. It is defined as ratio of toroidal turns M and poloidal turns N of a field-line:

$$q = \lim_{M \to \infty} \frac{M}{N} \tag{1.1}$$

q can be interpreted as inverse field line slope with respect to the toroidal direction. I.e., $q = \infty$ would correspond to a pure toroidal field, and $q = 0$ to a pure poloidal field.

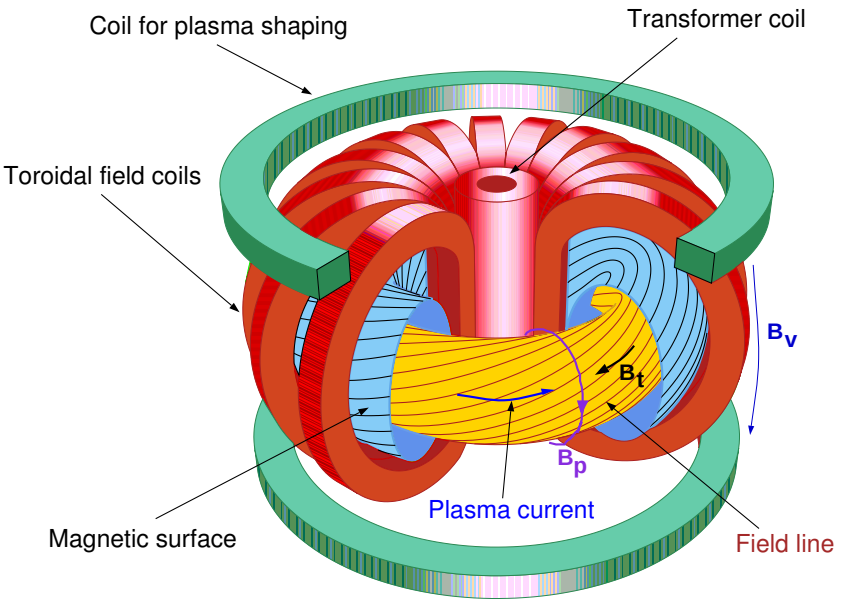

Figure 1.1: Illustration of the tokamak concept. The typical orientations of the plasma current and the poloidal and toroidal field (B_p and B_t) at ASDEX Upgrade are shown. The yellow and blue surfaces illustrate two nested flux surfaces. [1]

Plasma confinement and equilibrium

A magnetically confined plasma can be described as a conducting fluid, which interacts with the electro-magnetic fields. The corresponding physical theory is called magneto-hydrodynamics (MHD) and its basic equations are derived by combining the basic equations of hydrodynamics with the Maxwell equations. In this fluid picture, the plasma has a pressure p. The magnetic field $\vec{B}$ prevents the plasma from expanding and has to balance this pressure. This results in an equilibrium, for which the (ideal) MHD equations simplify to:

$$\nabla p = \vec{j} \times \vec{B} \tag{1.2}$$

$$\nabla \times \vec{B} = \mu_0 \vec{j} \tag{1.3}$$

$$\nabla \cdot \vec{B} = 0 \tag{1.4}$$

From eq. (1.2), it can be inferred directly that $\vec{B} \cdot \vec{\nabla} p = 0$ and hence the pressure is constant on field lines and flux surfaces. Perpendicular to the flux surfaces, however, a pressure gradient can be sustained. This is the essence of magnetic confinement, because it allows to separate a hot, dense plasma in the core of the machine from a colder, thinner plasma close to the walls, which can be handled by conventional materials then.

The constancy of the pressure (and other quantities) on flux surfaces motivates to define a radial coordinate based on these flux surfaces. Therefore, the toroidal and poloidal fluxes are introduced:

$$\Pi = \int_{A_\mathrm{tor}} \vec{B} \cdot \mathrm{d}\vec{A}, \quad \Psi = \int_{A_\mathrm{pol}} \vec{B} \cdot \mathrm{d}\vec{A} \tag{1.5}$$

They are given by an integral of the magnetic flux density $\vec{B}$ over specially defined surfaces A_tor and A_pol. These surfaces are sketched in fig. 1.2: A_tor is the surface in the

poloidal plane, containing the magnetic axis and limited by the given flux surface. In contrast, A_{pol} is the surface in the midplane (i.e. the toroidal plane at the height of the magnetic axis), which contains the center of the torus ($R = 0$) and is limited by the given flux surface. In doing so, each flux surface can be addressed with a unique label (e.g. either Π or Ψ). Consequently, the pressure p can be written as a function of these fluxes, e.g. $p = p(\Psi)$. It should be noted, that also different conventions exist, which result in prefactors or different signs of the two fluxes.

In practice, it is more convenient to have a normalized radius from 0 (plasma center) to 1 (last closed flux surface). From the above mentioned fluxes, such normalized flux radii are defined as:

$$\rho_{\mathrm{tor}} = \sqrt{\frac{\Pi - \Pi_0}{\Pi_1 - \Pi_0}}, \quad \rho_{\mathrm{pol}} = \sqrt{\frac{\Psi - \Psi_0}{\Psi_1 - \Psi_0}} \tag{1.6}$$

whereby the indexes 0,1 stand for the values at the magnetic axis and last closed flux surface, respectively. The square root can be motivated to get something similar to the minor radius of a torus, since the surface A_{tor} increases approximately with the square of the minor radius.

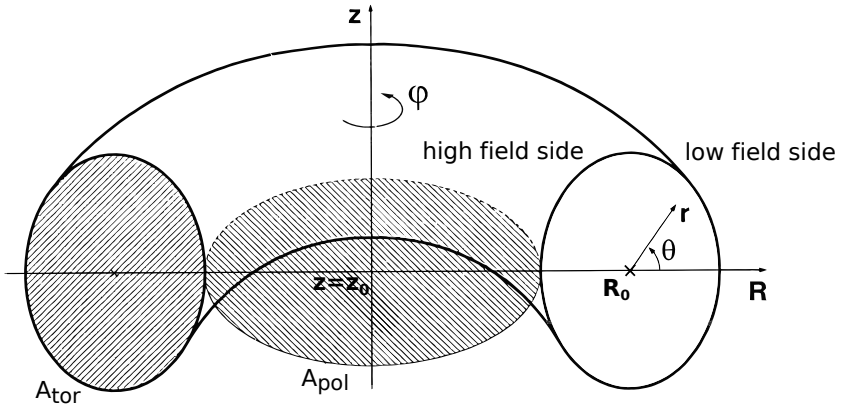

Figure 1.2: Integration surfaces A_{tor} and A_{pol} for a given flux surface. In addition, the spatial coordinates used in this thesis are shown. R and r are called major and minor radius, respectively. The magnetic axis is located at ($R = R_0$, $z = z_0$) and marked with a cross. φ is the toroidal and θ the poloidal angle. The vacuum toroidal field has a $1/R$-dependence, which is why the fraction of the torus inside the magnetic axis is called high field side (HFS) and the fraction outside of it is called low field side (LFS). Figure adapted from [2].

In similarity to the magnetic fluxes, also integrals over the current density $\vec{j}$ along the surfaces A_{pol} and A_{tor} can be defined. In the following, we will consider the poloidal current function:

$$I = \mu_0 \int_{A_{\mathrm{pol}}} \vec{j} \cdot \mathrm{d}\vec{A} \tag{1.7}$$

It can be used to write the magnetic field $\vec{B}$ of a tokamak in the following form:

$$\vec{B} = \vec{B}_{\mathrm{pol}} + \vec{B}_{\mathrm{tor}} = \nabla\Psi \times \nabla\varphi + I\nabla\varphi \tag{1.8}$$

This corresponds to a sum of poloidal and toroidal field components and fulfills Maxwell's equations (1.3-1.4). φ is the toroidal angle as shown in fig. 1.2. It should be noted, that

the definition of I (1.7) contains integration over the current flowing in the toroidal field coils. In the zero plasma pressure limit it follows that $I = const$ inside the toroidal field coils, which leads to the $1/R$ decay of the toroidal vacuum field (since $\nabla\varphi = \hat{e}_\varphi/R$).

Inserting equations (1.8) and (1.3) into (1.2) leads then to a single scalar equation describing the plasma equilibrium, the *Grad-Shafranov-Schlüter equation*: [3, 4]

$$\Delta^*\Psi = \left(R\frac{\partial}{\partial R}\frac{1}{R}\frac{\partial}{\partial R} + \frac{\partial^2}{\partial z^2}\right)\Psi = -R^2\mu_0\frac{\mathrm{d}p}{\mathrm{d}\Psi} - I\frac{\mathrm{d}I}{\mathrm{d}\Psi} \tag{1.9}$$

In this context, both p and I are seen as functions of the poloidal flux Ψ. The equation can be solved then for the 2D poloidal flux function $\Psi(R, z)$, which is done routinely at ASDEX Upgrade e.g. by the CLISTE code [5].

Plasma heating and fast ions

The tokamak concept provides an intrinsic source of plasma heating: The induced plasma current flows against the plasma resistance, which results in ohmic plasma heating. However, the plasma resistance decreases with plasma temperature (it is proportional to $T^{-3/2}$). Hence, ohmic heating is useful for the early plasma start-up, but to reach temperatures significantly higher than ≈1 keV, additional heating mechanisms are needed.

In an ignited fusion reactor, the main heating will come from the 3.5 MeV α-ions, which result from the fusion reaction and are still bound to the magnetic field (unlike the also produced neutrons). The fast α-ions will collide with the thermal bulk plasma particles, and thereby slow down until they are thermalized themselves. At the same time, the bulk plasma gains energy from those collisions and is heated.

In order to reach the state of ignition, a fusion reactor will need external heating. Present-day experiments avoid the usage of radioactive tritium, such that they do not have significant fusion heating, but rely entirely on external heating methods to achieve research-relevant plasma conditions. The most common methods are heating by electromagnetic waves and neutral beam injection (NBI).

In NBI heating, energetic neutral atoms, that are not bound to the magnetic field and travel in straight lines, are injected into the plasma. The injection energy needs to be much higher than thermal energies. In present-day medium sized tokamaks, it lies e.g. in typical ranges of 50-100 keV. On their path through the plasma, the neutrals are ionized trough charge exchange and ionization processes, such that they become fast ions. Similar to the fast α-particles, these fast ions provide heating to the bulk plasma by collisional slowing down.

Electro-magnetic waves can be tuned to several resonances in the plasma to achieve plasma heating. Very commonly used resonances are harmonics of the electron cyclotron frequency (electron cyclotron resonance heating, ECRH) and harmonics of the ion cyclotron frequency (ion cyclotron resonance heating, ICRH). During ICRH, resonant ions are accelerated by absorbing the wave. This results again in a population of fast, suprathermal particles, that heat the bulk plasma through collisions. The steady-state ion distribution is determined by a balance between the acceleration through the wave and the slowing down through collisions.

Apart from plasma heating, fast ions (as created e.g. by NBI or ICRH) can impose a torque on the main plasma. The resulting toroidal rotation can have beneficial effects

on the plasma confinement. In addition, if the fast ions fly mainly in one direction, they carry a net current, which can be used to drive plasma currents non-inductively (provided that the ion current is not fully shielded by electrons).

Motivation

These mechanisms work only efficiently, if the fast ions are well confined. In particular, the ignition of a fusion reactor relies on good confinement of the fusion α particles. In addition, strong losses of fast ions might cause severe damages to the first wall, such that they must be avoided. Hence, the physics of fast-ion confinement must be well understood to ensure the success of future fusion devices such as ITER and DEMO.

In general, confining fast ions is more challenging than thermal ions, because the orbit size (i.e. excursions from the average flux-surface position) increases with the ion velocity. At a certain velocity, these orbit widths may become even comparable with machine dimensions, such that a closed orbit is not possible anymore without intersecting with the first wall. But even for ions with lower velocities the chances that an ion gets on a non-confined orbit are higher for fast than for thermal ions.

In addition, the interaction between fast ions and MHD plasma instabilities, such as sawtooth crashes or Alfvén eigenmodes, is an interesting and ongoing subject of research. Fast ions can drive these instabilities or stabilize them, and get redistributed by them. In particular, this redistribution must be understood well, to avoid losses or redistribution towards undesired plasma regions.

But also the fast-ion generation itself is an ongoing field of research, in particular, the physics of ion cyclotron resonance heating (ICRH). Most present-day fusion devices use an ICRH scheme, where a plasma minority species (i.e. hydrogen) is resonant at the fundamental ion cyclotron frequency. In future fusion devices, this hydrogen-minority heating scheme cannot be applied, because the fusion α-particles would also be resonant (at the second harmonic), and further acceleration of αs must be avoided. Therefore it is forseen that ITER utilizes a heating scheme, where a majority ion species (tritium) is heated directly by second harmonic heating. The 2nd harmonic absorption is however (in contrast to fundamental absorption) only effective for fast ions with large Larmor radii. To ensure the success of ITER, it is therefore necessary to study and understand these physics aspects of second harmonic ICRH. In particular, codes which are used for predictions of ITER must be validated.

To study the fast-ion distribution experimentally, the six dimensional fast-ion phase space needs to be observed (with three spatial and three velocity coordinates). In a tokamak, this phase space can be typically considered to be axisymetric in real space and symmetric with respect to the gyro-angle in velocity space, which reduces the phase space dimension to four.

Fast-ion diagostics

Several techniques exist to study the fast-ion phase space such as neutral particle analyzers (NPA) [6], gamma ray tomography [7], collective Thomson scattering (CTS) [8], neutron spectroscopy (NESP) [9] and fast-ion D-alpha (FIDA) [10] measurements. In addition, the distribution of lost fast ions can be measured with fast-ion loss detectors (FILD) [11]. The FIDA technique is the main diagnostic tool used in this thesis. It is based

on the spectroscopic observation of line radiation that emerges after charge exchange reactions. Here, the fast ions can be distinguished from the thermal particles through the strong Doppler shift of the associated emission wavelength. Radial profiles of the FIDA emission can be measured and compared to theoretical predictions by forward-modeling with FIDASIM [12, 13].

An analysis of the whole FIDA Doppler spectrum yields information about the 2D velocity distribution $f(E, v_\parallel/v)$, where E is the energy and $v_\parallel/v$ is the pitch of the fast ions. The observed Doppler-shift of an ion is proportional to the projection of its velocity vector (after neutralization) onto the line of sight direction. Therefore, the FIDA spectrum of a line of sight with angle Φ to the magnetic field is dominated by fast-ions with similar pitch angles (i.e. $\cos(v_\parallel/v) \approx \Phi$). Observation from different viewing angles allows consequently a tomographic reconstruction of $f(E, v_\parallel/v)$.

This thesis

This thesis has been carried out at the ASDEX Upgrade tokamak. The experiment and plasma diagnostics used in this thesis are introduced in chapter 3.

In the framework of this thesis, the FIDA diagnostic at ASDEX Upgrade has received several upgrades. The spectrometer was redesigned to allow a measurement of the full D_α spectrum (i.e. blue and red Doppler shifts) permanently and under all plasma conditions. Furthermore, the FIDA diagnostic has been extended from three to five viewing arrays for a better coverage of the velocity space. These enhanced diagnostic capabilities allow to reconstruct the fast-ion velocity distribution at several radial positions by tomographic inversion of the FIDA raw data. The details of the diagnostic and the tomography are described in chapter 4.

In chapter 5, applications of the FIDA tomography are presented. In section 5.1, its velocity space accuracy is demonstrated by analyzing data in the presence of 60 keV and 93 keV NBI. In section 5.2, the fast-ion redistribution in the velocity space induced by a sawtooth crash is studied using all five FIDA views at two positions, in- and outside of the sawtooth inversion. Section 5.3 focuses on fast-ion redistribution due to Alfvén eigenmodes. In Section 5.4, we use the FIDA tomography to analyze the fast-ion distributions resulting from 2nd harmonic ICRH of deuterium beam ions.

As a side project, a model to calculate the NBI fast-ion distribution rapidly has been implemented, based on FIDASIM and an analytic solution of the Fokker-Planck-equation. The model delivers as output important profiles like the fast-ion pressure and driven current, but also the fast-ion distribution on request. The rather small numerical effort allows to run the model for larger sets of discharges and it is in use to improve equilibrium reconstructions. Further applications of the model could invoke a data-base like comparison between FIDA signals and theoretical predictions. The principles of this model are explained in detail in chapter 2, which should also serve as an introduction into the basic physics of the fast-ion slowing down process. In the second half of chapter 2, we explain the basic physics of ICRH and the resulting fast-ion distributions.

2 Fast-ion physics

2.1 The fast-ion distribution function

The distribution of fast ions is in general described by a 6D phase-space density $f(\vec{x}, \vec{v})$. In SI-Units, f has the dimension $[\,\mathrm{m}^{-3}(\frac{\mathrm{m}}{\mathrm{s}})^{-3}]$, i.e. it describes how many particles are found in a certain real-space and velocity space volume. In tokamak plasmas, two symmetries can be exploited to reduce the 6D distribution into 4D. Firstly, the axisymmetry of the torus allows to leave out the dependence on the toroidal angle φ. Hence, the real-space dependence of f can e.g. be written in terms of major radius R and vertical coordinate z or of a flux label (e.g. ρ_{tor}) and the poloidal angle θ. The second symmetry of the system is the gyromotion of the ions. A velocity vector can be decomposed into its motion parallel to the field lines $v_\parallel$ and perpendicular to them $v_\perp$:

$$\vec{v} = v_\parallel \hat{e}_\parallel + v_\perp \cdot (\cos\gamma \hat{e}_{\perp 1} + \sin\gamma \hat{e}_{\perp 2}) \tag{2.1}$$

Here, $\hat{e}_\parallel = \mathrm{sgn}(\hat{e}_\varphi \cdot \vec{B}) \frac{\vec{B}}{|\vec{B}|}$ is a unit vector parallel to the magnetic field, and $\hat{e}_{\perp 1,2}$ are unit vectors perpendicular to $\hat{e}_\parallel$ and $\hat{e}_{\perp 2,1}$. The orientation of $\hat{e}_\parallel$ is defined such that it points in the same direction as the toroidal angle $\hat{e}_\varphi$.

The standard ASDEX Upgrade field configuration features the following orientations: $\vec{B} \propto -\hat{e}_\varphi$ and $\vec{j} \propto +\hat{e}_\varphi$. Then, $v_\parallel > 0$ corresponds to co-current motion and vice versa. γ is the phase of the gyromotion with angular frequency ω_{c}:

$$\gamma = \omega_{\mathrm{c}} t \text{ with: } \omega_{\mathrm{c}} = \frac{qB}{m} \tag{2.2}$$

Here, m is the mass and q the charge of the ion. Under typical tokamak conditions, the magnetic field B can be assumed to be approximately constant during a gyroorbit (precise conditions are discussed later in eq. (2.47)). Then, the motion of a given fast-ion is fully described by $v_\parallel$, $v_\perp$ and the particle distribution is symmetric with respect to γ. In conclusion, the 6D fast-ion distribution, e.g. $f(R, \varphi, z, v_\perp, \gamma, v_\parallel)$, is symmetric with respect to φ and γ and can hence be written as a 4D function $f(R, z, v_\perp, v_\parallel)$.

In the following, we want to focus now on different velocity space coordinates, i.e. discuss the (3D) velocity space at a fixed spatial location. Mathematically, $(v_\perp, \gamma, v_\parallel)$ are cylindrical coordinates where $v_\perp \in [0; +\infty]$ has the role of a radius, $\gamma \in [0; 2\pi]$ is the polar angle and $v_\parallel \in [-\infty; +\infty]$ the height. The gyromotion can be interpreted as a rotational symmetry of the 3D velocity space around the $v_\parallel$-axis. Another coordinate system, which exploits rotational symmetry are spherical coordinates. They can be defined by taking:

$$\text{the total velocity } v = \sqrt{v_\perp^2 + v_\parallel^2} \text{ as radial coordinate,} \tag{2.3}$$

$$\text{the pitch angle } \theta_v = \arccos\frac{v_\parallel}{v} \text{ as azimuthal angle from } [0, \pi] \text{ and} \tag{2.4}$$

$$\text{the gyro angle } \gamma \text{ as polar angle from } [0, 2\pi]. \tag{2.5}$$

It can be convenient, to substitute v with the particle energy $E = \frac{1}{2}mv^2$: E can be directly compared to temperatures or the acceleration voltage and injection energy of the NBI. We will mainly use the energy E and the pitch $\xi := v_\parallel / v$ as velocity space coordinates.

Integration in velocity space

Integration over the velocity space coordinates is trivial for $(v_\parallel,\ v_\perp)$ and $(v,\ \theta_v)$ coordinates, because they form (together with γ) cylindrical and spherical coordinates, for which the Jacobians are well known:

$$\iiint f \,\mathrm{d}^3\vec{v} = \int_0^{+\infty}\int_{-\infty}^{+\infty} f(v_\perp, v_\parallel)\, 2\pi v_\perp \mathrm{d}v_\parallel \mathrm{d}v_\perp = \int_0^{+\infty}\int_{-\frac{\pi}{2}}^{+\frac{\pi}{2}} f(v,\theta_v)\, 2\pi v^2 \sin\theta_v \mathrm{d}\theta_v \mathrm{d}v = n_\mathrm{fi}$$

The result of the integration is the (spatial) fast-ion density n_fi. The Jacobian of (E, ξ) can be computed considering:

$$\begin{aligned}
\mathrm{d}v &= \frac{\partial v}{\partial E}\mathrm{d}E = \frac{1}{mv}\mathrm{d}E = \frac{1}{\sqrt{2Em}}\mathrm{d}E \\
\mathrm{d}\theta_v &= \frac{\partial \theta_v}{\partial \xi}\mathrm{d}\xi = -\frac{1}{\sin\theta_v}\mathrm{d}\xi \\
\iiint f \,\mathrm{d}^3\vec{v} &= \int_0^{+\infty}\int_{-1}^{+1} f(v,\xi)\, 2\pi v^2 \frac{1}{\sqrt{2Em}}\mathrm{d}\xi\mathrm{d}E = \int_0^{+\infty}\int_{-1}^{+1} f(v,\xi)\, 2\pi \frac{\sqrt{2E}}{m^{3/2}}\mathrm{d}\xi\mathrm{d}E
\end{aligned}$$

It can be convenient, to write a distribution function F including the Jacobian, eg:

$$F(E,\xi) = 2\pi\frac{\sqrt{2E}}{m^{3/2}} \cdot f(E,\xi), \text{ or:} \tag{2.6}$$

$$F_v(v,\xi) = 2\pi v^2 \cdot f(v,\xi) \tag{2.7}$$

$F(E,\xi)$ can than be interpreted more directly, as it gives the ion density at certain energy E and pitch ξ. Consequently, F has then units of $[1/\mathrm{m}^3/\mathrm{eV}]$.

Example: Shifted Maxwell-Boltzmann distribution

As an example, we consider a shifted Maxwellian-Boltzmann distribution. This is useful to describe the thermal distribution of the bulk plasma ions: They have a thermal (Maxwell-Boltzmann) distribution in the plasma frame, however the plasma is typically rotating in the toroidal direction with an angular frequency ω_rot. In the laboratory (i.e. torus hall) frame, this corresponds to a shifted Maxwell-Boltzmann distribution:

$$f(v_\parallel, v_\perp) = n_\mathrm{D}\sqrt{\left(\frac{m}{2\pi T_\mathrm{i}}\right)^3} \cdot \exp\left(-m\frac{(v_\parallel - v_{\mathrm{rot}\parallel})^2 + v_\perp^2}{2T_\mathrm{i}}\right) \text{ with: } v_{\mathrm{rot}\parallel} = \frac{|\vec{B}\cdot\hat{e}_\varphi|}{|\vec{B}|}\omega_\mathrm{rot}R \tag{2.8}$$

Here (and throughout this thesis), we use the common convention that the Boltzmann constant k_B is equal to one and hence temperatures have the unit of an energy (e.g. J or

eV). f corresponds to the usual Boltzmann-factor $e^{-E/T}$, with E being the kinetic energy in the plasma frame. This can be transformed into F by multiplying with the Jacobian:

$$F(E,\xi) = \frac{n_\mathrm{D}}{T_\mathrm{i}^{3/2}}\sqrt{\frac{E}{\pi}} \cdot \exp\left(-m\frac{(v_\parallel - v_{\mathrm{rot}\parallel})^2 + v_\perp^2}{2T_\mathrm{i}}\right) \tag{2.9}$$

and using:

$$v_\parallel = \sqrt{\frac{2E}{m}} \cdot \xi \qquad v_\perp = \sqrt{\frac{2E}{m}} \cdot \sqrt{1-\xi^2}. \tag{2.10}$$

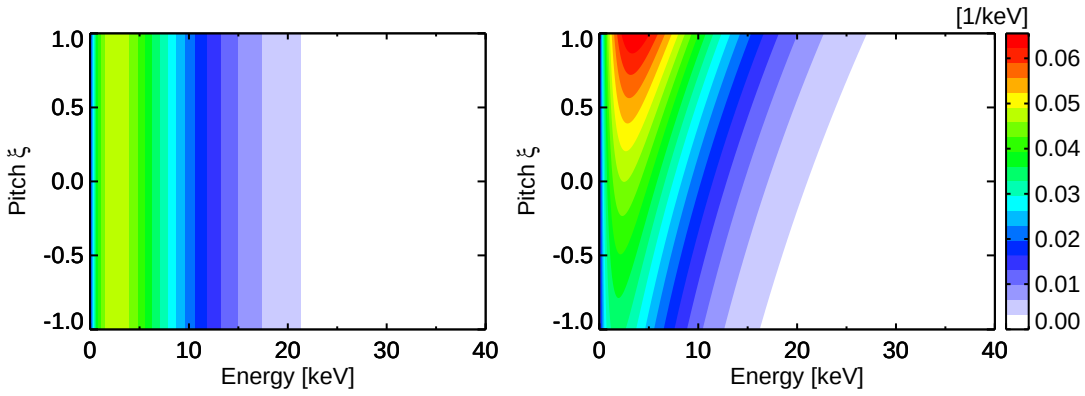

(a) $v_{\mathrm{rot}\parallel} = 0$ **(b)** $v_{\mathrm{rot}\parallel} = 160\ \frac{\mathrm{km}}{\mathrm{s}}$

Figure 2.1: Shifted Maxwell-Boltzmann distribution with $T_\mathrm{i} = 5$ keV, $n_\mathrm{D} = 1$ and two rotation velocities. The rotation velocity in (b) corresponds to a rotation frequency of 15 kHz at $R = 1.7$ m

Figure 2.1 shows two contour plots of F with parameters given in the figure subscription. With $v_\mathrm{rot} = 0$, F is an isotropic Maxwell-Boltzmann distribution, and the contour lines are parallel to the y-axis (fig. 2.1a). With finite v_rot, the distribution function is no longer isotropic in the laboratory frame, and the contour lines are enhanced (i.e. tilted) towards the direction of the rotation (fig. 2.1b).

2.2 The Fokker-Planck equation

2.2.1 Preliminary Considerations

The Fokker-Planck equation describes the physics of fast ions in the velocity space, i.e. the collisions with thermal bulk ions and electrons. These collisions cause momentum and energy transfer between thermal particles and fast ions: The fast ions slow down, and at the same time, the bulk plasma gets heated. Furthermore, the direction of the fast-ion velocity vectors may change during the collisions, which is called *pitch-angle scattering*. Since electrons have a much lower mass, pitch angle scattering is weak for collisions between electrons and ions, and it is much stronger for ion-ion collisions.

Whether a fast ion collides dominantly with electrons or with ions is mainly determined by the relative velocity between the colliding particles. The Coulomb collisions are most effective (i.e. they cause a large interchange of momentum and energy), when

this relative velocity is low, i.e. the colliding particles have comparable velocities. Then, the particles have more time $\mathrm{d}t$ to interact via the Coulomb force $\vec{F}$, which results in a larger momentum transfer $\mathrm{d}\vec{p}$, since:

$$\mathrm{d}\vec{p} = \vec{F}\mathrm{d}t \tag{2.11}$$

Typically, bulk electrons and ions have comparable temperatures in tokamak plasmas. The most probable velocity of thermal particles is given by:

$$v_{\mathrm{e,i}} = \sqrt{\frac{2T}{m_{\mathrm{e,i}}}} \tag{2.12}$$

which means that thermal electrons have much higher velocities (by a factor of $\approx \sqrt{2 \cdot 1836} \approx 61$) than thermal deuterons. Consequently, fast ions above a certain critical velocity v_{c} (or critical energy $E_{\mathrm{c}} = \frac{1}{2}mv_{\mathrm{c}}^2$) collide dominantly with electrons, while fast ions slower than v_{c} collide dominantly with thermal ions. A formula for E_{c} has been derived in [14] in the limit that (electron thermal velocity) $\gg$ (fast-ion velocity) $\gg$ (ion thermal velocity):

$$E_{\mathrm{c}} = 14.8 \cdot T_e \cdot A_{\mathrm{fi}} \cdot \left(\frac{1}{n_{\mathrm{e}}} \sum_j \frac{n_j Z_j^2}{Aj}) \right)^{2/3} \tag{2.13}$$

Herein, a plasma with several ion species j with density n_j, charge Z_j and atomic mass number A_j is considered. The subscript $()_{\mathrm{fi}}$ denotes the fast-ion species. If all ion species have the same charge-to-mass ratio (Z/A), the sum can be simplified to:

$$E_{\mathrm{c}} = 14.8 \cdot T_e \cdot A_{\mathrm{fi}} \cdot (Z/A)^{2/3} \tag{2.14}$$

which gives for deuterium NBI into a pure deuterium plasma:

$$E_{\mathrm{c}} = 18.6 \cdot T_e \tag{2.15}$$

The fact that these equations depend on T_{e} but not on T_{i} resembles the assumption that the thermal ion velocity can be neglected compared to the electrons.

Drifts and diffusion in velocity space

In the following section, we want to sketch, how the slowing-down and pitch angle scattering can be described mathematically. While this cannot deliver a rigid derivation of the Fokker-Planck equation, it should at least help to understand the different terms within.

The slowing down of fast ions due to the drag force with thermal particles corresponds to a drift of the distribution function towards lower velocities. This is equivalent with a directional flow $\vec{\Gamma} \propto -\hat{e}_v$ in the velocity space. This flow should conserve the number of particles, and hence has to fulfill the continuity equation for the distribution function f:

$$\frac{\partial f}{\partial t} = -\nabla \cdot \vec{\Gamma} + \sigma \tag{2.16}$$

where the ∇-operator is acting in the velocity space and σ describes particle sources and sinks. Hence, the temporal evolution of f due to slowing-down of fast ions is connected with a first derivative in velocity space.

The value of $\vec{\Gamma}$ can be calculated from a formula given in [14], where the average energy loss rate $\frac{\mathrm{d}E}{\mathrm{d}t}$ of a test fast-ion is given:

$$\frac{\mathrm{d}E}{\mathrm{d}t} = -\frac{2}{\tau_\mathrm{s}} \cdot \frac{E_c^{3/2} + E^{3/2}}{\sqrt{E}} \tag{2.17}$$

with the Spitzer time τ_s:

$$\tau_\mathrm{S} = 6.27 \cdot 10^8 \cdot \frac{A}{Z^2 \ln\Lambda} \cdot \frac{(T_\mathrm{e}\,[\mathrm{eV}])^{3/2}}{n_\mathrm{e}\,[\mathrm{cm}^{-3}]}\ \ \mathrm{s} \tag{2.18}$$

and the Coulomb logarithm [15]:

$$\ln\Lambda \approx 24 - \ln\sqrt{n_\mathrm{e}\,[\mathrm{cm}^{-3}]} + \ln T_\mathrm{e}\,[\mathrm{eV}] \tag{2.19}$$

Equation (2.17) is particularly useful, because it can be used to calculate the *slowing down time*, i.e. the time it takes for a fast ion with energy E to slow down (here: to zero velocity):

$$t_\mathrm{sd} = \frac{\tau_\mathrm{s}}{3} \cdot \ln\left(1 + \left(\frac{E}{E_\mathrm{c}}\right)^{3/2}\right) \tag{2.20}$$

For a fixed fast-ion species and injection energy τ_s is proportional to $T_\mathrm{e}^{3/2}/n_\mathrm{e}$ (neglecting the weak dependence of $\ln\Lambda$ on T_e and n_e). The argument of ln() contains an opposite T_e dependence, since $E_\mathrm{c}^{-3/2} \propto T_\mathrm{e}^{-3/2}$, but in total, the slowing down time increases with increasing T_e. Hence, slowing down times are long in hot and thin plasma regions and short in cold, dense plasma regions. Thus, the slowing down time is typically longer in the hot plasma core, than in the cold outer plasma.

Inversion of equation 2.20 delivers the (average) temporal evolution of the fast-ion energy $E(t)$. It is shown in figure 2.2 for for three representative values of electron density and temperature in a pure D plasma. The last case with lowest T_e corresponds to a typical situation in the plasma edge, while the other two cases are meant to illustrate typical core parameters at ASDEX Upgrade. The slowing down times for 60 keV fast ions are indicated with arrows.

Equation 2.17 can now be used to calculate the velocity space flow $\vec{\Gamma}$:

$$\vec{\Gamma} = \frac{\mathrm{d}v}{\mathrm{d}t} f \hat{e}_v = \frac{\mathrm{d}E}{\mathrm{d}t}\frac{\mathrm{d}v}{\mathrm{d}E}\hat{e}_v = -\frac{1}{\tau_\mathrm{s}}\frac{v_\mathrm{c}^3 + v^3}{v^2} f \hat{e}_v \tag{2.21}$$

Plugging this result into the continuity equation and using the ∇-operator for spherical coordinates, one obtains:

$$\frac{\partial f}{\partial t} = \frac{1}{\tau_\mathrm{s} v^2}\frac{\partial}{\partial v}\left(\left(v_\mathrm{c}^3 + v^3\right) f\right) + \sigma \tag{2.22}$$

i.e. a differential equation describing the temporal evolution of f due to drag as a drift in velocity space.

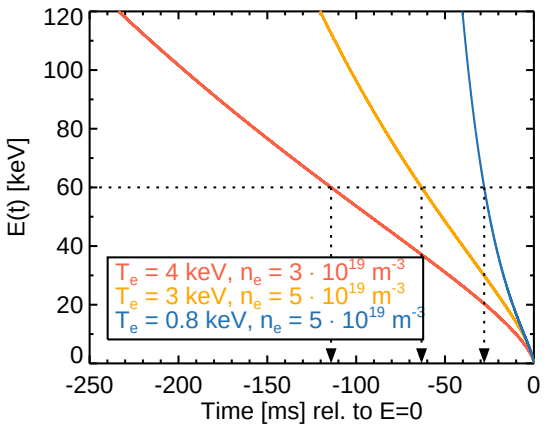

Figure 2.2: Average temporal evolution of a test fast-ion during its slowing down process, for three representative values of electron density and temperature in a pure D plasma. The last case with lowest T_e corresponds to a typical situation in the plasma edge, while the other two cases are meant to illustrate typical core parameters at ASDEX Upgrade. The slowing down times for 60 keV fast ions are indicated with arrows. Here, we plot the slowing down process until $E = 0$. Realistically, the slowing down process should stop when the E reaches T_i. In general, eq. 2.17 was derived assuming (fast-ion velocity) $\gg$ (ion thermal velocity), which is no longer fulfilled when $E \approx T_i$.

In contrast, pitch angle scattering is a diffusive process. An initially well-defined pitch distribution (e.g. a δ-function) will be broadened by collisions. Mathematically, diffusion can be described with the first Fick's law:

$$\vec{\Gamma} = -D\nabla f \tag{2.23}$$

where D is a (non-negative) diffusion constant. This means that the flow resulting from diffusion is proportional to the gradient of f. For a very peaked f, diffusion will be strong and hence it will cause a flattening of f. If no other processes are involved, this will continue until eventually a flat distribution is reached ($\nabla f = 0$) and hence the diffusion flow $\vec{\Gamma}$ is zero. Again, the diffusion has to fulfil the continuity equation:

$$\frac{\partial f}{\partial t} = -\nabla \cdot \vec{\Gamma} = \nabla(D \cdot \nabla f) + \sigma \tag{2.24}$$

and it can be seen that diffusion is described with two derivatives in velocity space.

2.2.2 The Fokker-Planck equation

In general, the term *Fokker-Planck equation* describes the temporal evolution of a probability distribution f under the impact of a drift and diffusion. As motivated in the previous section, this phenomenology matches the physics of fast-ion collisions in plasmas. The Fokker-Planck equation for the collisions of fast ions with bulk plasma is given by: [16, 17]

$$\frac{1}{\tau_s v^2}\frac{\partial}{\partial v}[(v^3 + v_c^3)f] + \frac{\beta}{\tau_s}\frac{v_c^3}{v^3}\frac{\partial}{\partial \xi}(1-\xi^2)\frac{\partial f}{\partial \xi} + \frac{1}{\tau_s v^2}\frac{\partial}{\partial v}\left[\left(\frac{T_e}{m_{fi}}v^2 + \frac{T_i}{m_{fi}}\frac{v_c^3}{v}\right)\frac{\partial f}{\partial v}\right] = \\ = \frac{\partial f}{\partial t} - \sigma \tag{2.25}$$

The left hand side represents the collision operator $\hat{C}(f)$. It is itself constituted of three terms:

The first term contains one derivative with respect to velocity and consequently describes the slowing down of fast ions towards lower energies as a drift.

The second term contains the second derivative with respect to the pitch, and hence describes a diffusive process: the pitch angle scattering. The prefactor β is given by

$$\beta = \frac{Z_{\text{eff}} m_{\text{i}}}{2 m_{\text{fi}}} \tag{2.26}$$

where m_{fi} is the mass of the considered fast-ion species (in the case of NBI, the mass of the injected ions). Furthermore, the term is proportional to v_{c}^3/v^3, which resembles the fact that pitch angle scattering is strong for collisions with ions ($v \ll v_{\text{c}}$) and weak for collisions with electrons ($v \gg v_{\text{c}}$).

The third term contains the second derivative with respect to the velocity, and hence describes a diffusion in the velocity direction. This velocity diffusion expresses the fact, that not all collisions cause a slowing down of the fast ion, but there are also some collisions which accelerate a given fast ion (e.g. a collision with a thermal ion from the high-energy tail of the Maxwell distribution). On average, the collisions will slow the fast ion down (i.e. a drift covered by the first term), but the deviations from this average are covered by this diffusion term. Under typical conditions, this third term is less important than the first two. The most prominent feature resulting from it is a small high energy tail above the injection energy of NBI, while without velocity diffusion no particles can exist above the injection speed.

Apart from the collision operator $\hat{C}(f)$, many other terms can be added to the left side of the Fokker-Planck equation to enhance the physical model [16, 18], e.g.:

- $\dfrac{-1}{\tau_{\text{cx}}(v)} f$ Losses due to charge exchange (i.e. neutralization of fast ions with rate τ_{cx})
- $-\dfrac{Z_{\text{fi}} e |\vec{E}| \eta}{m_{\text{fi}}} \left(\xi \dfrac{\partial f}{\partial v} + \dfrac{1-\xi^2}{v} \dfrac{\partial f}{\partial \xi} \right)$ Effect of a parallel electric field $|\vec{E}|$ (e.g. induced by the loop voltage) - partially shielded by the electrons (factor η, see eq. 2.63).

Furthermore, the collision operator presented here neglects spatial effects (e.g. particle trapping), and those effects can be taken into account by adding higher-order terms [18]. Collisions between fast ions are neglected as-well, and only collisions between fast ions and the bulk plasma are considered.

Ion cyclotron resonance heating can be described by an additional operator $\hat{Q}_{\text{RF}}(f)$ (on the left hand side of the Fokker-Planck equation (2.25)), which is discussed in section 2.4.1. In contrast to that, NBI and fast α-particles from fusion reactions can be modeled by using an appropriate source/sink term σ on the right hand side. Both act as a source of fast ions with distinct velocity and pitch distribution: In the case of NBI, the velocity is given by the injection energy and the pitch distribution by the geometry of the beam. α-particles from fusion reactions are isotropic, and their energy distribution is defined by the fusion reaction yield (plus the center of mass energy of the reactancs).

There are many numerical codes, which simulate the fast-ion slowing down very sophisticatedly, including all the mentioned effects and many more (e.g. toroidal field ripple)

- for example the TRANSP/NUBEAM code [17, 19, 20], which uses a Monte Carlo approach. However, increasing accuracy comes also with increasing complexity and calculation time. Sometimes, quicker calculations making acceptable approximations are needed. In particular for routine calculations of the fast-ion slowing down distribution including many time points and discharges, calculations are needed that require less computational efforts. We will therefore discuss an analytic solution of the Fokker-Planck equation in the presence of NBI in the next section, and show that it covers the most important physical aspects by a comparison with TRANSP/NUBEAM.

2.2.3 Modeling the NBI fast-ion distribution function

In the following, we will discuss an analytic solution of the Fokker-Planck equation in the presence of NBI, as it was derived in [16]. Therefore, we must define an appropriate source term σ, which we will motivate in the next section.

The NBI source term

NBI acts as a source of fast ions: A beam of initially neutral particles is injected with a well-defined velocity. As the beam propagates through the plasma, neutral particles from the beam collide with plasma particles and get ionized by electron/ion impact ionization or charge-exchange reactions. Thus, a former neutral particle has become a fast ion, and is now bound to the magnetic field. This leads to an attenuation of the beam. Since there is almost no momentum transfer during charge exchange reactions, the new-born fast ion keeps the same pitch $\xi = v_\parallel/v$ and velocity as the initial neutral particle.

We parametrize the NBI source term by:

$$\sigma = \frac{S}{2\pi v^2}\delta(v - v_0)K(\xi) \tag{2.27}$$

The injection velocity v_0 is assumed to be mono-energetic. The typically three energy components (comp. section 3.2.1) of a beam can be modeled by summation, then. A broad pitch distribution $K(\xi)$ (e.g. due to the broadening of the beam) can be taken into account. The normalization is defined such, that $\int K(\xi)\mathrm{d}\xi = 1$ and thus $\iiint \sigma \mathrm{d}^3\vec{v} = S$. Hence, S is the fast-ion birth (or deposition) per volume and time (e.g. in units of $[1/\mathrm{m}^3/\mathrm{s}]$).

The solution

We will discuss now the steady-state analytical solution of the Fokker-Planck equation (2.25) with the NBI source term (2.27), as it was derived in [16]. In steady state, $\frac{\partial f}{\partial t} = 0$. The pitch-angle scattering operator has the shape of Legendre's differential equation:

$$\frac{\partial}{\partial \xi}(1 - \xi^2)\frac{\partial}{\partial \xi}P_n(\xi) = -n(n+1)P_n(\xi) \tag{2.28}$$

which is solved by Legendre polynomials $P_n(\xi)$. This motivates to expand the solution of the Fokker-Planck equation in a series of Legendre polynomials. The solution is then given by:

$$f(v,\xi) = \frac{1}{2\pi}\frac{S\cdot\tau_\mathrm{S}}{v^3 + v_\mathrm{C}^3}\cdot\sum_{n=0}^{\infty}\left(n+\tfrac{1}{2}\right)u^{n(n+1)}P_n(\xi)K_n\cdot\exp[-g(v)H(v-v_0)] \tag{2.29}$$

with:

$$K_n = \int K(\xi) P_n(\xi)\, \mathrm{d}\xi \tag{2.30}$$

$$u = \left(\frac{v_0^3 + v_\mathrm{C}^3}{v^3 + v_\mathrm{C}^3} \frac{v^3}{v_0^3} \right)^{\pm\beta/3}, \text{ where } \pm \text{ corresponds to } \begin{matrix} v < v_0 \\ v \geq v_0 \end{matrix} . \tag{2.31}$$

H is the Heaviside function, and $g(v)$ is a function describing the high energetic tail above injection velocity due to velocity diffusion. This influences only a small part of the velocity space. Within our model, we will neglect this part and set $g(v) = 0$.

Example for one injection energy component

To illustrate the properties of the analytical solution, we will discuss a basic example. We set the injection energy to $E_0 = 59\,\mathrm{keV}$ and assume a narrow pitch distribution $K(\xi) = \delta(\xi - 0.5)$. These values represent the properties of NBI Q3 at ASDEX Upgrade in the plasma center, using deuterium injection (although the beam has a wider pitch distribution in reality). The fast-ion birth rate S is taken from a TRANSP run of discharge #29783 at 3.44 s. A contour plot of the solution (transformed to $F(E, \xi)$) is shown in fig. 2.3a with $T_\mathrm{e} = 2.83\,\mathrm{keV}$ and $n_\mathrm{e} = 5.97 \cdot 10^{19}\mathrm{m}^{-3}$ (corresponding to the plasma center). The injection position of the NBI can be clearly identified, as it marks the maximum of F. Since we study the steady state solution, the NBI is assumed to inject fast ions permanently.

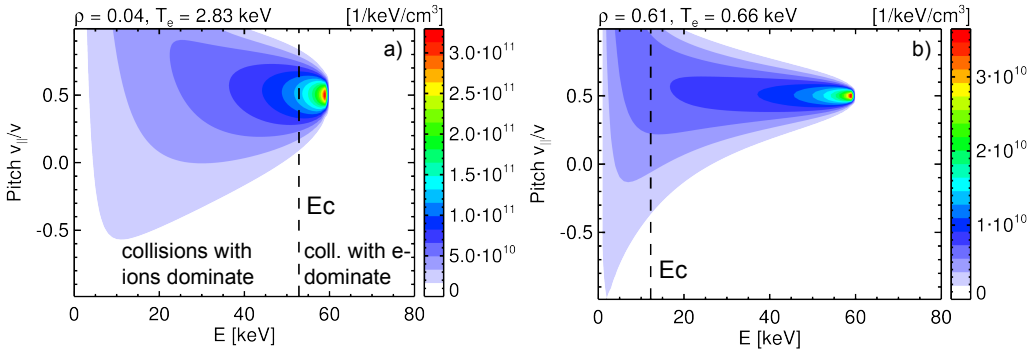

Figure 2.3: Solution (2.29) of the Fokker-Planck equation (2.25) with a point-like source of fast ions ($E_0 = 59\,\mathrm{keV}, \xi_0 = 0.5$), for two different electron temperatures. The critical energy is shown with a dashed line.

For comparison, the critical energy E_c is marked with a dashed line and it can be seen, that it lies only closely underneath the injection energy in this case. Below E_c, collisions with ions dominate during slowing down, and hence pitch angle scattering is strong in this case. The initially well defined injection pitch angle (a δ-function) is strongly broadened towards lower energies (i.e. after suffering more collisions). The high ratio of $E_\mathrm{c}/E_0 \gg 0.5$ means also, that dominantly ions are heated by the NBI in this case.

The solution for the same birth rate S, but lower T_e and n_e corresponding to the outer plasma at $\rho_\mathrm{tor} = 0.61$ is shown in fig. 2.3b. Due to lower T_e, the critical energy is much lower than the injection energy. Hence, collisions with electrons dominate, leading to dominant electron heating and weak pitch angle scattering in this case. It can also be

seen, that the total fast-ion density, given by $\iint F(E,\xi)\mathrm{d}E\mathrm{d}\xi$, is lower here, because the slowing down time is shorter.

Example with all three energy components

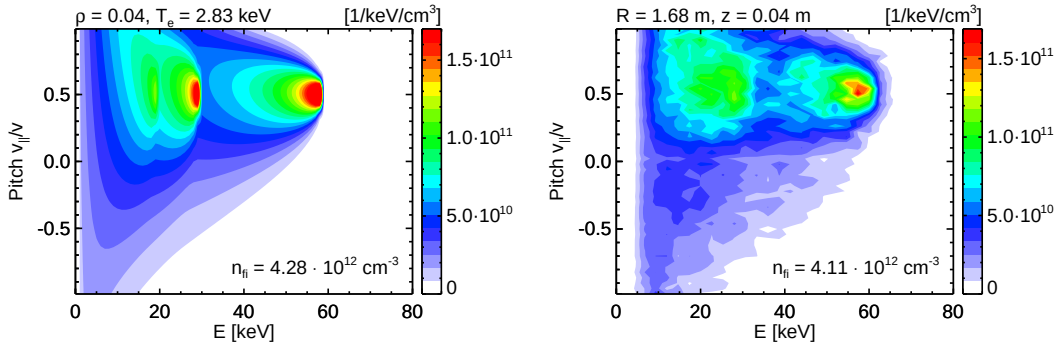

(a) Model **(b)** TRANSP

Figure 2.4: (a) Solution of the Fokker-Planck equation (2.25) using three injection energies. **(b)** Calculated TRANSP fast-ion velocity distribution in the plasma center.

For H or D injection, a single neutral injection beam at ASDEX Upgrade is consisting of three energy components (see section 3.2.1). In terms of the acceleration voltage U, those are given by eU, $eU/2$ and $eU/3$, i.e. they represent the full, half and third nominal injection energy. Since we neglect collisions between fast ions themselves, the full distribution function can be modeled as a sum of the different injection energies. An example in the plasma center is shown in fig. 2.4a. Again, the birth rates $S_{1,2,3}$ for the three energy components are taken from TRANSP. For comparison, the fast-ion distribution calculated by TRANSP is shown in fig. 2.4b, and it can be seen that the overall shape matches well. The noisy appearance of the TRANSP simulation results from the MC approach. For a more quantitative comparison, we have integrated over the pitch and plotted the resulting energy profile in fig. 2.5a. Again, the basic shape matches well. The different energy steps due to the three energy components are very clearly visible in the analytical solution. In the TRANSP solution, they are a little bit more smeared out, because TRANSP takes also the velocity diffusion into account, which we have neglected so far (by setting $g(v) = 0$ in eq. (2.29)).

The effect of the velocity diffusion is seen most clearly in the high energy tail above the largest injection energy, which is missing in the analytical solution. In [21], a convenient analytic expression is given for the slope of this tail. It can be derived from the Fokker-Planck equation (2.25) for $v > v_0$, if f is averaged over the pitch ξ (such that the pitch-angle scattering operator drops out). It is given by:

$$f \propto \exp\left(-\frac{E}{T_{\mathrm{eff}}}\right) \quad \text{with:} \quad T_{\mathrm{eff}} = \frac{T_{\mathrm{i}} + (\frac{E}{E_{\mathrm{c}}})^{3/2} T_{\mathrm{e}}}{1 + (\frac{E}{E_{\mathrm{c}}})^{3/2}} \tag{2.32}$$

The formula in [21] contains also a term taking into account acceleration due to an external electrical field, which we have left out here, to see the pure effect of velocity diffusion.

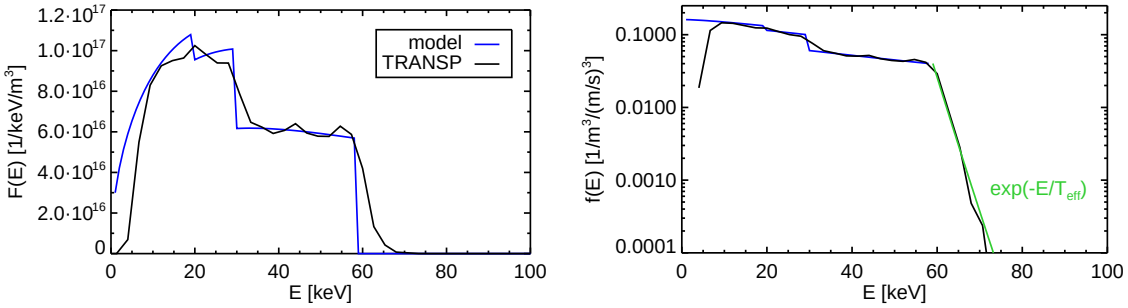

(a) $\int F \mathrm{d}\xi$ **(b)** f averaged over ξ

Figure 2.5: Comparison between the calculated TRANSP and model fast-ion distribution. TRANSP stops the simulation of fast-ion Monte Carlo Markers, when their energy is below $3/2\,T_\mathrm{i}$. Comparing the blue curves, the main difference between f and $F \propto \sqrt{E} f$ can be seen: F goes to zero for $E = 0$, because the volume in velocity space is small around the origin.

In order to compare this formula to the TRANSP simulation, we have plotted $f(E)$ (i.e. f averaged over ξ) in fig. 2.5b on a logarithmic scale. The term $\exp(-E/T_\mathrm{eff})$ is added to the analytical solution in a continuous way at the highest injection energy. It can be seen that a very good agreement in the slope is found with respect to the TRANSP result.

2.2.4 Calculation of profiles

For many applications, profile information about the fast-ion distribution are important. For example, knowing the fast-ion pressure profile and current drive profile can help to improve the reconstruction of magnetic equilibria. Calculating profiles in terms of ρ_pol or ρ_tor is equivalent to an average over the poloidal angle θ - and it is justified, because fast-ion distributions typically vary much stronger in the radial than in the poloidal directions.

The deposition profile

If we want to calculate a flux surface averaged fast-ion distribution $f(E, \xi, \rho)$ with the analytic formulas described in the previous sections, a flux surface averaged source term profile is needed. For a first try we will use:

$$\sigma(\rho) = \frac{S(\rho)}{2\pi v^2} \delta(v - v_0) \delta(\xi - 0.5) \tag{2.33}$$

and hence neglect that the angle between the B-field and the beam (i.e. the pitch of deposited fast ions) changes slightly on its way through the plasma. $S(\rho)$ is called *deposition profile* or *birth profile*, and it can be calculated fast e.g. with FIDASIM [12, 13] or SINBAD [22], and it is also calculated by TRANSP/NUBEAM.

Fig. 2.6(a) shows the calculated birth profiles for each energy component. The total ratio of the three energy components is determined by the technical details of the NBI ion source. From the shape of the birth profiles, it can be seen that the highest energy component is most strongly peaked. In the plasma center, the full energy component

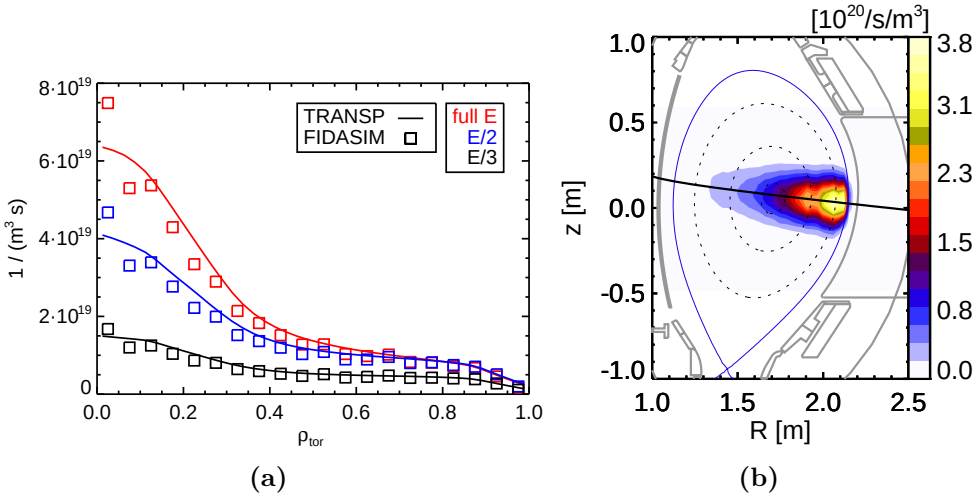

Figure 2.6: Fast-ion birth positions calculated by FIDASIM. **(a)** Radial profiles for each energy component and comparison to TRANSP calculation. **(b)** Poloidal contour plot. The solid black line shows the center of the beam.

is clearly dominant, while in the outer plasma, full and half energy components equal each other. The reason for this is that faster neutrals have a larger mean free path when travelling through the plasma, i.e. they get ionized less probably. Hence, they penetrate more deeply into the plasma leading to a stronger deposition close to the plasma center.

In Fig. 2.6(b) a poloidal contour of the deposition rate is shown. The finite width of the beam is well visible. Also it can be seen that the global maximum of deposition is located closely to the separatrix, because the beam is not yet strongly attenuated there. On the further path through the plasma, the attenuation causes an approximatly exponential decay of the beam, then. The reason, why this 2D contour still transforms into peaked deposition profiles, is an effect of the differential volume $\mathrm{d}V/\mathrm{d}\rho$ of the flux surfaces. In the outer part, e.g. where the global maximum of the deposition is located, the beam covers only a small part of the flux surfaces, and the deposition has to be equally distributed over the large flux surface. Close to the plasma center, flux surfaces are in contrast fully covered by the beam and in the mapping to a birth profile, this results then in a strong peak.

Fast-ion profiles

With the flux-surface averaged deposition profiles $S_{1,2,3}(\rho)$ for the three energy components, it is straightforward to calculate a flux surface averaged fast-ion distribution function $f(E, \xi, \rho)$. Of course, this approach uses the strong approximation that, during the slowing down-process, the fast ions stay on the flux surface they were born into. I.e., the ion orbits are assumed to have zero width and radial transport is not considered.

To make a comparison with TRANSP, we compute the fast-ion density profile

$$n_{\mathrm{fi}} = \iint F(E, \xi)\, \mathrm{d}E \mathrm{d}\xi \tag{2.34}$$

and the fast-ion pressure in the perpendicular and parallel direction

$$p_\perp = \iint E \cdot (1-\xi^2) \cdot F(E,\xi)\,\mathrm{d}E\mathrm{d}\xi \tag{2.35}$$

$$p_\parallel = 2\iint E \cdot \xi^2 \cdot F(E,\xi)\,\mathrm{d}E\mathrm{d}\xi \tag{2.36}$$

whereby the total fast-ion pressure is given by

$$p = \frac{1}{3}p_\parallel + \frac{2}{3}p_\perp = \frac{2}{3}\iint E \cdot F(E,\xi)\,\mathrm{d}E\mathrm{d}\xi = \frac{2}{3}\langle E\rangle\, n_{\mathrm{fi}}. \tag{2.37}$$

The different prefactors in $p_\perp$ and $p_\parallel$ originate from the fact that the perpendicular direction is associated with two degrees of freedom and the parallel direction with one degree of freedom.

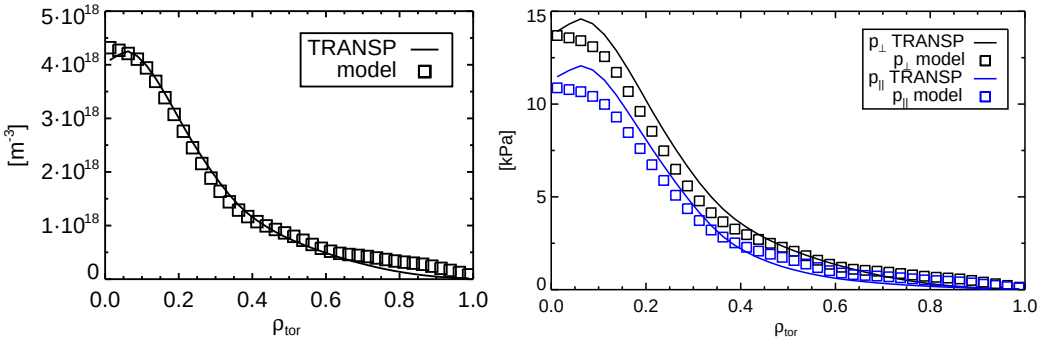

(a) Fast-ion density **(b)** Fast-ion pressure

Figure 2.7: Modeled fast-ion profiles in comparison to TRANSP.

The calculated profiles are shown in fig. 2.7. It can be seen, that very good agreement is found for the fast-ion density in the plasma center. However, towards the edge an over-estimation is found. Although the absolute values are low in this region, the relative error is big ($\approx$ a factor of 2 at $\rho_{\mathrm{tor}} = 0.8$) and the volume within this region is large, making these deviations even more problematic.

The same trend is seen in the pressure profile. In general, the agreement in the plasma center is little worse, and our model calculates slightly lower pressures than TRANSP. This might be explainable due to our neglection of the high energy tail above the injection energy due to velocity diffusion. This high energy tail is more important for the pressure calculation than for the density, because of the multiplication with E in eq. (2.35). Nevertheless, the relative error in the plasma center is small and the agreement can be considered as sufficient. However, towards the edge a similar strong relative over-estimation is found as for the density.

In the next sections, we will show, that these deviations are mainly caused by the fast-ion orbits, which we have not considered up to now. Therefore, we will discuss the physics of ion orbits in the following, and then describe how we include their effect into our model.

2.3 Ion Orbits

In this section, the properties of ion orbits in tokamak field configurations are discussed. Hereby, we will focus on the movement of the guiding center (i.e. the center of the gyromotion), and derive the constants of motion using Lagrangian mechanics.

2.3.1 Lagrangian and adiabatic invariants

The Lagrangian $\mathcal{L}$ for a charged particle with mass m and charge q in a magnetic field $\vec{B}$ with vector potential $\vec{A}$ and an electrical field $\vec{E}$ with potential Φ is given by:

$$\mathcal{L} = \frac{1}{2} m \dot{\vec{x}}^2 + q \dot{\vec{x}} \cdot \vec{A}(\vec{x}) - q\Phi(\vec{x}) \tag{2.38}$$

Hereby, $\vec{x}$ and $\dot{\vec{x}}$ are the particle position and velocity, respectively. Noether's theorem states, that every symmetry of $\mathcal{L}$ is connected to a conservation law. This can be seen directly from the Euler-Lagrange equation for the coordinate x_i:

$$\frac{\mathrm{d}}{\mathrm{d}t} \frac{\partial \mathcal{L}}{\partial \dot{x}_i} = \frac{\partial \mathcal{L}}{\partial x_i} \tag{2.39}$$

If $\mathcal{L}$ is symmetric with respect to x_i, then $\frac{\partial \mathcal{L}}{\partial x_i} = 0$ and hence

$$P_i = \frac{\partial \mathcal{L}}{\partial \dot{x}_i} \tag{2.40}$$

is a constant of motion. In general, P_i is called the canonical momentum (of the coordinate x_i).

In the case of tokamak plasmas, two symmetries exist: the gyromotion and the toroidal symmetry. Those result in two constants of motion, which we will derive in the following.

Conservation of the magnetic moment

In the following, we will show that gyromotion is associated with a constant of motion, if the magnetic field can be assumed to be constant during the gyromotion. Therefore, we will use a cylindrical coordinate system (r, γ, z), with the guiding center located at $r = 0$. We assume a homogeneous magnetic field in the z-direction $\vec{B} = -B\hat{e}_z$ and the absence of electrical fields. Hence, the gyration takes place in the z-plane, with γ being the gyro-phase. Then, the Lagrangian is given by:

$$\mathcal{L} = \frac{1}{2} m \dot{z}^2 + \frac{1}{2} m r_{\mathrm{L}}^2 \dot{\gamma}^2 + q r_{\mathrm{L}} \dot{\gamma} A_\gamma \tag{2.41}$$

with the Larmor-radius

$$r_{\mathrm{L}} = \frac{m v_\perp}{|q|\, B} \tag{2.42}$$

and the angular gyrofrequency

$$\dot{\gamma} = \frac{qB}{m} \ . \tag{2.43}$$

The vector potential $\vec{A}$ can be calculated from $\vec{B}$ using $\vec{B} = \mathrm{rot}\,\vec{A}$ and Stoke's theorem and after a short calculation one gets:

$$\vec{A} = -\frac{Br}{2}\hat{e}_\gamma \tag{2.44}$$

Since we have assumed that $\vec{B}$ is homogeneous, the Lagrangian does not depend on γ. Thus, the Euler-Lagrange equation for γ reads:

$$\frac{\mathrm{d}}{\mathrm{d}t}\frac{\partial \mathcal{L}}{\partial \dot{\gamma}} = \frac{\partial \mathcal{L}}{\partial \gamma} = 0 \tag{2.45}$$

The canonical momentum $P_\gamma = \frac{\partial \mathcal{L}}{\partial \dot{\gamma}}$ is a constant of motion and is given by:

$$P_\gamma = \frac{\partial \mathcal{L}}{\partial \dot{\gamma}} = m r_\mathrm{L}^2 \dot{\gamma} + q r_\mathrm{L} A_\gamma = q B r_\mathrm{L}^2 - q r_\mathrm{L} \cdot \frac{B r_\mathrm{L}}{2} = \frac{1}{2} q r_\mathrm{L}^2 B = \frac{m}{q} \cdot \frac{1}{2}\frac{m v_\perp^2}{B} \equiv \frac{m}{q} \cdot \mu \tag{2.46}$$

Hereby, μ is the magnetic moment, which is created by the current of the gyrating ion. μ is a constant of motion (i.e. $\frac{\mathrm{d}\mu}{\mathrm{d}t} = 0$) if the charge of the ion q is constant.

For this derivation, we have assumed that the magnetic field is constant during the gyromotion. In a tokamak configuration, this is not exactly true. E.g., the toroidal field is decreasing with $\frac{1}{R}$. However, if the magnetic field does not vary strongly during one gyroorbit, the constancy of μ is still a very good approximation, and μ is then called an adiabatic invariant. Therefore, two conditions must be met:

$$\frac{B}{|\nabla B|} \gg r_\mathrm{L} \quad \text{and} \quad \frac{\dot{B}}{B} \ll \dot{\gamma} = \omega_\mathrm{c} \tag{2.47}$$

i.e., the spatial variation of B must be weak compared to the gyroradius, and the temporal variation must be small with respect to the gyrofrequency. The former is fulfilled easily, as the gyroradius can be considered small against machine dimensions. The second condition is obviously true in the absence of field fluctuations, but also in the case of strong MHD activity: Assuming a magnetic field of $B = 2.4$ T, the gyration period of deuterium is $\tau_\mathrm{c} = 27$ ns. For comparison, the typical time-scale of a sawtooth crash at ASDEX Upgrade is of the order of $\tau_{cr} \approx 80$ µs. During a sawtooth crash, field lines reconnect, leading to strong changes of the magnetic field. However, compared to the period of gyromotion, these changes still can be considered adiabatic and conservation of the magnetic moment is still a good approximation even in such an extreme MHD-event.

An example where the magnetic moment is not conserved is the resonance layer of ion cyclotron resonance heating (ICRH). Here, electrical and magnetic fields are used which rotate with the same frequency as the gyromotion (fundamental ICRH) or higher multiples of the gyrofrequency (higher harmonic ICRH). Hence, those changes cannot be considered adiabatic, and the magnetic moment can change.

It is remarkable that P_γ from eq. 2.46 can also be written as $P_\gamma = \frac{1}{2} m r_\mathrm{L}^2 \dot{\gamma} = \frac{1}{2} m v_\perp r_\mathrm{L}$. Besides the leading factor of $\frac{1}{2}$ this corresponds exactly to the angular momentum associated with the gyromotion. Hence, conservation of the magnetic moment can also be interpreted as conservation of the angular momentum of the gyromotion. When an ion enters a region with higher magnetic field, its Larmor radius gets smaller. This is then balanced by the ion spinning faster (i.e. increased $v_\perp$ and $\dot{\gamma}$) - just like an ice dancer is spinning faster, when he draws his arms and legs in.

Conservation of the canonical toroidal angular momentum

The second symmetry in a tokamak, which results in a conservation law, is the symmetry with respect to the toroidal angle φ. To calculate the conserved quantity, we use the common cylindrical (R, φ, z) torus coordinates. Then, the Lagrangian for the motion of the guiding center takes the form:

$$\mathcal{L} = \frac{1}{2} m R^2 \dot{\varphi}^2 + qR\dot{\varphi} A_\varphi + \dots \tag{2.48}$$

Here, we have only written the terms depending on $\dot{\varphi}$ explicitly. Obviously, $\mathcal{L}$ does not contain any term with φ, because the magnetic field and hence its vector potential $\vec{A}$ are toroidally symmetric. To calculate A_φ, we recall that the magnetic field in a tokamak can be written as sum of poloidal and toroidal field:

$$\vec{B} = \vec{B}_{\text{pol}} + \vec{B}_{\text{tor}} = \nabla\Psi \times \nabla\varphi + I\nabla\varphi \tag{2.49}$$

Hereby, Ψ denotes the poloidal flux and I the poloidal current function. The φ-component of $\vec{A}$ describes the poloidal field, and hence

$$\vec{B}_{\text{pol}} = \nabla\Psi \times \nabla\varphi = \nabla \times (A_\varphi \hat{e}_\varphi) \tag{2.50}$$

must hold. This is fulfilled by

$$A_\varphi \hat{e}_\varphi = \Psi\nabla\varphi = \frac{\Psi}{R}\hat{e}_\varphi \ . \tag{2.51}$$

The Euler-Lagrange equation gives:

$$\frac{\mathrm{d}}{\mathrm{d}t}\frac{\partial\mathcal{L}}{\partial\dot{\varphi}} = \frac{\partial\mathcal{L}}{\partial\varphi} = 0 \tag{2.52}$$

Hence, the *canonical toroidal angular momentum* $P_\varphi = \partial\mathcal{L}/\partial\dot{\varphi}$ is a constant of motion in an axisymmetric tokamak and is given by:

$$P_\varphi = \frac{\partial\mathcal{L}}{\partial\dot{\varphi}} = mR^2\dot{\varphi} + qRA_\varphi = mR^2\dot{\varphi} + q\Psi \approx mRv_\parallel + q\Psi \ . \tag{2.53}$$

The latter form can be useful to express P_φ directly in terms of $v_\parallel$, we use however the exact form for calculations.

Similar to the conservation of the magnetic moment, the conservation of P_φ is still true under small deviations from axisymmetry. However, the conditions are more strict. For example, P_φ is not conserved during sawtooth crashes. The changes in P_φ result then in a radial redistribution, i.e. a redistribution towards other flux surface with different Ψ.

Orbit calculation from the constants of motion

If collisions are neglected, then the energy E is conserved on an ion orbit, and hence it is also a constant of motion. Together with the magnetic moment and the canonical toroidal angular momentum, this results in a set of three constants of motion (COM):

$$\begin{cases} E = \frac{1}{2}m(v_\parallel^2 + v_\perp^2) = const \\ \mu = \frac{1}{2}\frac{mv_\perp^2}{B} = const \\ P_\varphi = mR\frac{B_{tor}}{B}v_\parallel + q\Psi = const \end{cases} \tag{2.54}$$

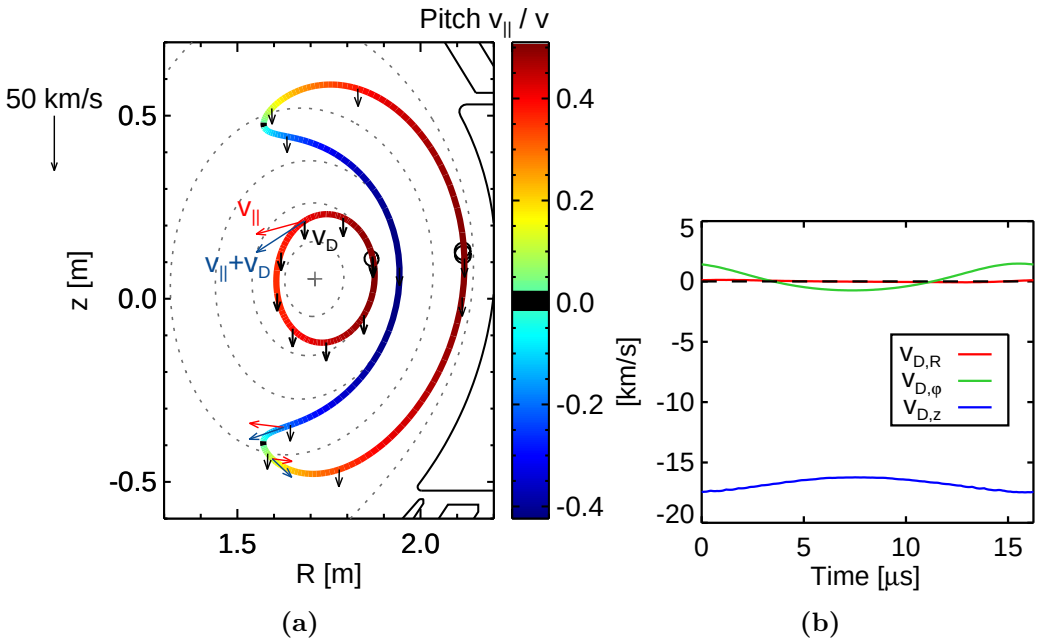

Figure 2.8: (a): Exemplaric orbit calculations for $E = 59$ keV. Two types of orbits are seen. From left two right (with respect to the midplane): A passing and a trapped orbit. The dashed lines show contours of ρ_{pol} and the magnetic axis is marked with a cross. **(b)**: Components of the drift velocity $\vec{v}_{\mathrm{D}}$ for the passing orbit in (a).

μ and P_φ depend on (R, z) through B and Ψ. Hence, this can be interpreted as a system of four variables $(R, z, v_\perp, v_\parallel)$ and three equations. If the initial values $(E_0, \mu_0, P_{\varphi 0}$ and the sign of $v_{\parallel 0})$ are known, the solution of this system is given by an one dimensional solution set: The poloidal projection of the guiding center orbit.

Figure 2.8a shows two calculated orbits for 59 keV fast ions with initial pitch $\xi_0 = 0.5$ at two different starting positions. For comparison, the first Larmor orbit is shown with a black line. We will focus now on the smaller orbit, which is started at R=1.87 m, z=0.11 m. As the fast ion propagates towards smaller R values, the magnetic field increases. Conservation of μ demands then an increase of $v_\perp$ and hence a decrease of $v_\parallel$ to conserve the energy (the pitch $\xi = v_\parallel / v$ is shown with the color scale). In total, the particle has moved to a position with lower R and lower $v_\parallel$. To ensure conservation of the canonical toroidal angular momentum P_φ, this must be balanced by a change of Ψ. In the sign convention of the CLISTE equilibrium code, which we have used here, Ψ is increasing (monotonically) from the separatrix to the magnetic axis. To keep P_φ constant, an increase of Ψ is needed, hence the particle cannot stay on its initial flux surface, but has to travel inward towards flux surfaces closer to the magnetic axis. On the way back towards large R, this behaviour reverses, and hence a closed orbit is obtained.

2.3.2 Particle drifts

Alternatively, the behavior of the orbits can be explained by particle drifts. In general, the presence of a force $\vec{F}$ results in a drift of the guiding-center with velocity:

$$\vec{v}_{\mathrm{D}} = \frac{1}{q} \frac{\vec{F} \times \vec{B}}{B^2} \tag{2.55}$$

Due to the curvature of the tokamak configuration, two forces are always present: The first is the centrifugal force, which arises because the particles have to follow the toroidally (and poloidally) curved field lines. It is given by:

$$\vec{F}_\mathrm{c} = m\frac{v_\parallel^2}{R_\mathrm{c}^2}\vec{R}_\mathrm{c} \tag{2.56}$$

Here, $\vec{R}_\mathrm{c}$ is a vector describing the field line curvature. Its length R_c is the radius of curvature and the direction is pointing outwards, away from the center of the circular arc which best approximates the field line at that point. The resulting drift is given by:

$$\vec{v}_\mathrm{D,c} = \frac{mv_\parallel^2}{q}\frac{\vec{R}_\mathrm{c}\times\vec{B}}{R_\mathrm{c}^2B^2} \tag{2.57}$$

The second force arises due to the gradient ∇B of the magnetic field strength:

$$\vec{F}_{\nabla B} = -\mu\nabla B = -\frac{1}{2}\frac{mv_\perp^2}{B}\nabla B \tag{2.58}$$

Obviously, the main cause of the magnetic field gradient ∇B is the toroidal curvature of the tokamak, because this leads to the $1/R$-decay of the vacuum toroidal field. However, there is also a small contribution to ∇B from the plasma, e.g. due to the variation of the poloidal field and the diamagnetic response of the plasma. The resulting drift is given by:

$$\vec{v}_{\mathrm{D},\nabla B} = -\frac{1}{2}\frac{mv_\perp^2}{q}\frac{\nabla B\times\vec{B}}{B^3} \tag{2.59}$$

Both drifts go approximately in the same direction and add up to a combined curvature and ∇B drift. If the contribution from the plasma is neglected (i.e. only the vacuum toroidal field is considered) ∇B can be expressed by the curvature:

$$\frac{\vec{R}_\mathrm{c}}{R_\mathrm{c}^2} = -\frac{\nabla B}{B} \tag{2.60}$$

Hence, the direction of both drifts is exactly the same, and the sum can be given in a convenient form:

$$\vec{v}_\mathrm{D} = \vec{v}_\mathrm{D,c} + \vec{v}_{\mathrm{D},\nabla B} = -\frac{m(v_\parallel + \frac{1}{2}v_\perp)}{q}\frac{\nabla B\times\vec{B}}{B^3} \tag{2.61}$$

It can be seen that these drifts can lead to charge separation, which must be avoided. In the standard ASDEX Upgrade field configuration, they point downwards for ions and upwards for electrons.

Figure 2.8b shows a numerical calculation of the three components of v_D for the left orbit in fig. 2.8a during a complete poloidal turn. It can be seen, that the z-component is clearly dominant, which also proves that the approximation made in eq. (2.61) is very good. Also it can be seen that the duration of a poloidal turn takes 16 µs for the considered orbit. This time is 3-4 orders of magnitude shorter than typical slowing down

times for 59 keV ions. Hence, it can be assumed in good approximation, that fast ions complete their first orbit (after their birth) without collisions.

In figure 2.8a the sum of both drifts is shown with black arrows. In the standard field configuration of ASDEX Upgrade, ions with $v_\parallel > 0$ move counter-clockwise in the poloidal projection. The projection of the parallel velocity into the poloidal plane is shown with a red arrow. The total velocity of the ion considered here is $v = 2.4 \cdot 10^6 \frac{\mathrm{m}}{\mathrm{s}}$ and hence two orders of magnitude larger than the drift velocity. However, the poloidal projection of $v_\parallel$ is comparable to v_D leading to significant excursion from the initial flux surface. In a tokamak field configuration, the effect of the drifts cancel along the orbit, as the ion velocity vector changes. Thus, the particle returns to its initial poloidal position and a closed orbit forms.

The strength of the curvature and ∇B drift depend on $v_\parallel^2$ and $v_\perp^2$, respectively. This means that the ratio $v_\mathrm{D}/v_\parallel$ between the drift motion and the motion parallel to field lines increases linearly with $v_\parallel$ (for fixed pitch). Hence, the influence of the drift on the particle orbit becomes more important the faster an ion is. While thermal ions move closely to the flux surfaces, fast ion orbits have much stronger excursions from the mean flux surface (also called orbit width). This makes safe confinement of fast ions more challenging, as with increasing orbit width chances increase that an orbit intersects with the wall and the ion is not confined.

2.3.3 Orbit classification

Passing orbit

The left (and smaller) orbit in fig. 2.8a which we have discussed further above as first example is called a *passing orbit*, because the particle passes the high field side on a circle-like shape. In particular, the parallel velocity does not cross zero and hence keeps its initial sign. Another important kind of orbits are *trapped orbits*, which we will discuss in the next section.

Trapped orbit

In section 2.3.1, we have seen that as a particle propagates towards regions of higher magnetic field (i.e. the high field side) the conservation of the magnetic moment μ demands an increase of $v_\perp$ at the expense of $v_\parallel$ (because $E = const$). Obviously, this process has to stop when $v_\parallel$ reaches 0 and the whole kinetic energy is stored in the gyromotion. Then, the particle cannot proceed anymore towards regions with higher magnetic field: It is *trapped* and gets reflected, the parallel velocity goes through zero and changes its sign after the reflection. An exemplaric orbit with this behavior is the right and larger orbit in figure 2.8a. The poloidal projection of the orbit has the shape of a banana, which is why trapped particles/orbits are also called banana particles/orbits. The two orbit points with the highest magnetic field (and hence $v_\parallel = 0$) are called banana tips or bouncing points. Due to the low $v_\parallel$, the particle spends a large fraction of its orbit time close to the tips.

Conservation of the angular canonical momentum demands that the parts of the banana with opposite sign of $v_\parallel$ lie on different flux surfaces Ψ. In general, it can be shown that the outer leg of the banana corresponds to co-current motion and the inner leg to

counter-current motion. This has an important consequence for neutral beam injection: If the beam is injecting co-current (as all beams on AUG), and if a newly born fast-ion is trapped, it is on the outer leg of the banana. Hence, during its orbit, it moves further into the plasma, and is well confined. If the beam is injecting counter-current, the situation is opposite, i.e. newly born trapped fast ions are on the inner leg of their banana. This has the consequence, that they travel further outwards during their first orbit, which increases the "danger" of hitting the wall and getting lost. Hence, counter-current NBI has the disadvantage that a larger fraction of the first orbits is not confined, leading to increased fast-ion prompt losses.

Stagnation orbit

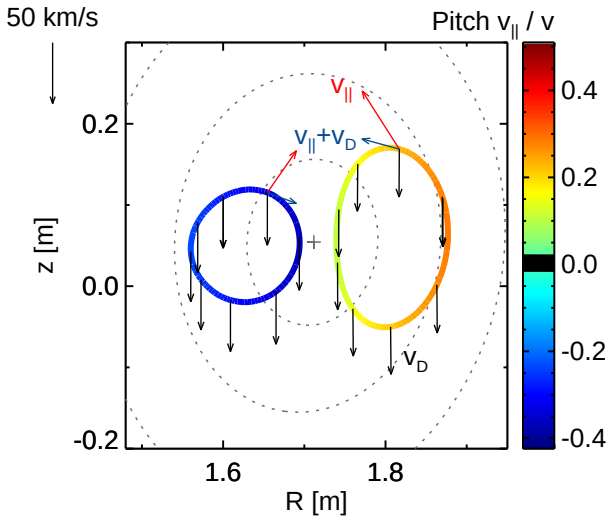

Figure 2.9: Stagnation orbits. Both ions have $E = 120$ keV. The left orbit is stagnating on the HFS and the right on the LFS. The dashed lines show contours of ρ_{pol} and the magnetic axis is marked with a cross.

Another kind of orbits are so-called *stagnation* or *potato* orbits. Like passing orbits, they do not flip the sign of $v_\parallel$, but they are in contrast not encircling the magnetic axis. Two examples with $E = 120$ keV are given in fig. 2.9. It can be seen, that for this kind of orbit, the curvature and ∇B drifts are so strong with respect to the parallel velocity, that the drift pushes the particle down before it can cross the magnetic axis. Hence, this kind of orbits are rarely encountered for slow, thermal ions but happen more often for fast ions (in particular with low absolute values of the pitch). The right orbit has $\xi > 0$ and is stagnating on the LFS, while the left orbit has $\xi < 0$ and is stagnating on the HFS.

2.3.4 Taking orbit effects into account

In the following section, we want to discuss how an orbit effect correction can be taken into account in our analytical model. To motivate our approach, we study the calculated NBI distribution from TRANSP, which has all those effects taken into account.

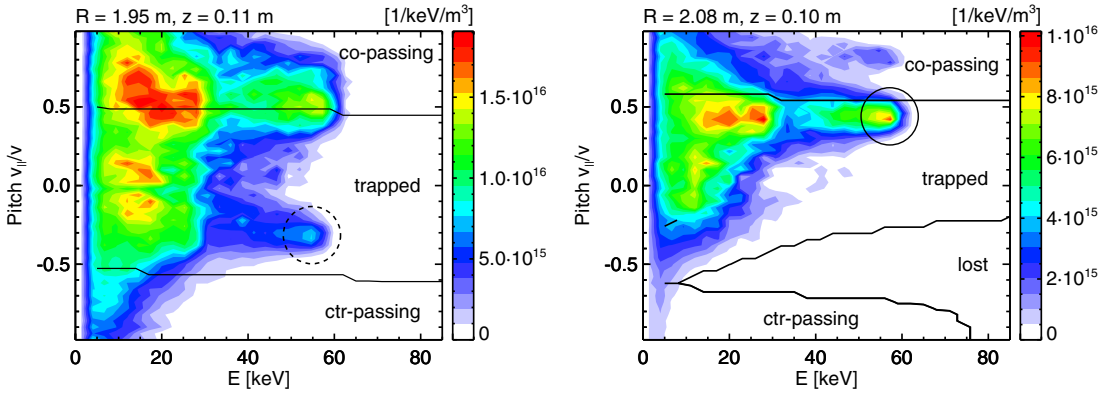

(a) $\rho_{tor} = 0.4$ **(b)** $\rho_{tor} = 0.8$

Figure 2.10: TRANSP/NUBEAM calculations of the fast-ion distribution from NBI Q3 for two positions on the LFS.

Orbit effects in TRANSP

Figure 2.10a shows the TRANSP calculation for our testcase with NBI Q3 at $\rho_{tor} = 0.4$ on the low field side. It can be seen, that apart from the expected peak at $\xi \approx 0.5$, a weaker peak is showing up at negative pitches ($\xi \approx -0.3$ - in the opposite direction of the NBI alignment). We have calculated the orbit classifications for the entire velocity space, and it can be seen that particles in that region are trapped. Hence, the peak at $\xi \approx -0.3$ must originate from fast ions, which were originally injected with positive pitch, but are on a trapped orbit and hence reappear at $\rho_{\mathrm{tor}} = 0.4$ with negative pitch. Using the orbit calculations, we can trace back the orbit and see, that the outer leg of the banana lies at $\rho_{\mathrm{tor}} = 0.8$ with $\xi \approx 0.4$. This corresponds to the local pitch between the NBI and magnetic field, as it can be seen from the TRANSP calculation (fig. 2.10b) at this position, which shows the injection peak at $\xi \approx 0.4$. Thus, the peak at $\rho_{\mathrm{tor}} = 0.4, \xi = -0.3$ and the peak at $\rho_{\mathrm{tor}} = 0.8, \xi = +0.4$ are not independent of each other, but they belong to the same fast-ion orbits (which is shown in fig. 2.11b). This can also be seen from the fact, that the absolute values of the peak are very similar.

The reason behind this is that the slowing down time scale is much longer than the time scale for a poloidal orbit turn. This fact can be used to rewrite the 4D fast ion distribution function $f(R, z, E, \xi)$ (i.e. two spatial and two velocity coordinates) into a 3D function of the three constant of motions $f(E, \mu, P_\varphi)$. The disadvantage of this formulation is that the COMs are not so easy to interpret as the more common variables (R, z, E, ξ) or (ρ, θ, E, ξ). Within our model, we are interested in profiles (e.g. fast-ion pressure and driven current), and for the calculation of those, the latter representation is more straightforward, also.

Averaging the deposition over first orbit

In the previous section, we have discussed that the TRANSP results can be quite well explained by a consideration of the first fast-ion orbit after birth. Hence, we can improve our model by taking the effect of the first orbit into account. This can be done by averaging the fast-ion deposition over the first orbit instead of just considering the deposition

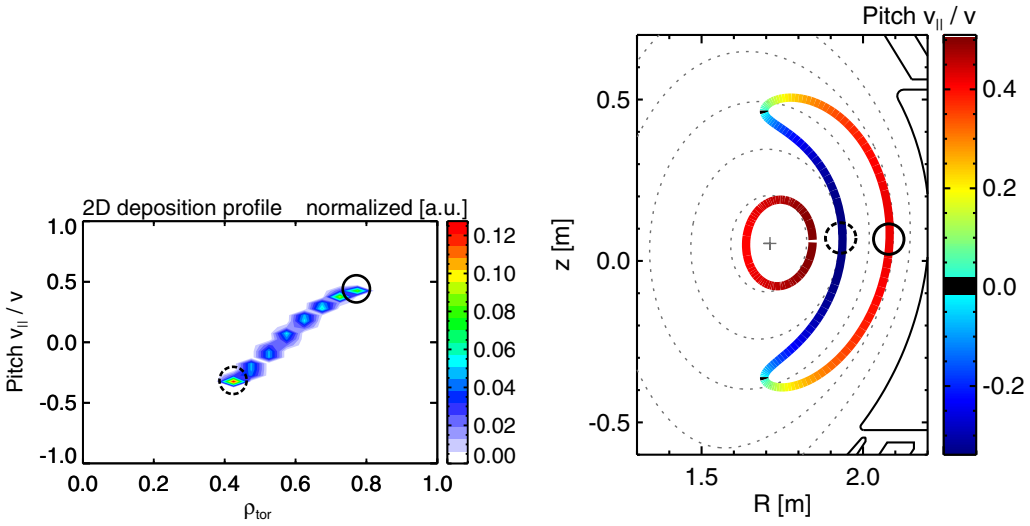

(a) (b)

Figure 2.11: (a) 2D Deposition profiles $S(\rho_{\mathrm{tor}}, \xi)$ for an individual fast-ion ($\xi = v_{\parallel}/v$). It is calculated by averaging over the first orbit, shown in (b).

position, as we have done it before. For a given born fast ion (Monte carlo marker), this results in a 2D deposition $S(\rho_{\mathrm{tor}}, \xi)$, which can be calculated straight-forwardly by a histogram of the first orbit, where the weight is given by the time the fast-ion stays in the given ρ and ξ bin.

Figure 2.11a shows an example of such a 2D deposition profile for a trapped particle orbit shown in fig. 2.11b. The original birth position is indicated with a circle. It can be seen that it lies on the outer leg of the banana (due to co-current NBI). Hence, taking into account the 2D deposition profile should decrease the resulting fast-ion density at the outer plasma around $\rho_{\mathrm{tor}} = 0.8$ and increase it further inwards. So, this leads to a correction needed to cure the deviations we have observed before in the outer plasma.

In fig. 2.12, we have calculated such an averaged 2D deposition function for all MC markers from the TRANSP birth profile. Here, fig. 2.12a shows the result for the 60 keV component and fig. 2.12b shows the 20 keV component. The plots reveal all relevant orbit effects during NBI. In the plasma center, the situation is fairly simple, and the pitch distribution is clearly peaked around $\xi = 0.5$. This is also the reason, why we achieved already good agreement in the model neglecting orbit effects. However, in contrast to our preliminary model, we have now also included the broadening of the pitch profile due to the finite width of the beam and the pitch changes the ions exhibit during their first orbit.

Towards the outer plasma, the situation gets more complex, and the pitch profiles split up into two branches. The upper one corresponds to deposition on the HFS, here the angle between NBI and the magnetic field is lower and hence the injection pitch is higher. Also it can be seen, that the HFS-branch is only visible for 60 keV, whereas the 20 keV neutrals hardly reach the HFS, because they get ionized already before. The lower branch corresponds to injection on the LFS, where the angle between beam and magnetic field is higher, and hence the pitch is lower. Due to the low pitch and the birth position on the LFS, some of these ions are trapped and we recognize the 2D deposition

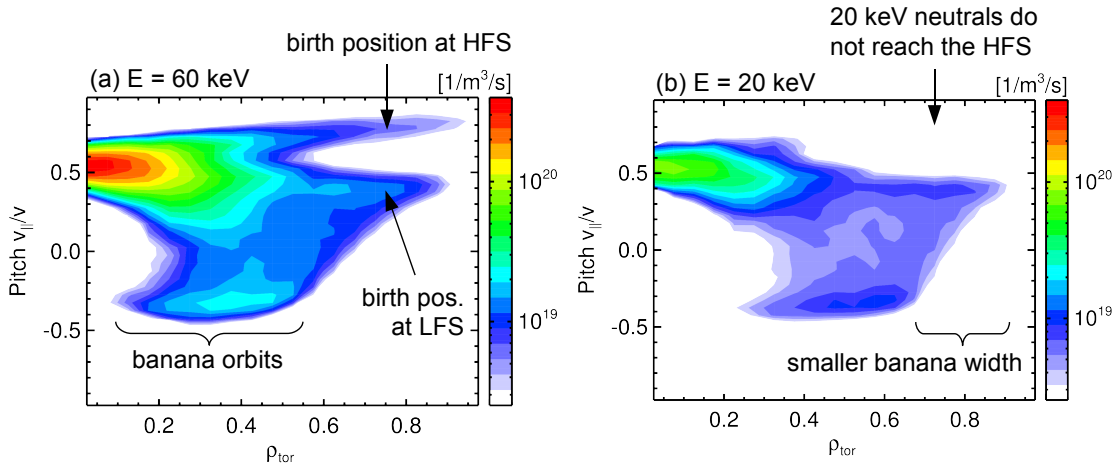

Figure 2.12: 2D Deposition profiles $S(\rho_{\mathrm{tor}}, \xi)$ for the (a) 60 keV and (b) 20 keV component of the beam.

shape corresponding to banana orbits (compare fig. 2.11a). For the 20 keV neutrals, the banana orbits have a much smaller width.

Improved fast-ion profiles

The first-orbit averaged deposition profiles $S(\rho, \xi)$ can be used in the Fokker-Planck solution straight-forwardly, because the solution discussed above allows a broad pitch distribution $K(\xi)$. Further orbit effects during the slowing down process are however still neglected. We again have computed fast-ion density and pressure profiles, and compare them to TRANSP. The results are shown in fig. 2.13 on a log scale. Due to the logscale, the large relative discrepancy between TRANSP and the previous model without orbit effects are much more clearly visible. Furthermore, it can be seen that the averaging over the first orbit cures this deviations, and greatly enhances the shape agreement with TRANSP, both for the pressure and density profiles.

The overall absolute values of density and pressure are slightly higher in our model than in TRANSP, especially around mid-radius positions. Several explanations can be given for this: Firstly, a large uncertainty arises from the Coulomb logarithm $\ln \Lambda$. We have compared eq. (2.19) with the Coulomb logarithm in the output of TRANSP, which can be described well if an offset of +0.95 is added to eq. (2.19). Typical values of $\ln \Lambda$ are 15-20, and the fast-ion density is proportional to $1/\ln \Lambda$. Thus, by using a formula for $\ln \Lambda$ more closely to the TRANSP values the agreement between both models could be improved. Secondly, we have considered in our model only prompt losses (i.e. losses due to ions whose first orbit is not confined). TRANSP considers further loss mechanisms, such as charge-exchange losses. Thirdly, neo-classical transport is not considered in our model. It would in general lead to a flattening of the profiles, and it is especially strong for trapped ions. Hence, this could explain the deviations at mid-radius positions.

In fig. 2.13c, the profiles of toroidal fast-ion current density j_{fi} and driven current density j_{NBCD} are shown in addition. We calculate the toroidal fast-ion current density as follows:

$$j_{\mathrm{fi}} = q \iint F \cdot (v_\varphi - v_{rot,\varphi}) \mathrm{d}E \mathrm{d}\xi \approx q \iint F \cdot (v_\parallel - v_{rot,\varphi}) \mathrm{d}E \mathrm{d}\xi \tag{2.62}$$

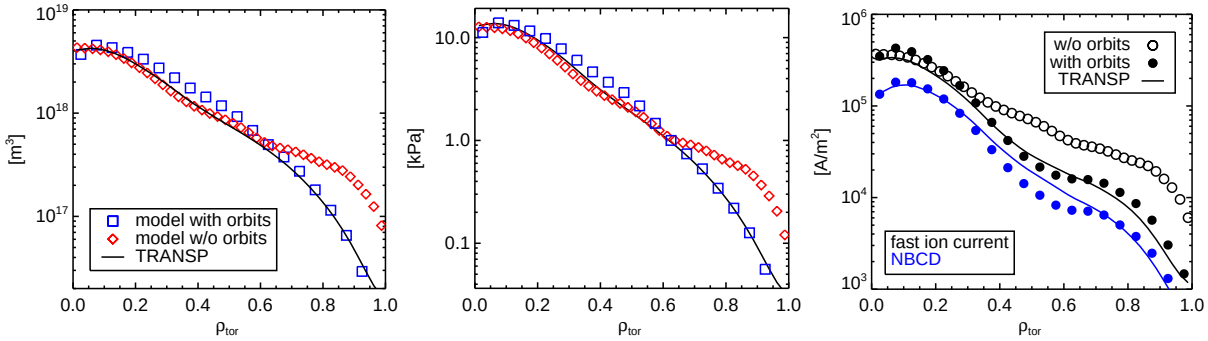

(a) Density **(b)** Pressure **(c)** Current density

Figure 2.13: Calculated fast-ion profiles from the model in comparison to TRANSP results.

Here, we subtract the toroidal plasma rotation $v_{rot,\varphi}$, because F is given in the lab frame but the current needs to be calculated with respect to the (rotating) plasma frame. The toroidal rotation does not result in a net current, because ions and electrons rotate in the same direction and with same speed. It can be seen in fig. 2.13c, that the orbit effects are very important for j_{fi}, because trapped particles change the sign of $v_{\parallel}$ along their orbit. On the inside of their banana orbit, they move in the opposite direction of the NBI direction, such that they decrease the fast-ion current. Hence, j_{fi} is strongly reduced in the regions of $\rho_{\mathrm{tor}} \gtrsim 0.3$, where trapped orbits occur mostly. In this case, the naive calculation without orbit effects is far off the TRANSP prediction, while the improved model with orbit effects shows very good agreement to TRANSP.

A part of this fast-ion current is however shielded by electrons, which follow the fast ions. In order to calculate the net current density driven by the NBI (j_{NBCD}), this needs to be taken into account by a factor η, such that $j_{\mathrm{NBCD}} = \eta j_{\mathrm{fi}}$. For η, several models and formulas exist. An overview is given e.g. in [23]. Basic models contain the effect of impurities (using the effective charge Z_{eff}) and of the trapped electron fraction ϵ_{t}. Large ϵ_{t} is beneficial for neutral beam current drive (NBCD), because trapped electrons cannot contribute to the current shielding as they cannot follow passing ions due to their bounce motion. More sophisticated models also include a correction due to the normalized electron collision rate ν_{e}^*. For the calculation shown in fig. 2.13c we have used:

$$\eta = 1 - \frac{Z_{\mathrm{fi}}}{Z_{\mathrm{eff}}} + \frac{Z_{\mathrm{fi}}}{Z_{\mathrm{eff}}} \epsilon_{\mathrm{t}} h(Z_{\mathrm{eff}}, \nu_{\mathrm{e}}^*, \epsilon) \tag{2.63}$$

where h is a rather complicated function of Z_{eff}, ν_{e}^* and the local aspect ratio ϵ, which is described in eq. (2.42-2.46) of [23]. With this approach, we find good agreement to the TRANSP prediction.

Dynamical phases after switching the beam on or off

Up to now, we have only considered the steady-state solution. If the plasma parameters (e.g. the temperatures and density) change only slowly with respect to the slowing down time (of order 100 ms), this is a very good approximation when the NBI heating is constant as well. However, for the phase directly after switching an NBI beam on or

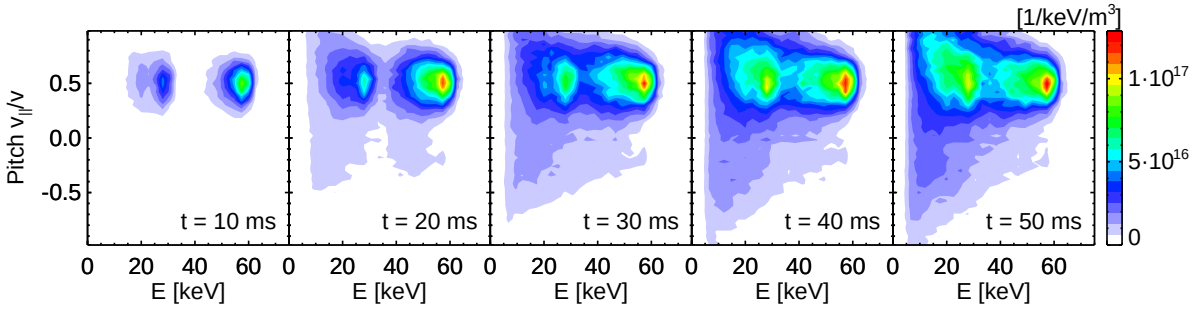

Figure 2.14: Temporal evolution of the fast-ion velocity distribution in the plasma center, calculated by TRANSP. The time t is given relative to the NBI-onset.

off, a dynamic description is needed. Fig. 2.14 shows a calculation from TRANSP for several time points directly after the NBI Q3 gets switched on. At the beginning only the 20, 30 and 60 keV peaks are visible, i.e. only newly born fast ions which have not yet slowed down due to collisions. As the time moves on, the fast ions slow down, filling up the parts of the velocity space below the injection energy. At the same time, the beam keeps generating new ions at the injection energy. After approximately one slowing down time, a quasi-steady state is reached. Obviously, also the other plasma parameters (temperature, rotation etc) may change during that phase, because the plasma heating is increased and the NBI induces a torque on the bulk plasma.

Neglecting these changes of the kinetic profiles, a solution of the time-dependent Fokker-Planck equation has been derived in [24] (i.e. keeping the $\frac{\partial f}{\partial t}$ term). Assuming, that the temporal evolution of the NBI source term follows a step function, i.e. $\sigma(t) \propto H(t)$ with H being the Heaviside function, the time dependent evolution of the distribution function can be described by a travelling front in the velocity space. When the beam gets turned on (at $t = 0$), the wave front starts at the injection energy, and propagates towards lower energies. The speed of this wave front is the averaged energy loss rate $\frac{\mathrm{d}E}{\mathrm{d}t}$ for test fast ions which we have already discussed in eq. (2.17). The time-dependent distribution function $f_t(E, \xi, t)$ for one energy species with injection energy E_0 is hence given by multiplying the steady-state solution with a time-dependent Heaviside function:

$$f_t(E, \xi, t) = f(E, \xi) \cdot H(E_0 - E(t)) \tag{2.64}$$

whereby $E(t)$ is given by the inversion of the slowing down time formula (2.20):

$$E(t) = \left[\exp\left(3 \cdot \frac{t_{\mathrm{sd}} - t}{\tau_{\mathrm{s}}}\right) - 1\right]^{3/2} \cdot E_{\mathrm{c}} \tag{2.65}$$

Figure 2.15a shows the function $E(t)$ calculated for our testcase and the three injection energies. The resulting distribution function is illustrated in fig. 2.15b, 10 ms after the beam was switched on.

Now we compare the results of this approach to TRANSP. Fig. 2.16a shows time-traces of fast-ion density and pressure. To allow a shape comparison between both time-traces (which have different units), the scales are set such, that the steady-state values in TRANSP lie on top of each other. For each time step, we have taken the actual values

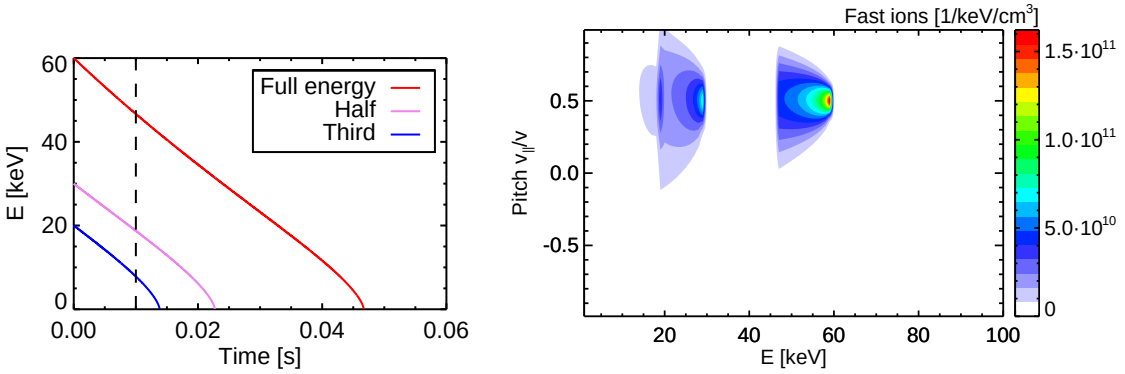

(a) **(b)**

Figure 2.15: **(a)** $E(t)$ for the three energy components of the beam. **(b)** Modeled temporal evolution of the fast-ion distribution function, 10 ms after the NBI was switched on.

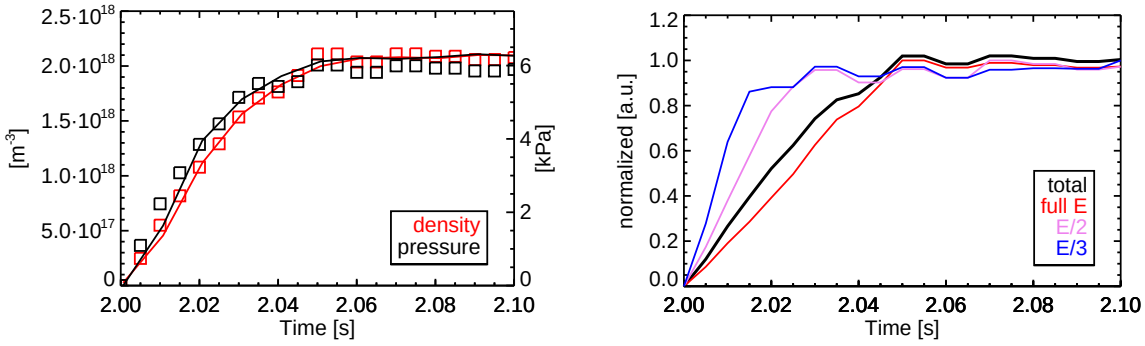

(a) Density and pressure. The model is shown with symbols, TRANSP with lines.

(b) Modeled density of the individual energy components.

Figure 2.16: Modeled temporal evolution of the fast-ion density and pressure in the plasma core.

of the kinetic profiles during each time step, although eq. (2.64) was derived under the assumption of constant kinetic profiles. It can be seen that very good agreement with the TRANSP time traces is found. The pressure build-up is faster than the density build-up, because the velocity space is filled up from "above". This feature is clearly seen in the TRANSP prediction, and is in good agreement also predicted by our model. Another consequence of this approach is, that the 20 keV beam ions reach their equilibrium density faster than the 30 keV and 60 keV ions, as it is expected (see fig. 2.16b).

The dynamic phase after switching off the beam can modeled analogously. To do so, it is simply needed to exchange the sign of the argument of the Heaviside function, i.e.:

$$f_t(E,\xi,t) = f(E,\xi)\cdot H\big(\pm(E_0 - E(t))\big) \text{ for a NBI source } \sigma(t) \propto H(\pm t) \qquad (2.66)$$

2.4 Ion cyclotron resonance heating

Ion cyclotron resonance heating (ICRH) is based on the excitation of a wave in the plasma, which has the same frequency as the gyromotion of the ions (fundamental ICRH) or

higher multiples (higher harmonic ICRH). In general, the resonance condition (including Doppler-shifts) for the angular frequency of the wave ω is given by:

$$\omega - k_\parallel v_\parallel - n\omega_{\mathrm{ci}} = 0 \quad \text{with: } n \in \mathbb{N},\ \omega_{\mathrm{ci}} = \frac{|q|B}{m} \tag{2.67}$$

Here, $n = 1$ corresponds to fundamental (or first harmonic) ICRH, $n = 2$ to second harmonic and so forth. $k_\parallel$ is the wave number parallel to the magnetic field ($k = \frac{2\pi}{\lambda}$). It is mainly determined by the antenna and machine geometry. Due to the toroidal boundary condition in a tokamak, $k_\parallel$ must fulfill:

$$k_\parallel \cdot R \approx n_\varphi \text{ with: } n_\varphi \in \mathbb{N} \tag{2.68}$$

The spectrum of toroidal modes n_φ is then defined by the shape of the antenna. For the ASDEX Upgrade antennas, the dominant toroidal mode is $n_\varphi \approx 12$ [25] and hence $k_\parallel$ is in the order of $k_\parallel \approx 7\ \mathrm{m}^{-1}$.

The magnetic field in a tokamak is varying with $1/R$, which defines a unique radial position, where the resonance condition is fulfilled. Hence it is possible to control the heating position by adjusting the magnetic field or the ICRH frequency. The Doppler-shift leads to a broadening of this resonance layer. For example, 60 keV fast D ions injected with $\xi = 0.5$ see a Doppler shift of $k_\parallel v_\parallel \approx 2\pi \cdot 1.3$ MHz. In the standard ICRH setup for central heating (B=2.4 T, f=36.5 MHz), this corresponds to a radial shift of the resonance position of 6 cm.

In the ion cyclotron frequency range, the only wave which can propagate directly across the magnetic field is the so-called fast magnetosonic (compressional Alfvén) wave, or short the *fast wave*. As the wave propagates through the plasma, the frequency remains constant, however the wave numbers perpendicular and parallel to the magnetic field ($k_\perp$ and $k_\parallel$) change according to the dispersion relation. The latter can be derived from Maxwell's equation in matter. To do so, several assumptions can be made: Due to the high conductivity parallel to the magnetic field for low frequencies (i.e. $\omega \ll \omega_{\mathrm{pe}}$, the electron plasma frequency), the parallel component of the electric field can be neglected with respect to the perpendicular component: $|E_\parallel| \ll |E_\perp|$. In the cold plasma approximation the dispersion relation for the refractive indices ($\frac{\omega}{k} = \frac{c}{n}$) can be derived as: [26, eq. 5.8.2]

$$n_\perp^2 = \frac{\left[\sum_j \frac{\omega_{pj}^2}{\omega_{cj}(\omega+\omega_{cj})} - n_\parallel^2\right]\left[\sum_j \frac{\omega_{pj}^2}{\omega_{cj}(\omega-\omega_{cj})} + n_\parallel^2\right]}{\left[\sum_j \frac{\omega_{pj}^2}{\omega^2-\omega_{cj}^2} + n_\parallel^2\right]} \tag{2.69}$$

Here, the index j denotes different ion species in the plasma, and indices p and c correspond to plasma and cyclotron angular frequencies, respectively. Wave propagation demands $n_\perp^2 > 0$. In eq. (2.69), the first bracket on the right hand side can go through zero and become negative. This defines a cut-off condition for the fast wave:

$$n_\perp^2 > 0 \Leftrightarrow \sum_j \frac{\omega_{pj}^2}{\omega_{cj}(\omega+\omega_{cj})} - n_\parallel^2 > 0 \tag{2.70}$$

For a pure deuterium plasma and $\omega = 2\omega_{cD}$ this condition simplifies to:

$$\omega_{\mathrm{pD}}^2 = \frac{n_{\mathrm{D}} q^2}{\epsilon_0 m_{\mathrm{D}}} > \frac{3}{4} c^2 k_\parallel^2 \tag{2.71}$$

Using $k_\parallel \approx 7\mathrm{m}^{-1}$, this gives a condition for the plasma density $n_\mathrm{e} = n_\mathrm{D} > 4 \cdot 10^{18}\ \mathrm{m}^{-3}$. Below this cut-off density, the wave cannot propagate and is evanescent. Thus, the fast wave is evanescent at the ICRH antenna, and must tunnel through the evanescence layer into the plasma. For an efficient coupling, the antenna must be placed as close as possible to the plasma boundary (i.e. the separatrix).

2.4.1 The Kennel-Engelmann operator

The effect of ICRH on the ion distribution function f can be described by an additional operator Q_RF, which is added to the left hand side of the Fokker-Planck equation (2.25). Yakimenko [27] and Kennel and Engelmann [28] have derived this operator for a uniform plasma (i.e. with volume $V \to \infty$). They used Cartesian coordinates (x, y, z), where the homogeneous static magnetic field B_0 is aligned in the z-direction. Hence, the z-component is parallel to the magnetic field, while x and y are perpendicular to it. The oscillating parts of the magnetic and electric fields are written as Fourier decomposition:

$$\vec{B}(\vec{x}, t) = B_0 \hat{e}_z + \int \frac{\mathrm{d}^3 k}{(2\pi)^3} \exp(\mathrm{i}\vec{k} \cdot \vec{x}) \vec{B}_k(t) \tag{2.72}$$

$$\vec{E}(\vec{x}, t) = \int \frac{\mathrm{d}^3 k}{(2\pi)^3} \exp(\mathrm{i}\vec{k} \cdot \vec{x}) \vec{E}_k(t) \tag{2.73}$$

with $\vec{E}_k(t)$ and $\vec{B}_k(t)$ being the Fourier amplitudes. Starting from this, they derived the operator Q_RF describing the influence of the oscillating $\vec{E}$ and $\vec{B}$ fields on the distribution function f: [29]

$$Q_\mathrm{RF}(f) = \lim_{V \to \infty} \sum_n \frac{\pi Z^2 e^2}{m^2} \int \frac{\mathrm{d}^3 k}{(2\pi)^3 V} L\, v_\perp\, \delta(w - k_\parallel v_\parallel - n\omega_\mathrm{ci})\, |\theta_{n,k}|^2\, v_\perp\, L\, f \tag{2.74}$$

where

$$L \equiv \left(1 - \frac{k_\parallel v_\parallel}{\omega}\right) \frac{1}{v_\perp} \frac{\partial}{\partial v_\perp} + \frac{k_\parallel}{\omega} \frac{\partial}{\partial v_\parallel} \tag{2.75}$$

$$\theta_{n,k} = \frac{1}{2} e^{-\mathrm{i}\Psi} \cdot (E_x + \mathrm{i}E_y)_k \cdot J_{n-1}\left(\frac{k_\perp v_\perp}{\omega_\mathrm{ci}}\right) + \frac{1}{2} e^{\mathrm{i}\Psi} \cdot (E_x - \mathrm{i}E_y)_k \cdot J_{n+1}\left(\frac{k_\perp v_\perp}{\omega_\mathrm{ci}}\right) + \\ + \frac{v_\parallel}{v_\perp} \cdot (E_z)_k \cdot J_n\left(\frac{k_\perp v_\perp}{\omega_\mathrm{ci}}\right) \tag{2.76}$$

$$\vec{k} = k_\perp \cos\Psi \hat{e}_x + k_\perp \sin\Psi \hat{e}_y + k_\parallel \hat{e}_z. \tag{2.77}$$

Here, Ψ is related to the choice of the x, y coordinates and we can set $\Psi = 0$ for convenience. In the argument of the δ function, we recognize the resonance condition (2.67) with n defining the cyclotron harmonic. L is a derivative operator with respect to $v_\perp$ and $v_\parallel$. It appears twice in Q_RF, hence Q_RF describes a diffusion in the velocity space. $\theta_{n,k}$ contains the contributions from the different polarization of the electric field. Here, $E_x + \mathrm{i}E_y \equiv 2E_+$ corresponds to a left circular polarized wave (i.e. rotating in the same direction as the gyration of the ions), whereas $E_x - \mathrm{i}E_y \equiv 2E_-$ is the right circular polarized component (rotating in the opposite direction). $E_z = E_\parallel$ is the component parallel

to the magnetic field. As discussed earlier, in the ion cyclotron range of frequencies it is very weak with respect to the perpendicular components due to the good conductivity parallel to $\vec{B}$. Hence, E_z can be neglected in good assumption. $J_\alpha(x)$ denote the Bessel function (of the first kind), and it can be seen that each component of the electric field is multiplied by a different Bessel function, depending on n. The argument of the Bessel function can be rewritten as $\frac{k_\perp v_\perp}{\omega_{ci}} = k_\perp r_L = \frac{2\pi r_L}{\lambda_\perp}$ with r_L being the Larmor radius. Hence, the Bessel functions describe the physical effects resulting from the ion Larmor radius having a comparable size with respect to the perpendicular wavelength. Those effects are called *finite Larmor radius* (FLR) effects. Obviously, FLR effects are more important for fast ions, and play a less important role for thermal particles (especially if the ion temperature is low). In the following, we will start a detailed discussion of the Kennel-Engelmann operator in the small Larmor radius limit $k_\perp r_L \to 0$, and return later to the FLR effects.

Small Larmor radius limit

The small Larmor radius limit $k_\perp r_L \to 0$ greatly simplifies Q_{RF}: The argument of the Bessel functions become zero, and $J_\alpha(0)$ vanishes for all $\alpha \neq 0$. Hence, only one term survives in Q_{RF}: The term describing absorption of the left circular component E_+ at the fundamental ion cyclotron frequency ($n = 1$). A basic sketch of this situation is shown in the top row of fig. 2.17: The electric field vector rotates with the same direction and frequency, as the perpendicular component of the velocity vector of the fast-ion. Hence, the ion gets effectively accelerated or decelerated in its perpendicular velocity component. Whether acceleration or deceleration takes place depends obviously on the relative phase between the gyromotion and the electric field. In fig. 2.17, we have chosen the relative phase corresponding to maximum acceleration. In general however, the phase of the gyration is distributed randomly uniformly among all ions, and hence particles will be randomly accelerated or decelerated. This is even true for one individual ion: During

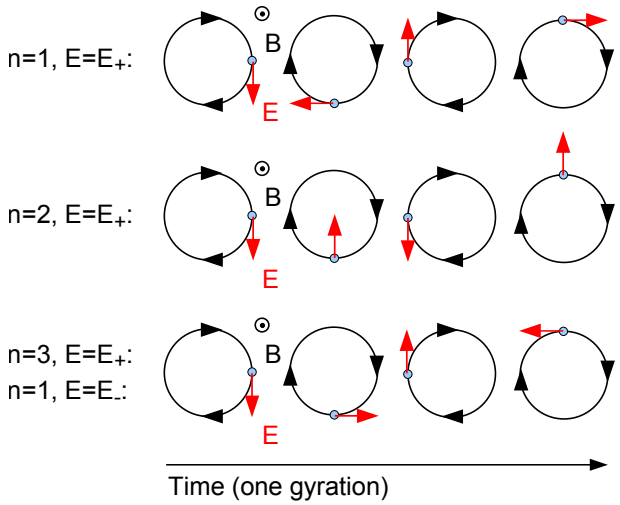

Figure 2.17: Illustration of the small Larmor radius limit, $k_\perp r_L \to 0$. In this limit, only fundamental absorption $n = 1$ of a circular polarized wave E_+ (rotating in the same sense as the ions) is possible. For all other absorption schemes, the effect of $\vec{E}$ averages out during one gyro period.

the motion on its orbit, it will pass through the ICRH resonance layer repeatedly. On each passage, the gyrophase will be different, and hence even this individual particle will be randomly accelerated or decelerated, i.e. it performs a random walk in velocity space. This behavior corresponds to a diffusion in velocity space, and this explains why Q_{RF} is a diffusion-type operator (i.e. the differential operator L appears twice).

Direction of diffusion

In the sketch of fig. 2.17, we have neglected the effects of Doppler-Shifts, i.e. $\frac{k_\parallel v_\parallel}{\omega} \approx 0$. Then, L simplifies:

$$L \equiv \left(1 - \frac{k_\parallel v_\parallel}{\omega}\right) \frac{1}{v_\perp} \frac{\partial}{\partial v_\perp} + \frac{k_\parallel v_\parallel}{\omega} \frac{1}{v_\parallel} \frac{\partial}{\partial v_\parallel} \approx \frac{1}{v_\perp} \frac{\partial}{\partial v_\perp} \tag{2.78}$$

In this limit, L contains only the derivative $\frac{\partial}{\partial v_\perp}$ and hence Q_{RF} describes a diffusion in the $v_\perp$-direction of the velocity space, which is in line with the qualitative picture we got from the sketch. Also within this limit, the entire velocity space is resonant (i.e. the resonance condition simplifies to $\omega = n\omega_{\mathrm{ci}}$, which is fulfilled only at one narrow radial position (with respect to the major radius R).

For deuterium beam ions injected by NBI Q3 ($E = 60$ keV, $\xi = 0.5$) and the standard ASDEX Upgrade ICRH frequency $\omega = 2\pi \cdot 36.5$MHz we find $\frac{k_\parallel v_\parallel}{\omega} \approx 0.037$ and hence the diffusion will indeed go mainly in the $v_\perp$-direction.

If Doppler-shifts are not neglected, the general shape of L has to be considered, and diffusion goes also into the $v_\parallel$ direction. In general, it can be seen, that L is a gradient operator in the velocity space, acting tangential to circles described by:

$$v_\perp^2 + (v_\parallel - \frac{\omega}{k_\parallel})^2 = C = const, \tag{2.79}$$

because $LC = 0$. Those circles are drawn in fig. 2.18, together with the resonance condition: With finite Doppler-shifts, not the entire velocity space is resonant at a fixed radial position R, but only a vertical line described by $v_\parallel = \frac{\omega}{k_\parallel} - \frac{n\omega_{\mathrm{ci}}}{k_\parallel}$. However, the resonance layer has now a finite width, and in different radial positions R, different parts of the velocity space are resonant - such that in total, the entire velocity space is resonant like in the zero-Doppler-shift approximation. The resonance condition can be identified in fig. 2.18 by the vertical line, only particles on that line are resonant. Diffusion happens then in the direction of the circle tangents.

Why diffusion is heating

As described in the previous section, ion cyclotron resonance heating causes a diffusion in the velocity space. One may ask now the question, how this diffusion leads to heating. To asses this question, we recall Fick's law (2.23). Considering only the perpendicular diffusion, this diffusion leads to the following velocity space flow:

$$\vec{\Gamma} = -D_\perp \frac{\partial f}{\partial v_\perp} \hat{e}_\perp \tag{2.80}$$

where the diffusion constant $D_\perp$ can be derived from the Kennel-Engelmann operator. In order to have a flow towards higher velocities (and hence particle heating), $\frac{\partial f}{\partial v_\perp}$ must

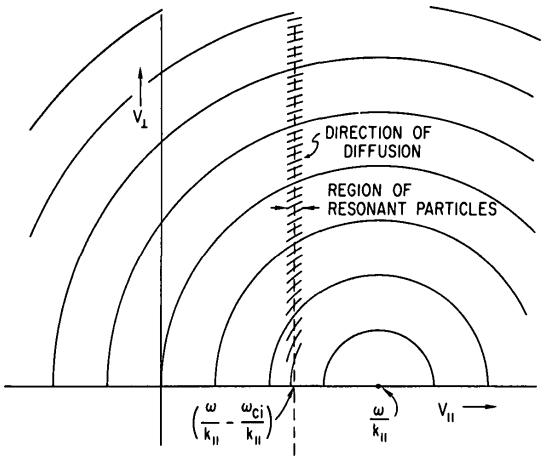

Figure 2.18: The gradient operator L is acting in the velocity space along the indicated circles. Diffusion takes place in the direction of the circle tangents, but only where the resonance condition is fulfilled (dashed line). The circle origin lies on the $v_\parallel$-axis. In the limit of small Doppler-shifts $\omega/k_\parallel \to \infty$, the circle origin moves towards $v_\parallel \to \infty$ and diffusion goes mainly in the $v_\perp$ direction. (Figure from [29])

be negative. This condition is fulfilled in many cases: E.g., thermal ions with a Maxwell distribution $f \propto \exp(-\frac{v_\perp^2+v_\parallel^2}{2mT})$ fulfill $\frac{\partial f}{\partial v_\perp} < 0$ in the entire velocity space. Beam ion distributions are rather flat below the injection velocity, but have a very steep fall-off above the injection energy. Hence, ICRH will cause a diffusion of ions in the velocity space region above the injection energy and consequently cause a high energy tail. Ultimately, every distribution function must go to zero for $v_\perp \to \infty$ in order to have a finite ion density. Hence, every distribution function must have a negative $v_\perp$ gradient towards high velocities, that allows a net acceleration due to ICRH.

Higher harmonic heating due to finite Larmor radius effects

Up to now, we have discussed the small Larmor radius case $k_\perp r_\mathrm{L} = 0$. In this case, we have seen that only absorption of E_+ is possible at the fundamental frequency ($n = 1$). We will now explain, why all other absorption cases in $\theta_{n,k}$ do not work in this limit. Fig. 2.17 shows a sketch of the temporal evolution of the ion velocity vector and the electric field vector for four equidistant phases of the gyromotion. The top row corresponds to $n = 1$, E_+, and we have seen that the electric field is aligned such, that net acceleration or deceleration occurs. In the second row, the 2nd harmonic case ($n = 2$) with E_+ is sketched. Here, the electric field vector rotates twice as fast as the velocity vector. Hence, there is a phase during the gyroorbit, were acceleration takes place, but in the opposite phase, the ion is decelerated by the same amount. Thus, no net effect results, i.e. $n = 2$ absorption of E_+ is not possible for $k_\perp r_\mathrm{L} \to 0$. The third row corresponds to $n = 3$, E_+ and also to $n = 1$, E_-, because both cases result in the same phasing between $\vec{E}$ and $\vec{v}$. This explains, why both terms are multiplied by the same Bessel function $J_2(x)$ in $\theta_{n,k}$. Also in these cases, the effect of the electric field cancels out during one gyroorbit for $k_\perp r_\mathrm{L} = 0$.

We will now discuss the more general case, i.e. a finite $k_\perp r_\mathrm{L}$. Fig. 2.19 shows a comic for the 2nd harmonic absorption of E_+, but with a wavelength of comparable size as the

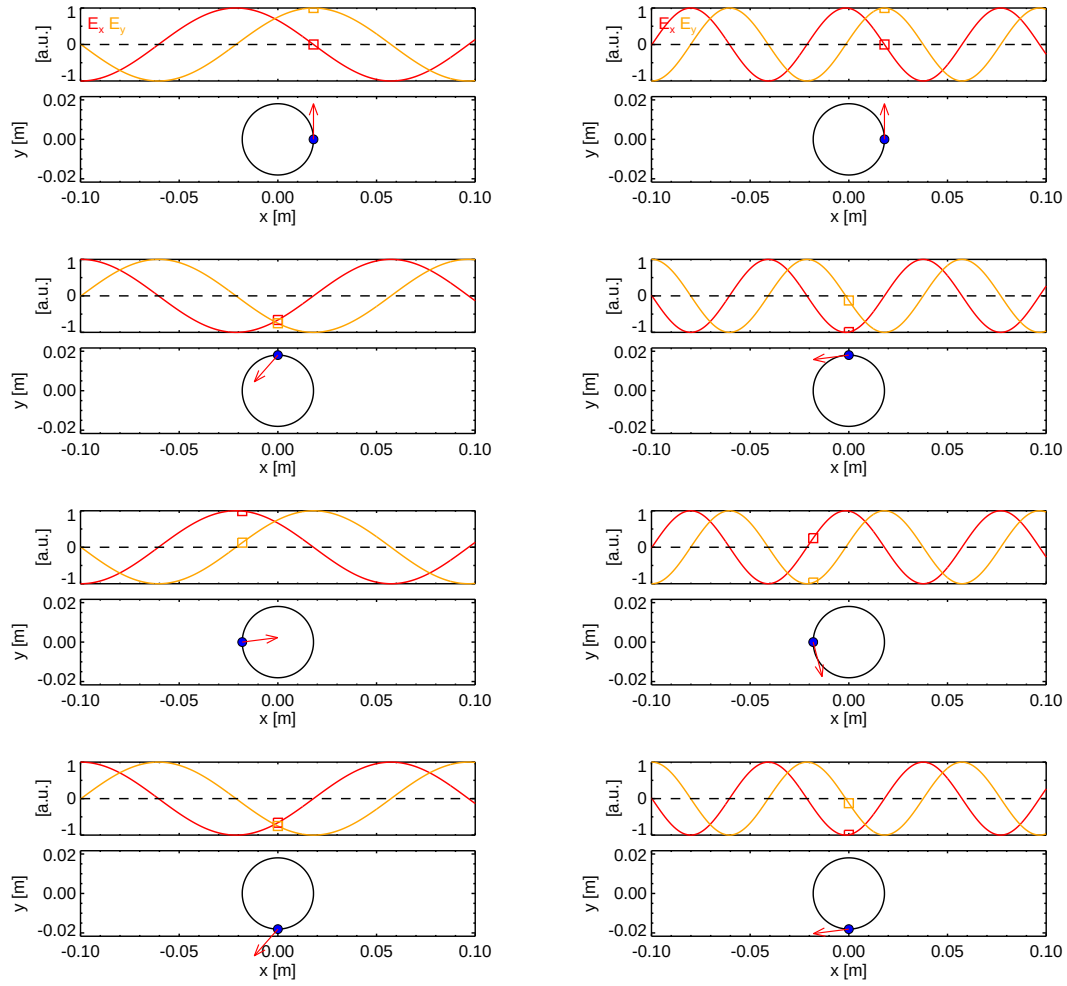

(a) $k_\perp = 40\ \mathrm{m}^{-1}$ **(b)** $k_\perp = 80\ \mathrm{m}^{-1}$

Figure 2.19: Illustration of large Larmor radius effect on 2nd harmonic absorption of a left circular polarized electric field, in four phases of the gyromotion (rows) and for two different perpendicular wave numbers $k_\perp$ (columns). The Larmor radius is $r_\mathrm{L} = 1.8\,\mathrm{cm}$, which corresponds to fast D ions injected by NBI Q3 ($E = 60\mathrm{keV}$, $\xi = 0.5$) at B=2.4 T.

gyroradius. In the top row, the x and y component of the electric field is sketched. In the bottom row, we have plotted again the gyrating ion with the electric field vector. Here, we have drawn the ion gyration as perfect cycle, i.e. we have not taken into account deviations due to the electrical field force. Furthermore, we have neglected the motion parallel to the magnetic field ($v_\parallel = 0$). Due to $k_\perp r_\mathrm{L} > 0$, the electric field varies now in a more complex scheme. The important quantity to consider is the acceleration of the gyromotion, which is given by the component of $\vec{E}$ which is tangential to the gyromotion. It can be seen that the acceleration in phase 1 and 3 do not cancel any more (while acceleration in phase 2 and 4 cancel again).

In general, of course, not only these four representative phases must be considered, but the acceleration during the entire gyromotion. Within this basic comic-model, we have calculated the acceleration of $v_\perp$ by calculating the projection $\vec{E} \cdot \vec{v}$ (we are satisfied with arbitrary units here). The result during one gyroorbit is shown in fig. 2.20, for three cases

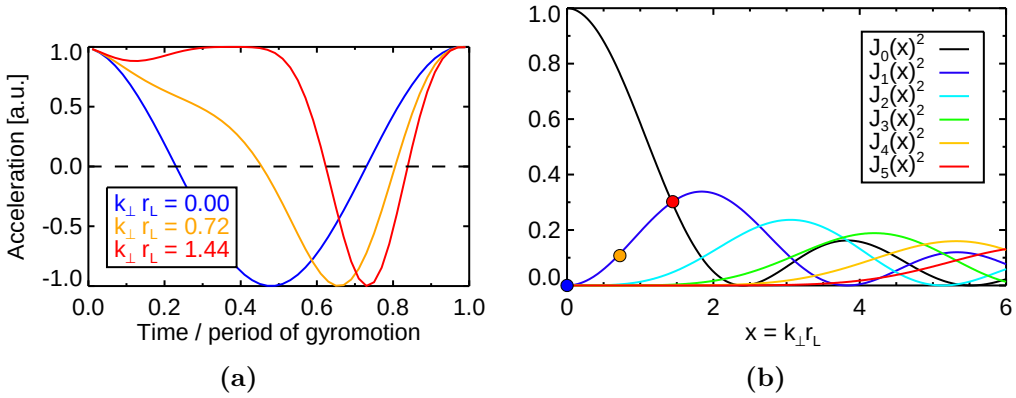

(a) **(b)**

Figure 2.20: (a) Acceleration of the gyromotion ($\propto \vec{E} \cdot \vec{v}$) as a function of time during one gyroorbit. **(b)** Bessel functions of order 0-5. They yield the effectiveness of ICRH wave absorption as a function of $k_\perp r_\mathrm{L}$ (comp. eq. (2.74) and (2.76)). The points correspond to the integrated acceleration (over one gyroorbit) from (a), and it can be seen that they align on J_1^2, which is expected because J_1 corresponds to 2nd harmonic absorption of E_+.

of $k_\perp r_\mathrm{L}$. The case with $k_\perp r_\mathrm{L} = 0$ corresponds to fig. 2.17, and it can be seen that the acceleration has a purely sinusoidal shape. This can be expected from the fact, that $\vec{E}$ is rotating with twice the frequency as $\vec{v}$. The total integral of the acceleration is zero, in line with our previous consideration, that 2^{nd} harmonic absorption is not possible in the small Larmor orbit limit. With increasing $k_\perp r_\mathrm{L}$, the acceleration curve becomes more anharmonic, in such a way that the total integral becomes non-zero. We have computed this integral for the three cases, and compared it with $J_1(k_\perp r_\mathrm{L})^2$. It can be seen, that the explanation given here matches well with the precise calculation with the Bessel function. From the shape of $J_1(k_\perp r_\mathrm{L})^2$, it can be seen that there is a maximum, and the red case in fig. 2.20a is quite close to it. An explanation for this maximum can be seen in fig. 2.19b: In phase 1 and 3, $\vec{E}$ points almost parallel to the movement of the ion which results in a large net acceleration. Increasing $k_\perp r_\mathrm{L}$ further beyond the maximum in $J_1(k_\perp r_\mathrm{L})^2$ will then again decrease the net acceleration.

In conclusion, fundamental absorption of E_+ is the only scheme which works for $k_\perp r_\mathrm{L} = 0$ (e.g. cold, thermal ions). In general, its efficieny is described by $J_0(k_\perp r_\mathrm{L})^2$ (see $\theta_{n,k}$ in eq. 2.76) and it is decreasing with increasing $k_\perp r_\mathrm{L}$. Second harmonic ($n = 2$) absorption of E_+ is only possible for $k_\perp r_\mathrm{L} > 0$, its dependency is described by $J_1(k_\perp r_\mathrm{L})^2$. Furthermore, third harmonic ($n = 3$) absorption of E_+ and fundamental ($n = 1$) absorption of E_- are both described by $J_2(k_\perp r_\mathrm{L})^2$ and they need even larger $k_\perp r_\mathrm{L}$ to work efficiently.

Calculation of $k_\perp r_\mathrm{L}$

In general, the $k_\perp r_\mathrm{L}$-dependence of E_+ absorption at the n-th harmonic is given by $J_{n-1}(k_\perp r_\mathrm{L})^2$, and for E_- absorption it is given by $J_{n+1}(k_\perp r_\mathrm{L})^2$ (see $\theta_{n,k}$). The calculation of the Larmor radius r_L is straightforward and has been given in eq. (2.42). The perpendicular wave number $k_\perp$ can be calculated using the cold plasma dispersion relation eq. (2.69). If only a one-species plasma is considered and the parallel component is neglected

(i.e. $n_\parallel^2 \ll n_\perp^2 \Leftrightarrow k_\parallel^2 \ll k_\perp^2$), eq. (2.69) can be strongly simplified. If $\omega = n\omega_{\mathrm{ci}}$ is inserted, one gets: [30, eq. 2.24], [31, eq. 2]

$$k_\perp \approx \frac{\omega}{v_{\mathrm{A}}} \text{ with the Alfvén velocity: } v_{\mathrm{A}} = c\frac{\omega_{\mathrm{ci}}}{\omega_{\mathrm{pi}}} = \frac{B}{\sqrt{\mu_0 m_{\mathrm{i}} n_{\mathrm{i}}}} \tag{2.81}$$

Numerical example:
For a pure deuterium plasma with $n_{\mathrm{i}} = 4 \cdot 10^{19}\mathrm{m}^{-3}$, $B = 2.4\mathrm{T}$, and the standard ASDEX Upgrade ICRH frequency $\omega = 2\pi \cdot 36.5$ kHz we get $k_\perp \approx 40\ \mathrm{m}^{-1}$. Compared to $k_\parallel \approx 7\ \mathrm{m}^{-1}$, one sees that $k_\parallel^2 \ll k_\perp^2$ is well fulfilled. Taking the Larmor radius of injected fast D ions from NBI Q3 (E=60 keV, $\xi = 0.5$), we get $r_{\mathrm{L}} = 1.8$ cm and $k_\perp r_{\mathrm{L}} = 0.71$. These numerical values were also used for the sketch in fig. 2.20a and correspond to the orange dot and curve in fig. 2.20b. It can be seen that substantial 2nd harmonic absorption is possible for these fast ions.

2.4.2 Wave polarization and suitable ICRH scenarios

In the previous sections, we have seen that fundamental $n = 1$ absorption of the left-circular polarized wave E_+ is the most preferential absorption scenario: It is effective for a broad range of realistic $k_\perp r_{\mathrm{L}}$ values, and in particular it is the only possible scenario in the limit $k_\perp r_{\mathrm{L}} = 0$. Hence, it can be easily used to heat cold plasmas, without any further auxiliary heating. For this heating scenario, E_+ must be present at the resonance layer. However, the wave polarization cannot be fixed externally (e.g. by the antenna), instead it evolves due to the interaction between the wave and the plasma.

For a one-species plasma, the relative strength of E_+ can be calculated assuming the cold plasma approximation and $\omega_{\mathrm{ci}} < \omega \ll \omega_{\mathrm{pi}}$ as follows: [31]

$$\frac{|E_+|^2}{|E_y|^2} = \frac{\left(\frac{\omega}{\omega_{\mathrm{ci}}} - 1\right)^2 \cdot \left(\frac{\omega}{\omega_{\mathrm{ci}}} - \frac{k_\parallel^2}{k^2}\right)^2}{4\left|\frac{\omega}{\omega_{\mathrm{ci}}}\left(1 + \frac{k_\parallel^2}{k^2}\right)\right|^2} \longrightarrow \frac{1}{4}\left(\frac{\omega}{\omega_{\mathrm{ci}}} - 1\right)^2 \quad \text{for: } \frac{k_\parallel^2}{k^2} \to 0 \tag{2.82}$$

Here, k is the full length of the wave vector and is consequently given by $k = \sqrt{k_\perp^2 + k_\parallel^2}$. Following the numerical example from above, we get $\frac{k_\parallel^2}{k^2} \approx \frac{7^2}{40^2} = 0.03$ and the approximation in the second step is fulfilled well. In general, the fast wave shows elliptical polarization, which is given by: (eq. 2.29 in [30], [29])

$$\frac{\mathrm{i}E_x}{E_y} = \frac{\frac{\omega^2}{\omega_{\mathrm{ci}}^2} + \frac{k_\parallel^2}{k^2}}{\frac{\omega}{\omega_{\mathrm{ci}}}\left(1 + \frac{k_\parallel^2}{k^2}\right)} \xrightarrow{k_\parallel^2/k^2 \to 0} \frac{\omega}{\omega_{\mathrm{ci}}} \tag{2.83}$$

It can be seen from eq. (2.82) that, for fundamental heating, E_+ vanishes at the resonance layer ($\omega = \omega_{\mathrm{ci}}$). In line with that, eq. (2.83) yields $\mathrm{i}E_x/E_y = +1$, which means that the wave is purely circular polarized in the opposite polarization E_-, since $E_\pm = \frac{1}{2}(E_x \pm \mathrm{i}E_y) = \frac{1}{2}(-\mathrm{i}E_y \pm \mathrm{i}E_y)$. This result can be interpreted such, that the gyrating ions shield out the left-handed polarization. Higher harmonic absorption schemes $n > 1$ do not have this problem. For example, for $\omega = 2\omega_{\mathrm{ci}}$ one gets $\mathrm{i}E_x/E_y = +2$ and

$E_\pm = \frac{1}{2}(-2\mathrm{i}E_y \pm \mathrm{i}E_y)$. Hence, the wave is elliptically polarized, and both circular polarization exist: $|E_+| = \frac{1}{2}|E_y|$ and $|E_-| = \frac{3}{2}|E_y|$. However, these $n > 1$ schemes work only for large Larmor radii.

A way to overcome this unfavorable situation is the so-called *minority heating* scheme. Here, a plasma with at least two species is needed. If the species, which is resonant at $n = 1$, has a very low concentration (e.g. $\lesssim 10\%$), its interaction with the wave is weak, such that the wave electric field can keep the correct polarization E_+, which can be absorbed then by the minority. This effect cannot be explained by the cold plasma theory, instead the hot plasma contribution has to be taken into account. Then, the wave polarization for the minority heating scheme at the minority resonance can be approximated as: [31]

$$\frac{|E_+|^2}{|E_y|^2} = \frac{1}{4(1+\sigma^2)} \quad \text{with:} \quad \sigma^2 = \frac{\pi}{4}\left(\frac{n_\mathrm{m}}{n_\mathrm{M}}\frac{m_\mathrm{M}}{m_\mathrm{m}}\frac{Z_\mathrm{m}^2}{Z_\mathrm{M}^2}\right)^2 \left(1 - \frac{\omega_\mathrm{cM}^2}{\omega^2}\right)^2 \left(\frac{\omega}{k_\parallel v_\mathrm{ti}}\right)^2 \tag{2.84}$$

Here indices m and M stand for the minority and majority species, respectively, and v_ti is the thermal velocity. How much E_+ is present at the resonance, depends strongly on the minority concentration. Assuming hydrogen as minority and deuterium as majority (i.e. $\omega = \omega_\mathrm{cH} = 2\omega_\mathrm{cD}$), a plot of $\frac{|E_+|^2}{|E_y|^2}$ as a function of the minority concentration is shown in fig. 2.21. For vanishing hydrogen concentration ($n_\mathrm{m} = 0$), the same ratio

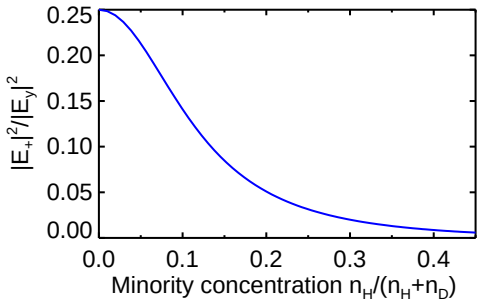

Figure 2.21: Wave polarization $\frac{|E_+|^2}{|E_y|^2}$ for the hydrogen minority heating scheme as function of the minority density (according to eq. 2.84).

$|E_+|^2/|E_y|^2 = 1/4$ is obtained as for pure 2nd harmonic D heating (see the numerical example from eq. (2.82) above). If the hydrogen concentration is non-zero, but low enough ($\lesssim 5\%$), $|E_+|^2/|E_y|^2$ stays almost the same and it can be absorbed very efficiently at the fundamental frequency by the minority. If the minority concentration gets too high, $|E_+|^2/|E_y|^2$ goes down rapidly to zero, which corresponds to the result from the one-species cold plasma calculation (2.82) for $\omega = \omega_\mathrm{ci}$. This heating scheme has been actually found by chance, when trying to demonstrate 2$^\mathrm{nd}$ harmonic D heating in TFR [32]: Here, exceptional good absorption was found, which was later then explained by a small amount of residual hydrogen present in the machine. Since hydrogen has half the ratio of q/m, it was resonant at the fundamental frequency, and absorbed the RF wave efficiently. This heating scheme is called H-minority scheme, and it is very frequently used in present-day fusion devices. In particular, it is the standard ICRH scheme at ASDEX Upgrade.

However, in a future fusion reactor, this heating scheme will not be a good choice: High-energetic α-particles from fusion reactions have the same q/m ratio as deuterium

(4/2=2/1), and hence will also be resonant at the second harmonic in a H-minority regime. Due to their large Larmor radii, 2nd harmonic absorption will be very efficient for α-particles. However, further acceleration of α's must be avoided, because these particles will be difficult to confine then.

The forseen ICRH scenario for ITER will therefore be second harmonic heating of tritium, which has $q/A = 3/1$. Since ITER is expected to have higher temperatures than present-day devices, second harmonic heating should work already for thermal ions. For the plasma start-up, when temperatures are still low, it would be possible to enhance the heating by adding ^{3}He as minority, which is resonant at $n = 1$ in this scenario. However, ^{3}He is very rare and expensive, so the benefits of this method must be evaluated and compared to the costs.

For the success of ITER, it will be important to understand the physics of 2nd harmonic ICRH. This gives the motivation to study it on present-day machines. On ASDEX Upgrade, it can be studied using D neutral beam injection, which provides the necessary large Larmor orbits. 2nd harmonic ICRH should then result in a further acceleration of the beam ions, and this can be studied and analyzed.

2.4.3 Orbit effects during ICRH

The Kennel-Engelmann operator, which we have discussed in the previous sections, was derived assuming a homogeneous magnetic field. We will discuss now heuristically the effect of orbits in a (inhomogenous) tokamak field configuration. As mentioned before, ICRH increases dominantly the perpendicular velocity $v_\perp$ of ions. This leads to an enhanced amount of trapped ions. On a banana orbit, the parallel velocity is close to zero near the banana tips. If a trapped ion has its banana tips close to the ICRH resonance, it passes through it very slowly. Hence, those ions get heated most efficiently and mark the maximum in the distribution function.

A heuristic model distribution function, which models this phenomena in a zero-orbit-width approximation[1], is given in [33, 34]

$$f(E,\mu,\rho) = \left(\frac{m}{2\pi}\right)^{3/2} \frac{n_{\mathrm{fi}}(\rho)}{T_\perp(\rho) T_\parallel^{1/2}(\rho)} \cdot \exp\left[-\frac{\mu B_c}{T_\perp(\rho)} - \frac{|E-\mu B_c|}{T_\parallel(\rho)}\right] \tag{2.85}$$

Here, ρ is any radial coordinate (e.g. ρ_{pol}), μ is the magnetic moment and B_c is the magnetic field at the ICRH resonance. The distribution function is given in terms of the constants of motion in the zero-orbit-width limit:

$$\begin{cases} E = const \\ \mu = \frac{E(1-\xi^2)}{B} = const \\ \rho = const \end{cases} \tag{2.86}$$

This model distribution is representative for pure ICRH heating (e.g. without NBI). At the resonance position, it is essentially a bi-Maxwellian with perpendicular and parallel temperatures $T_\perp$ and $T_\parallel$ (see fig. 2.22b). For each energy-slice, the maximum of the

[1] i.e. the ions are assumed to move along flux surfaces (i.e. along $\rho = const$), and the ∇B and curvature drifts are neglected

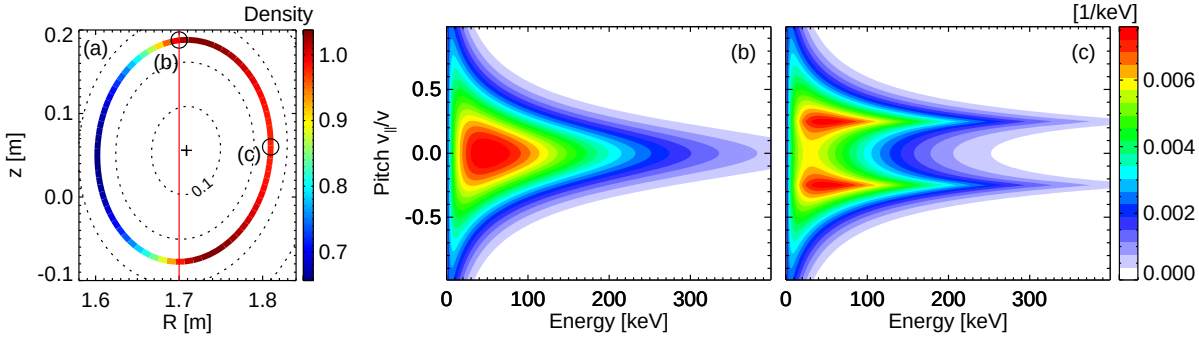

Figure 2.22: Illustration of eq. (2.85) for $T_{\parallel} = 10$ keV, $T_{\perp} = 100$ keV and $n_{\mathrm{fi}} = 1$ on a flux surface with $\rho_{\mathrm{pol}} = 0.25$. The ICRH resonance position is shown in (a) with a red line. The model results in a poloidal density variation, which is shown in (a) with the color scale. The resulting distribution function $F(E, \xi)$ is shown for two positions on the flux surface (b)+(c).

distribution function is found at $\xi = 0$, and this corresponds to ions which have their banana tip exactly at the resonance position. The formation of this maximum is called *resonance localization* [35, 36], and it can be explained because the parallel velocity is low close to the banana tips. Hence, trapped ions, which have their banana tips close to the ICRH resonance layer, are most effectively accelerated since they spend a longer fraction of their orbit within the resonance position.

The distribution function at the low field side of the same flux surface is shown in fig. 2.22c. In the zero orbit width limit, all ions stay on the flux surface, but their pitch ξ changes to ensure magnetic moment conservation. Here, the banana orbits with their tips at the resonance layer reappear with pitches $\xi = \pm 0.25$ and the distribution function has two maximums at these pitch-values. This basic shape is very typical for ICRH distribution functions, and it is often identified with "rabbit ears". In the zero orbit width approximation, the rabbit ears are symmetrical with respect to $\xi = 0$, because the "inner" and "outer" leg of a banana orbit lies actually on the same flux surface (leading to $\min \xi = -\max \xi$). Taking orbit widths into account leads then to a slightly more complex shape, where the rabbit ears can be asymmetric (w.r.t. the absolute values).

2.4.4 ICRH modeling codes

TORIC-SSFPQL

The full-wave TORIC [37] code simulates propagation and absorption in plasmas of radio-frequency (RF) waves in the ion-cyclotron (IC) range of frequencies. It solves the finite–Larmor–radius wave equation in frequency domain (nonhomogeneous Helmholtz equation),

$$\nabla \times \nabla \times \vec{E} = \frac{\omega^2}{c^2} \left[\vec{E} + \mathrm{i} \, \frac{4\pi}{\omega} \left(\vec{J}_{\mathrm{p}} + \vec{J}_{\mathrm{a}} \right) \right] \tag{2.87}$$

with $\vec{J}_{\mathrm{p}}$ the RF-induced plasma currents and ω the angular frequencies of the waves excited by the currents $\vec{J}_{\mathrm{a}}$ flowing in the conductors of the antennas. It solves the wave equation in arbitrary axisymmetric toroidal geometry.

To describe the impact of the wave absorption on the distribution function of the resonant species, TORIC is coupled to the steady-state Fokker-Planck SSFPQL solver for ions [38]. SSFPQL looks for the steady-state solution of the surface-averaged Fokker-Planck equation in (v, ξ) in the zero-orbit-width approximation. The numerical method is spectral in ξ (with Legendre polynomials as basis functions since they are eigenfunctions of the pitch-angle part of the collisional operator) and cubic finite elements in v. SSFPQL can solve the FP equation in the simultaneous presence of ICRF and NBI sources [39]. The NBI sources are calculated with SINBAD code [22].

The distribution functions calculated by SSFPQL can be directly used in TORIC to evaluate the coefficients of the wave equations. This allows a consistency loop between the two codes [40], which is particularly important in scenarios like D(H) minority scheme with D-NBI sources. In fact, in these scenarios there is a competition in absorbing RF waves between the minority hydrogen at the fundamental ion-cyclotron resonance and the fast ions of the NBI source at the first-harmonic ion-cyclotron resonance. Since the coupling TORIC-SSFPQL solves a non-linear problem, the number of iterations depends also on the coupled RF power.

ICRH modeling with TORIC/TRANSP

The TRANSP code has also included TORIC to simulate ICRH physics. Hereby, the effect of second harmonic heating on the beam ion distribution function can be calculated. The approach is different compared to TORIC-SSFPQL, because TRANSP/NUBEAM is based on Monte-Carlo simulations: A Monte-Carlo kick operator is used to describe the effect of the electric fields calculated by TORIC on the fast-ions from NBI. The resulting distribution function is given as output.

In contrast, TRANSP does not deliver the minority distribution function as output. However, perpendicular and parallel temperatures of the minority species are given, and hence the minority distribution function can be estimated using a Bi-Maxwellian.

3 The ASDEX Upgrade tokamak

3.1 Overview

The ASDEX Upgrade (AUG) tokamak [41] is situated in Garching at the Max-Planck Institut für Plasmaphysik (IPP) and went into operation in 1991. It features a major radius of 1.65 m and a minor radius of 0.5 m, which makes it a medium-sized tokamak. The 16 toroidal field coils are able to create a toroidal magnetic field in the typical range of 1.8 to 3.0 T. The poloidal magnetic field is created by a central transformator coil, which allows to induce plasma currents I_p in the range of 0.6-1.4 MA for plasma discharges of up to 10s length.

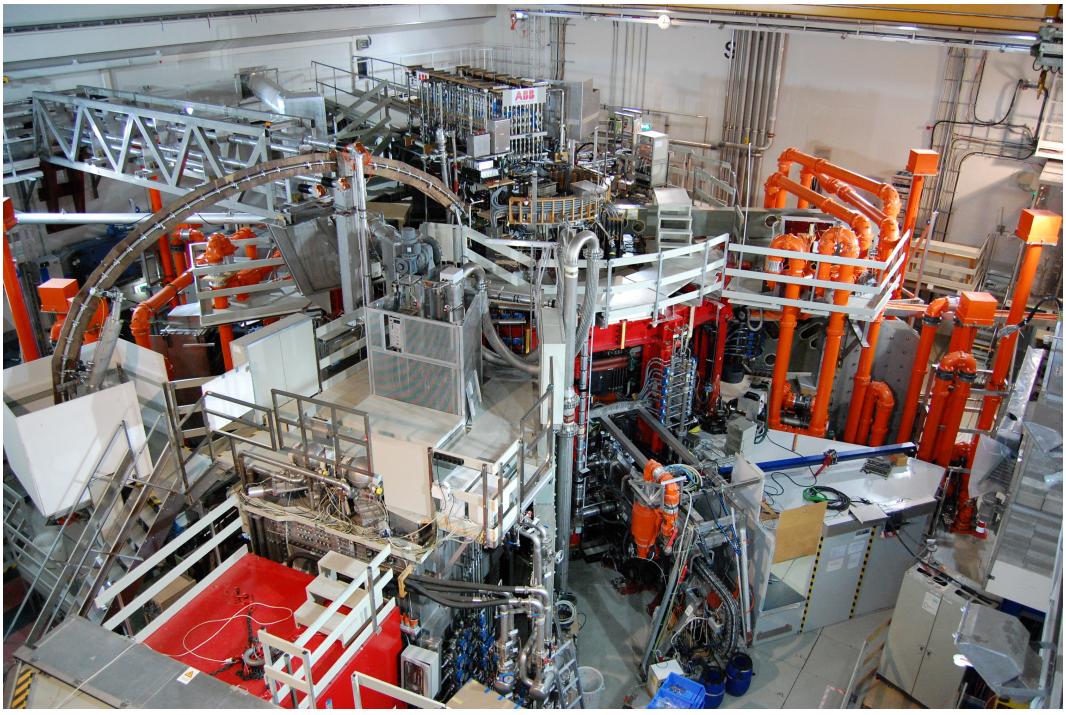

Figure 3.1: The torus hall of ASDEX Upgrade.

The name of ASDEX Upgrade originates from its predecessor ASDEX, which was in operation at the IPP from 1982 to 1990. ASDEX stands for 'Axial Symmetrisches Divertor EXperiment', which indicates that it was one of the first tokamak experiments with a divertor configuration instead of a limiter configuration. In the limiter configuration, the plasma boundary is defined by limiter tiles mounted in the main chamber, and the last closed flux surface has the same topology as the inner flux surfaces. The plasma-wall interaction takes place close to the main plasma, such that impurities from the wall can enter the plasma easily. The divertor configuration uses additional coils to deform the last closed flux surface and produce an X-Point (comp. fig. 3.2). In doing so, the plasma-wall interaction is spatially separated from the main plasma, leading to much

cleaner plasmas. In ASDEX, this concept was studied in perfection with two divertor chambers below and above the main chamber, that separated the plasma-wall interaction completely from the main plasma, leading to extremely clean plasmas. In a future reactor, such separated divertor chambers are not possible. Due to engineering, maintenance and radiation protection constraints, the divertor coils must be placed outside of the vacuum vessel. This lead to a divertor concept inside the main chamber, which is successfully studied at ASDEX Upgrade. Apart from allowing clean plasmas, the divertor concept gave rise to one of the most important discoveries in fusion research: The discovery of a high-confinement plasma regime (*H-mode*) at ASDEX, where the turbulent radial transport is supressed in the edge region. The H-mode allows strongly increased plasma densities and temperatures and soon became the forseen baseline scenario for future fusion devices such as ITER. The success of the divertor concept was so striking, that all other major tokamak devices adopted this concept, even though their vacuum vessel was initially not designed for it.

Another influential research program was started in 1996: the tungsten program. Initially, the first wall of ASDEX Upgrade was entirely made of carbon tiles, which was the most common material for fusion experiments. At the same time, it became clear that carbon is not suited for a reactor, because it reacts chemically with hydrogen isotopes. This leads to intolerably high erosion rates. In addition, radioactive tritium can be bound in hydrocarbons which leads to an increased radioactive inventory and decreases the safety advantages of a fusion reactor. As an overcome, ASDEX Upgrade investigated the usage of tungsten-coated tiles. The main disadvantage of tungsten is, that it is a high-Z element which is not fully ionized even in the core plasma and thus radiates and cools the plasma very strongly. Hence, only small concentrations in the range of 10^{-4}-10^{-5} are tolerable. In order not to endanger the successful experiment operation of ASDEX Upgrade, the carbon tiles were replaced by tungsten-coated tiles in small steps, during each machine opening. This process continued over more than a decade, and in 2007 the last carbon tiles were replaced with tungsten substitutes, such that AUG was a full-tungsten machine from then on. Good plasma performance and clean plasmas could be demonstrated in the full tungsten machine, which lead to the decision that ITER will use tungsten as divertor material. [42, 43]

3.2 Additional heating systems

ASDEX Upgrade has a very powerful and flexible heating system. Besides ohmic heating from the plasma current, AUG plasmas can be heated by ion and electron cyclotron heating (ICRH/ECRH) and neutral beam injection (NBI). The installed power adds up to 33 MW. In practice, 24 MW have been demonstrated, which marks a world record in terms of power over major radius $P/R = 15$ MW/m and this is in particular the closest achieved value compared to the forseen P/R of ITER.

3.2.1 Neutral beam injection

The neutral beam injection (NBI) system at AUG consists of two boxes with each four sources. Injection of several isotopes is possible, such as hydrogen, deuterium and helium. The properties of the beam parameters (e.g. power and maximum acceleration voltage)

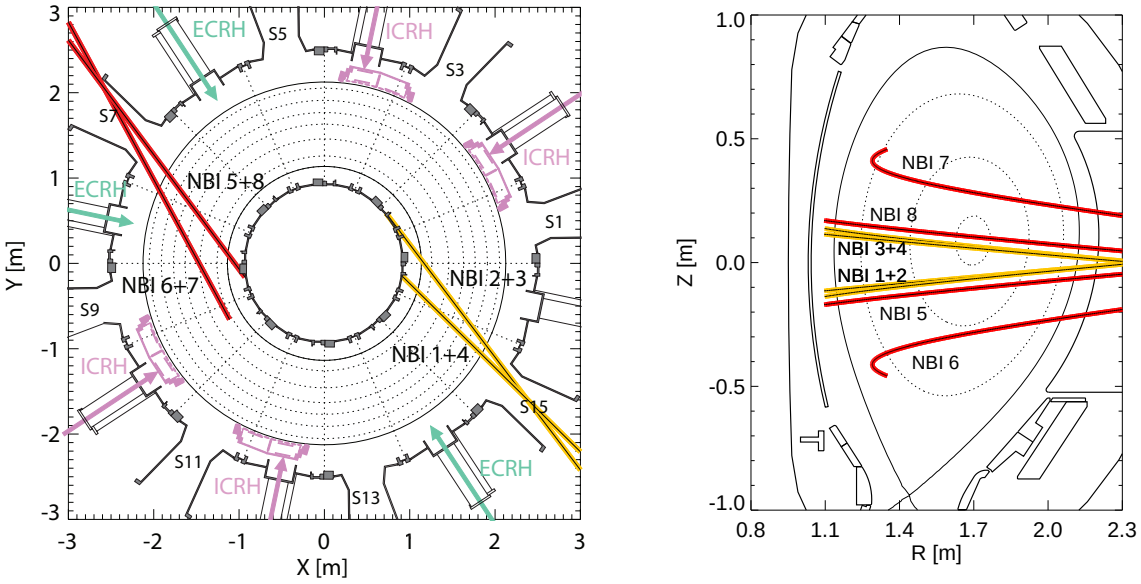

Figure 3.2: Top-down and poloidal view on the ASDEX Upgrade tokamak indicating the different heating sources. [13]

depend on the used species. In this thesis, we use solely deuterium injection, for which all sources have a maximum power of 2.5 MW. The beams of box 1 are labeled with Q1-4 (where Q stands for 'Quelle') and have a maximum acceleration voltage of $U = 60$ kV, while the beams of box 2 are labeled Q5-8 and accelerate with voltages up to $U = 93$ kV. The resulting energy of the injected neutral deuterium atoms is given by $E = eU$ (i.e. 60 keV or 93 keV, respectively). However, the ion source in the injectors emits also D_2 and D_3 molecules. They run through the same acceleration voltage, such that an individual D atom gets only half ($E = 1/2 \cdot eU$) or one third ($E = 1/3 \cdot eU$) of the nominal acceleration energy. Thus, a deuterium neutral beam consists of a full, half and third energy component. For box 1, the according species mix is approximately 0.47 : 0.36 : 0.17 and for box 2 it is 0.43 : 0.39 : 0.18.

The geometry of all sources is shown in fig. 3.2. All sources except Q6-7 are aligned close to the magnetic axis to allow NBI heating in the plasma center. Q6-7 are more off-axis and tangential, which is beneficial for neutral beam current drive (NBCD). Of particular importance for this thesis is NBI Q3, because it serves as diagnostic beam for FIDA, ion temperature and plasma rotation measurements based on charge exchange recombination spectroscopy.

3.2.2 Ion cyclotron resonance heating

The ion cyclotron resonance heating (ICRH) system at AUG is based on four generators that deliver 2 MW each, with frequencies in a range of 30-100 MHz. The produced voltage is transmitted to the antennas through rigid coaxial cables (painted orange on the outside and thus easily visible in fig. 3.1). AUG has four antennas inside the vacuum vessel (see fig. 3.2). As discussed in section 2.4, plasma heating is based on the so-called fast wave, which is evanescent below a certain plasma density cut-off. To reach the plasma, the wave must tunnel through that evanescent layer, such that the antenna must be positioned

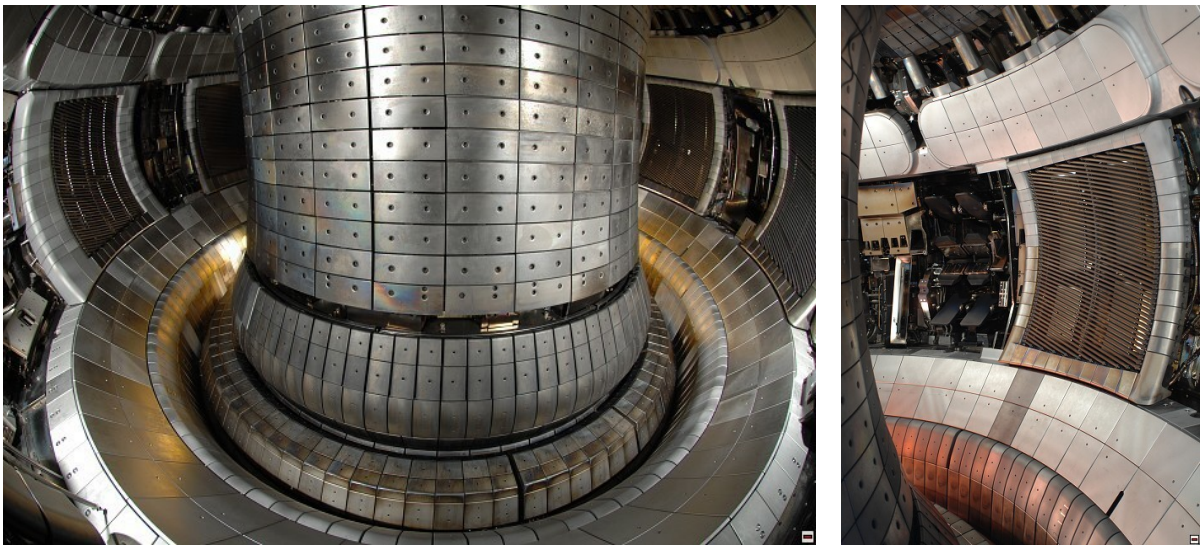

Figure 3.3: Photographs from the inside of ASDEX Upgrade. In the right photo, an ICRH antenna and steerable mirrors of the ECRH are seen.

closely to the separatrix for efficient coupling. To protect the antennas from the plasma, limiter tiles are mounted all around it. Faraday shielding stripes in front of the antenna shield static electric fields.

The standard heating scheme is minority heating of hydrogen, which is typically present in AUG plasmas with concentrations of around 5 %. The resonance condition is given by equation (2.67). It can be adjusted by varying the frequency or the magnetic field strength. Frequently used frequencies are 30.0 MHz and 36.5 MHz, which correspond to central, on-axis heating for a magnetic field strength of 2.0 T and 2.4 T, respectively.

3.2.3 Electron cyclotron resonance heating

The electron cyclotron resonance heating is the electron counterpart of ICRH. I.e., it accelerates electrons based on the same resonance condition (2.67) with the electron cyclotron frequency ω_{ce} instead of the ion cyclotron frequency ω_{ci}. Due to the low electron mass, the needed frequencies are much higher and the vacuum wavelength is much smaller ($\approx$2 mm, typically called microwaves). At ASDEX Upgrade, 105 GHz or 140 GHz are used, which corresponds to central second harmonic heating for 1.875 T and 2.5 T, respectively. It has to be noted that relativistic effects play an important role for electrons, such that the equations (such as (2.67)) should be corrected for relativistic effects to achieve precise results.

The microwaves are generated directly by gyrotrons and are transmitted via waveguides to the plasma torus. Due to the low wavelength, narrow wave beams can be accomplished that deposit their energy in a well-defined and narrow plasma region. The beam geometry and hence the deposition position can be steered flexibly with turnable mirrors that allow both a poloidal and toroidal tilting.

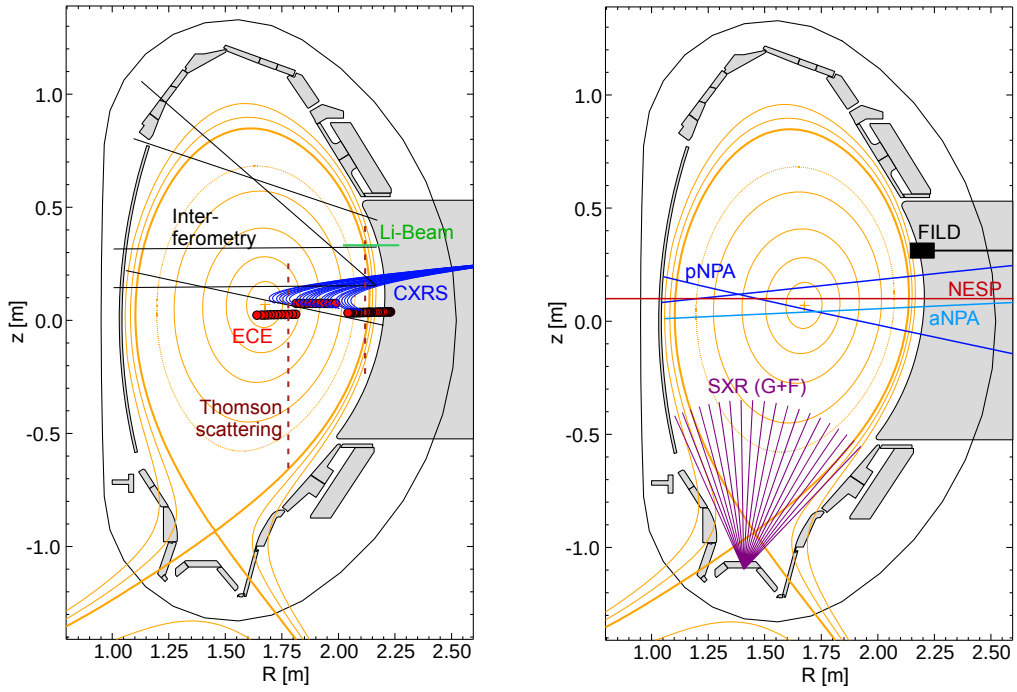

Figure 3.4: Poloidal geometry of diagnostics used in this thesis. Left: Kinetic profiles, right: fast ions and soft-X-ray.

3.3 Diagnostics

Over the more than two decades of operation, more and more plasma diagnostics have been installed in ASDEX Upgrade to monitor the plasma behavior, such that ASDEX Upgrade can be considered as an extremly well diagnosed tokamak. For each plasma discharge, a typical data amount of 30 GB is recorded (as of 2015). In the next section, we discuss the most important diagnostics used in this thesis.

3.3.1 Kinetic profiles

Electron density

The line-integrated central electron density n_e can be measured with plasma interferometry. At AUG, a DCN (deuterium cyanide) laser with a wavelength of 195 µm is injected into the plasma on five lines of sight (see fig. 3.4). The plasma causes a phase shift, which is proportional to the line integration of n_e. The phase shift is determined by analyzing the interference pattern with a reference path that does not pass through the plasma. In addition to that, n_e can be measured with Thomson scattering [44]. Therefore, an infrared Nd:YAG-laser is injected into the plasma, and n_e can be inferred from the intensity of the scattered light. At the plasma edge plasma, a Lithium beam is used to measure n_e with high spatial resolution to resolve the density pedestal which forms in H-mode. n_e profiles are obtained by fitting these diagnostics altogether.

Electron temperature

The electron temperature T_e can be measured by the electron cyclotron emission (ECE) diagnostic. A gyrating particle experiences a permanent acceleration, which results in the emission of electromagnetic radiation at the gyrofrequency and its low harmonics. This radiation is observed by the ECE diagnostic along a line of sight. The gyrofrequency depends on the magnetic field, which varies in a tokamak with approximately $1/R$. Hence, the spectral resolution of the ECE diagnostic translates into a radial resolution and if the former is good enough, well localized measurements are possible. Typical measurement positions of the ECE diagnostic at ASDEX Upgrade are shown in fig. 3.4, but they depend obviously on the individual magnetic field strength in a given discharge.

The plasma can be considered optically thick at the resonance position, such that the electron cyclotron emission can be described as black-body radiation. In present-day fusion devices the Rayleigh-Jeans approximation holds, such that the radiation intensity at angular frequency ω is given by: $I = \omega^2/(4\pi^2 c^3) T_e$. Consequently, T_e can be determined from the radiation intensity.

In addition, T_e can be inferred with the Thomson scattering diagnostic, from the Doppler-broadening of the scattered laser light.

Ion temperature and rotation

The ion temperature and rotation is measured using charge exchange recombination spectroscopy (CXRS). Like the FIDA technique (further explained in section 4.1), it relies on the charge exchange process between a donor neutral D^0 and the ion species of interest. While the FIDA technique aims for fast ions, here impurity ions I (with charge Z) are studied:

$$I^{Z+} + D^0 \longrightarrow I^{(Z-1)+*} + D^+ \tag{3.1}$$

After charge exchange, the impurity ion is with a high probability in an excited state $I^{(Z-1)+*}$ (keeping its momentum), and the subsequent light emission can be analyzed spectroscopically. Impurities are chosen for this analysis under the assumption, that they have a similar temperature and rotation as the main ions. The temperature can be determined by the Doppler broadening of the emission line, and the rotation is given by the rigid Doppler shift of the whole peak. In addition, the density of the analyzed impurity species can be inferred from the peak intensity. In contrast, the emission spectra of the main ions are much more complicated (as an example, the D_α spectrum is further discussed in section 4.1.2).

The neutral beams deliver the donor neutrals for the charge exchange (active contribution), which allows well localized measurements by choosing appropriate line of sights through a given neutral beam. In addition, a passive contribution originating from donor neutrals localized at the cold plasma edge has to be taken into account in the data analysis.

We use mainly the so-called CER diagnostic, which is aligned on NBI Q3 (as the FIDA diagnostic) and features 25 radial channels (spanning from the magnetic axis to the plasma edge on the low field side, see fig. 3.4) and a time resolution of up to 3.5 ms.

Effective charge

The effective charge of a plasma is defined as:

$$Z_{\text{eff}} = \frac{\sum_k n_k Z_k^2}{\sum_k n_k Z_k} = \sum_k \frac{n_k Z_k^2}{n_e} \tag{3.2}$$

where the index k corresponds the ion species. Z_{eff} is needed as input for TRANSP and FIDASIM. Bremsstrahlung is proportional to Z_{eff} (comp. eq. 4.4), such that it is in principle possible to infer line integrated Z_{eff} values from the bremsstrahlung background visible in spectra in the optical range (such as in the FIDA diagnostic). However, this evaluation method suffers from spurious background signals originating from outside the plasma (e.g. wall reflections). Thus, the Z_{eff} values from this method are typically too high.

Another method is the direct measurement of the individual impurity densities n_k by CXRS. On AUG, impurity density profiles of boron, carbon and nitrogen can be measured simultaneously. These densities can be plugged into eq. (3.2) to calculate a Z_{eff} estimate. Since also other impurity species can be present in the plasma (e.g. oxygen), this approach delivers a lower boundary of Z_{eff}.

For the analyzes in this thesis, educated guesses were used for Z_{eff}, which lie in between the two estimation approaches mentioned above.

3.3.2 Fluctuation measurements

Plasma instabilities result in fluctuations in the frequency range of several kHz and higher. To detect these plasma instabilities, measurements with high time resolution are required. Conventional CXRS diagnostics for T_i, rotation or the FIDA diagnostic have temporal resolutions in the order of some milli-seconds, and thus are too slow. In the following we discuss the fluctuation diagnostics used in this thesis.

T_e fluctuations

The ECE diagnostic has a temporal resolution of up to 1 MHz. With its good spatial resolution, it is suited for measuring the radial structure of fluctuations. In addition, AUG is equipped with a 2D ECE imaging system, which consists of a 2D arrangement of 16 (vertical) x 8 (radial) measurement positions, covering 40x10 cm. This can be used to study the poloidal structure additionally. Recently, a second 2D array has been installed at a different toroidal position which allows to study the toroidal structure furthermore.

Soft-X-Ray

The Soft-X-Ray (SXR) diagnostic measures electromagnetic radiation emitted by the plasma in an energy range above 1 keV along a large set of lines of sight (≈ 200 in total). The lines of sight are defined geometrically by pinhole cameras. Radiation below 1 keV is filtered with 75 µm thick beryllium foils. The radiation emerges from bremsstrahlung as well as from line- and recombination-radiation (mostly by tungsten). The time resolution is up to 2 MHz.

n_e fluctuations: Reflectometry

Electron density fluctuations can be measured with high temporal resolution by reflectometry. The main principle is similar to interferometry: The interaction between electromagnetic waves and the plasma is used to infer information about n_e. The main difference is the wavelength range. Here, RF millimeter waves are used, which corresponds to typical frequencies between 10-300 GHz. The waves are injected into the plasma with antennas. Unlike in interferometry, these waves cannot pass through the entire plasma but witness an n_e-dependent cut-off from which they are reflected back to a reciever. n_e fluctuations lead to fluctuations of the cut-off position. This leads to a change of the optical path length which can be detected by comparing the signal phase between antenna and reciever.

3.3.3 Fast-ion diagnostics

ASDEX Upgrade is equipped with a comprehensive set of fast-ion diagnostics. The main fast-ion diagnostic used in this thesis is the fast-ion D-alpha (FIDA) diagnostic, which is discussed in detail in the next chapter. In the following, we describe the other fast-ion diagnostics, which are used in this thesis.

Fast-ion loss detector (FILD)

A fast-ion loss detector (FILD) is a particle detector based on scintilator plates, which is positioned on a movable probe arm such that its position can be optimized for a given plasma discharge scenario. At present, three FILDs are available at ASDEX Upgrade, while two more are forseen to be installed. The signal can be increased by moving the FILD closer to the plasma, while at the same time putting it too close would result in overheating and possible damage to the detector. The geometry features a narrow entry slit and the scintillator plate is aligned such that it is only reached by gyrating ions and not by neutral atoms moving in a straight line. Hence, a FILD measures fast ions that are on lost or nearly-lost orbits, i.e. orbits which come close to the first wall or intersect it. The point of impact on the scintillator plate yields information about the gyro-radius and pitch. The light emitted from the scintillator is recorded by with high spatial (and thus velocity-space) resolution by a CCD camera with a moderate frame rate between 25 and 100 Hz. In parallel, it is measured through an optical fiber bundle, connecting a preselected array of fields on the scintillator to a set of photomultipliers. The latter approach yields a much better time resolution (1 MHz) at the expense of velocity-space resolution. The high time resolution allows to measure fast-ion fluctuations (e.g. due to MHD instabilities) and we use this technique in section 5.3.

Neutral particle analyzer

Neutral particle analyzers (NPA) rely on charge exchange processes: Ions from the main plasma get neutralized, are thus no longer bound to the magnetic field and can be detected with a NPA positioned outside of the plasma. The line of sight of the NPA (resp. its angle to the magnetic field) defines the pitch of the observed neutrals. The NPAs at AUG are in addition designed such that they can measure the energy spectrum of the incoming neutral particles. In total, three NPAs exist currently at AUG. Two of them rely on

passive charge exchange (comp. section 4.1.1) [45]. Through $\vec{E} \times \vec{B}$ mass separation, they are able to distinguish between deuterium and hydrogen, such that the ratio between the densities of both species can be measured. One of these two passive NPAs has a movable line of sight, which allows to adjust the measurement position both in real space and velocity space (pitch).

The third, recently installed active neutral particle analyzer (aNPA) [46] is aligned on NBI Q3 as source of donor neutrals, which allows a better spatial localization of the measurement compared to the passive NPAs. This active NPA uses a pulse height detection of the incoming neutrals to determine the energy spectrum which does not allow to distinguish between H and D.

Neutron rate and spectroscopy

Fast deuterium ions can also be studied indirectly, by analyzing the neutrons which they produce via fusion reactions. For D+D fusion, the following two reactions exist:

$$\mathrm{D} + \mathrm{D} \longrightarrow \begin{cases} {}^3\mathrm{He} + \mathrm{n} + 3{,}3\,\mathrm{MeV} \\ \mathrm{T} + \mathrm{H} + 4{,}0\,\mathrm{MeV} \end{cases}$$

whereby only the first reaction produces neutrons (n). The fusion cross-section increase strongly with ion energy (in the typical energy range of present-day devices), such that the neutron rate is in particular sensitive to fast ions. Several neutron rate detectors exist at ASDEX Upgrade with different sensitivities, to cover several orders of magnitude of neutron rates (ranging from very low values in e.g. ohmic discharges to high values in high power shots or shots with high fast-ion densities due to NBI and/or ICRH).

According to energy and momentum conservation, the neutron gets an energy of 2.5 MeV plus the initial center-of-mass energy of the D+D reactants. A measurement of the neutron energy spectrum allows consequently to infer information about the deuteron velocity distribution. Such a neutron spectrometer (NESP) has been recently installed on ASDEX Upgrade [47].

4 The new FIDA diagnostic at ASDEX Upgrade

(Parts of this chapter are published in [48])

4.1 Basic principle of the FIDA technique

In the following section, we discuss the basic principle, how the fast-ion distribution function can be measured with the FIDA technique. It is based on a charge exchange (CX) reaction:

$$\mathrm{D}^+_{\mathrm{fast}} + \mathrm{D}^0 \longrightarrow \mathrm{D}^{0*}_{\mathrm{fast}} + \mathrm{D}^+ \tag{4.1}$$

In such a reaction, a fast ion $\mathrm{D}^+_{\mathrm{fast}}$ collides with a *donor neutral* D^0 and exchanges its charge. Here, the donor neutral can be in an arbitrary atomic state (e.g. ground state or excited states). As a result of the reaction, the donor neutral is ionized (D^+) and the fast-ion is neutralized (D^{0*}_{fast}) with high probability into an excited state (denoted with the *). During such a charge exchange reaction, the momentum transfer is very low, such that the collision can be considered elastic. This is because the energy differences between the atomic states (< 13.6 eV for deuterium) are very low compared to the kinetic energies.

Hence, the *fast neutral* $\mathrm{D}^{0*}_{\mathrm{fast}}$ can be considered to have the same velocity vector $\vec{v}$ as the fast ion, just before it underwent the CX reaction. In other words, $\mathrm{D}^{0*}_{\mathrm{fast}}$ contains the same "information" as the initial fast ion, but it can be directly measured: On the one hand, it will emit light when it transitions to lower atomic states and, on the other hand, it is no longer bound to the magnetic field. The latter can be exploited by placing particle detectors onto the first wall (neutral particle analyzers). The light emission is the basis for the FIDA technique: The emitted light can be collected on well-defined lines of sight (LOS), and then analyzed spectroscopically. For the FIDA technique, the D_α transition ($n = 3 \rightarrow 2$) is analyzed, which has a wavelength of $\lambda_0 = 656.1$ nm. Fast ions can then be distinguished from thermal ions through their stronger Doppler-shift, which is discussed later in greater detail.

For quantitative analysis of the FIDA spectra modeling is needed. This is done with the FIDASIM [12, 13] code. It models neutral atoms by tracking Monte Carlo markers on a 3D grid. Therefore, the kinetic profiles and the equilibrium are needed as input. The interaction between the neutrals and the plasma is modeled via a collisional radiative model (4.2), which is explained later in detail. The code delivers two main outputs: First, the steady-state neutral density (atomic-state resolved) for all important neutral species involved in the FIDA process (i.e. donor neutrals and fast neutrals). Second, the D_α photon emission of those neutral atoms is calculated. In addition, synthetic FIDA and NPA diagnostics with realistic line-of-sight geometries are included. In the next sections, we will explain both the FIDA technique and its simulation by FIDASIM in greater detail.

In order for charge exchange diagnostics (such as FIDA) to work one needs donor neutrals in the first place. We will therefore discuss sources of donor neutrals in the following.

4.1.1 Donor neutrals

Active contribution

Beam neutrals

A very well-defined and strong source of donor neutrals is the injection of a neutral beam into the plasma. This can either be a low-power diagnostic beam, which is optimized for diagnostic purposes and does not perturb the main plasma significantly. Or one uses directly a heating neutral beam, which can of course not be considered non-perturbative any more. Since NBI heating is applied in most plasma experiments, this is an acceptable limitation. On ASDEX Upgrade, both approaches are realized: A purely diagnostic lithium-beam is used for edge measurements, which is strongly attenuated and does not reach the core plasma, and heating NBI beams are used for core CXRS measurements (comp. section 3.3.1). Since the FIDA diagnostic is intended to measure in the plasma core, it utilizes the latter approach and is aligned onto NBI Q3.

The neutrals injected by the beam can be calculated with FIDASIM. Figure 4.1a shows a contour plot of the neutral particle density injected by Q3 in the top-down view. Here, we have integrated over the z-direction and summed over all atomic states n=1-6, which are considered in the simulation. The beam enters the simulation grid at $X \approx 2.2$ m and propagates towards the separatrix without significant attenuation. After entering the plasma, it gets strongly weakened on its further way. Nevertheless, a sufficient number of neutrals reaches the magnetic axis (shown with a solid line), allowing measurements in the plasma core. To study the relevant processes, which cause the beam attenuation, in greater detail, we will briefly discuss the model implemented in FIDASIM.

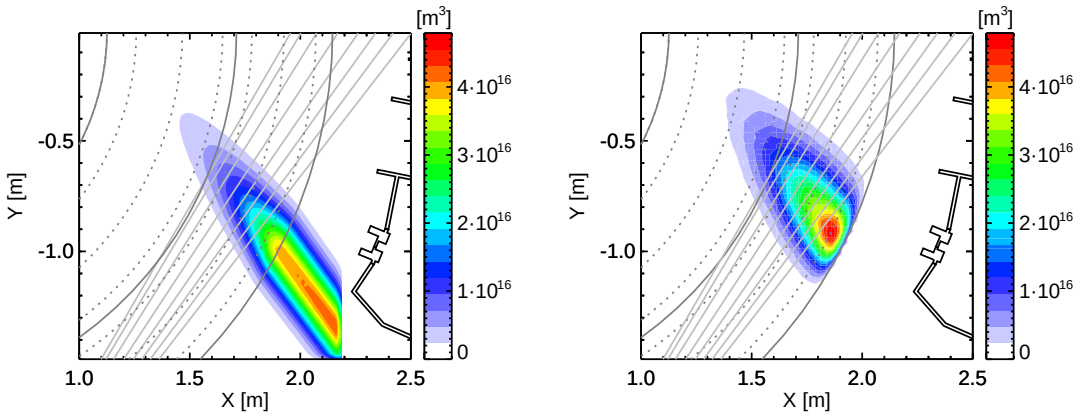

(a) Neutrals from NBI Q3 **(b)** Halo neutrals

Figure 4.1: Donor neutrals for active charge exchange radiation spectroscopy, shown in the top-down view. The neutral density is calculated by FIDASIM, summed over all considered atomic states $n = 1 - 6$ and integrated over the z-direction. The $\Phi \approx 10°$ lines of sight of the FIDA diagnostic are indicated with grey lines.

Simulation with the collisional radiative model in FIDASIM

In FIDASIM, the evolution of neutral atom Monte Carlo markers (of the beam, but also all other types of neutrals) is simulated with a collisional radiative model, which is

resolved for the atomic states H(n). Hereby, H can stand for any hydrogen isotope (since they have almost identical atomic structure), and n corresponds to the first quantum number (ignoring all further energy level corrections, such as fine structure etc.). The following processes are considered in the model:

$$\begin{aligned}
\mathrm{e}^- + \mathrm{H}(n) &\longrightarrow \mathrm{e}^- + \mathrm{H}^+ + \mathrm{e}^- && \text{electron impact ionization}\\
\mathrm{e}^- + \mathrm{H}(n) &\longrightarrow \mathrm{e}^- + \mathrm{H}(m) && \text{electron impact (de-)excitation}\\
\mathrm{H}^+ + \mathrm{H}(n) &\longrightarrow \mathrm{H}(m) + \mathrm{H}^+ && \text{proton charge exchange}\\
\mathrm{H}^+ + \mathrm{H}(n) &\longrightarrow \mathrm{H}^+ + \mathrm{H}^+ + \mathrm{e}^- && \text{proton impact ionization}\\
\mathrm{H}^+ + \mathrm{H}(n) &\longrightarrow \mathrm{H}^+ + \mathrm{H}(m) && \text{proton impact (de-)excitation}\\
\mathrm{I}^{Z+} + \mathrm{H}(n) &\longrightarrow \mathrm{I}^{(Z-1)+} + \mathrm{H}^+ && \text{impurity charge exchange}\\
\mathrm{I}^{Z+} + \mathrm{H}(n) &\longrightarrow \mathrm{I}^{Z+} + \mathrm{H}^+ + \mathrm{e}^- && \text{impurity impact ionization}\\
\mathrm{I}^{Z+} + \mathrm{H}(n) &\longrightarrow \mathrm{I}^{Z+} + \mathrm{H}(m) && \text{impurity impact (de-)excitation}\\
\mathrm{H}(n) &\overset{n>m}{\longrightarrow} \mathrm{H}(m) + \gamma && \text{spontaneous de-excitation}
\end{aligned} \tag{4.2}$$

Hereby, typically only one impurity species I with atomic number Z is considered (e.g. boron or carbon). The reaction probability of the first eight processes is modeled with cross-sections, that depend also on the relative velocity of the left-hand side collision partners. The ions and electrons on the left hand side are assumed to have a thermal distribution (according to their respective temperatures). The probability of spontaneous de-excitation is given by the Einstein coefficient [49] (as it is well-known from atomic physics textbooks), and a photon γ is emitted.

The neutral halo

The beam attenuation is caused by the ionization and charge exchange reactions. In contrast, the excitation (and spontaneous de-excitation) reactions will only cause a change of the atomic state of the beam neutrals. In FIDASIM, it is assumed that the beam neutrals enter the simulation grid in the ground state $n = 1$. The ionization reactions in (4.2) have only ions on the right hand side of the equation, such that the reaction products do not have to be further considered in the simulation. In contrast, the charge exchange reactions leave a new neutral on the right hand side: The beam neutral has become ionized, and the reaction partner (typically a thermal ion from the bulk plasma) has become a neutral. This gives rise to a (secondary) source of neutral atoms, which is called *halo* and must be considered in the simulation.

In the current versions of FIDASIM, only the right hand side of the proton charge exchange process is considered. The initial ion H^+ on the left hand side is assumed to have a thermal velocity distribution, and the resulting neutral on the right hand side H(m) keeps this velocity. Hence, the halo has in good approximation also a thermal Maxwell distribution (which is only slightly distorted by the velocity dependence of the cross-section). Obviously, this first generation of halo neutrals has to be further simulated. As they move through the plasma (along straight lines), they undergo the same processes described in the collisional radiative model (4.2). I.e., they may change their atomic state

due to excitation or de-excitation, get (re-)ionized through ionization reactions or perform another charge-exchange reaction with thermal ions. The latter leads to a new, second generation of halo ion, for which the same simulation has to be repeated iteratively. This iteration can be stopped at some point, because the halo density gets lower for increasing generation. In FIDASIM, 20 iterations are simulated by default.

The result of this halo calculation is shown in fig. 4.1b. It can be seen that the halo density is of the same order of magnitude as the beam density - in this example it is even larger. Hence, consideration of the halo is very important for quantitative analyses. Furthermore, it can be seen that the halo distribution is broader than the beam density. This is explained by the Maxwell distribution of the halo ions, which means that they fly into random directions before they get ionized again.

In principle, also the impurity charge exchange reaction yields a partially neutralized ion $I^{(Z-1)+}$, which can serve as donor for further charge exchange reaction. The main difference to the hydrogenic halo is however, that such an impurity halo is still bound to the magnetic field. In the current versions of FIDASIM, such an impurity halo is not considered, which should be a rational approximation if the impurity density is low (i.e. low Z_{eff}). Nevertheless, for the analysis of plasma discharges with high Z_{eff}, there might be room here for future improvements of the FIDASIM code.

In the terminology of CX, the CX-radiation resulting from beam and halo donor neutrals is called *active* contribution, because those neutrals were injected actively into the plasma. They can be well quantified (for example through such calculations with FIDASIM), and are well localized. Hence, active CX allows for well-localized and absolutely calibrated measurements. The contrast to that is the passive contribution, which we will discuss shortly in the next section

Passive contribution

Even in a hot and highly ionized plasma, a small fraction of neutral atoms will always remain. In tokamak plasmas, their density will be lowest in the hot plasma core, and rise strongly towards the colder plasma edge. Those neutrals can also act as donors for charge exchange, and this contribution is then called *passive*. Compared to the active CX, this process has several disadvantages: The passive background neutrals are not well localized as they exist everywhere in the plasma, and their absolute density is unknown and can only be calculated with large uncertainties.

4.1.2 The D_α spectrum

In the previous sections, we have discussed that the FIDA diagnostic uses (mainly) beam and halo neutrals from NBI Q3 as donor neutrals D^0 for the charge exchange process:

$$D^+_{\text{fast}} + D^0 \longrightarrow D^{0*}_{\text{fast}} + D^+$$

Following this reaction, the D_α transition ($n = 3 \rightarrow 2$) of the excited fast neutral D^{0*}_{fast} is analyzed by a spectroscopic measurement of the entire D_α spectrum. In the FIDASIM code, this process corresponds to the spontaneous emission $H(3) \rightarrow H(2) + \gamma$ in the collisional radiative model (4.2). We will discuss now the different components that comprise the D_α-spectrum.

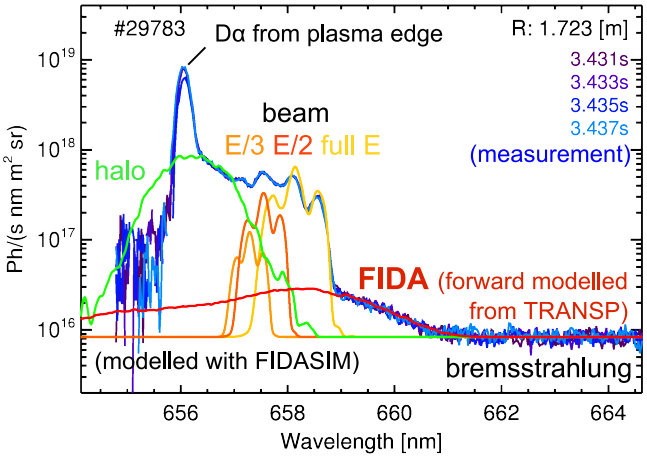

Figure 4.2: The D_α spectrum. Measured with the 2013 FIDA diagnostic setup, which allowed only to measure on one side of the D_α line (i.e. $\lambda \gtrsim 656.1$ nm).

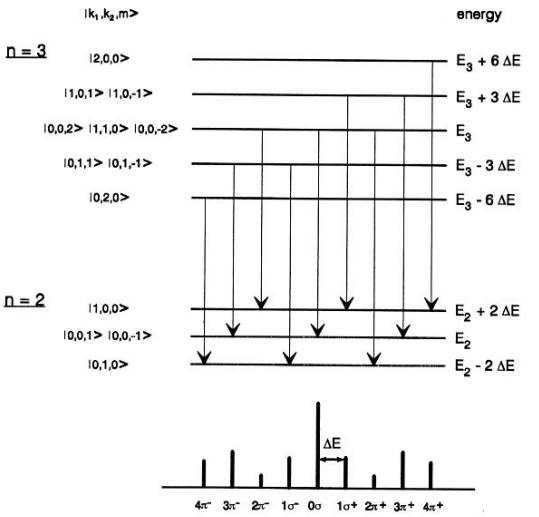

Figure 4.3: Energy level splitting due to the linear Stark effect, and resulting transitions allowed by selection rules.

Such a measured spectrum is shown in fig. 4.2 together with simulation results from FIDASIM. At 656.1 nm, the largest peak is seen, which corresponds to only weakly Doppler-shifted D_α radiation of thermal particles from the plasma edge, where temperatures are low and the passive neutral particle density is high. Furthermore, the beam neutrals, which perform a $3 \rightarrow 2$ transition, are directly seen. Here, each energy component is separately visible at different wavelengths. This is due to the Doppler-shift, which is given by the projection of the neutral velocity vector $\vec{v}_\mathrm{n}$ onto the line of sight unit vector $\hat{e}_\mathrm{los}$ (pointing from the optical head towards the plasma):

$$\Delta\lambda = \lambda - \lambda_0 = \lambda_0 \frac{\vec{v}_\mathrm{n} \cdot \hat{e}_\mathrm{los}}{c} \tag{4.3}$$

Since each beam component is mono-energetic, one would expect only one peak per energy component. Instead, each beam component is seen with a multi-peak structure. This is caused by the motional Stark effect. In general, the linear Stark effect causes the energy level of the n-th state to split into $(2n-1)$ separate energy components due to an external electric field $\vec{E}$. The reason for this is that the hydrogen atom has a non-zero electrical dipole moment $\vec{d}$, which gives rise to a perturbation term $\vec{d} \cdot \vec{E}$ in the Schrödinger equation. The resulting difference between the splitted energy levels depends linearly on $|\vec{E}|$. In a tokamak plasma, the static electric fields are too weak to cause a significant Stark effect. However, the ions see a strong electric field in their rest frame, because they move with their velocity $\vec{v}_\mathrm{i}$ through the magnetic field $\vec{B}$. This *motional* electric field can be calculated by a Lorentz transformation and it is given by $\vec{E} = \vec{v}_\mathrm{i} \times \vec{B}$.

The splitted energy levels for $n = 2$ and $n = 3$ are shown in fig. 4.3. Hereby, the energy difference is given by multiples of $\Delta E = \frac{3}{2} e |\vec{E}| a_0$ with a_0 being the Bohr radius. The resulting splitting of the D_α transition is also shown in fig. 4.3 for the nine transitions, which are allowed by the selection rules. In addition, six more transitions are possible, but their intensities are very weak. FIDASIM models all 15 transitions with fixed, tabulated

relative intensities. Due to the limited spectral resolution, we are not able to separate all those 15 lines, but we see mainly three peaks for each energy component of the beam.

Coming back to fig. 4.2, it can be seen that the halo neutrals are also seen directly in the spectra. Since they have a nearly thermal distribution, they appear as broad peak, and individual Stark components are not visible. In principle, it would be possible then to measure T_i from the width of the peak and the plasma rotation from the net shift with respect to $\lambda_0 = 656.1$ nm.

The background of the spectrum is determined by bremsstrahlung, which is emitted throughout the plasma: [50]

$$I(\lambda) = 7.57 \cdot 10^{-8} \cdot \frac{1}{\mathrm{s\,nm\,m^3\,sr}} \cdot \frac{\mathrm{nm}\sqrt{\mathrm{eV}}}{\mathrm{cm}^{-6}} \cdot \frac{g n_\mathrm{e}^2 Z_\mathrm{eff}}{\lambda\sqrt{T_\mathrm{e}}} \cdot \exp\left(\frac{-hc}{\lambda T_\mathrm{e}}\right) \tag{4.4}$$

$$\text{with: } g = 5.42 - (3.108 - \ln T_\mathrm{e}[\mathrm{eV}])(0.6905 - 0.1323/Z_\mathrm{eff})$$

The bremsstrahlung measured in a spectrum is given by the line integral over the line of sight. The bremsstrahlung depends only weakly on λ, at least in the wavelength window typically observed by the spectrometer. Hence, it can be considered as a flat line, and subtracted accordingly.

Finally, we move on in our description of the D_α spectrum towards the part, in which we are actually interested: The FIDA radation. In the spectrum, it can be distinguished from the halo and beam emission by its large Doppler-shift ($\Delta\lambda \gtrsim 3$ nm).

In order to simulate the FIDA radiation, FIDASIM needs the fast-ion distribution function as input. The distribution function gets translated into a set of Monte Carlo (MC) markers. Then, FIDASIM calculates the probability, that a given fast-ion MC marker is neutralized by charge exchange with the donor neutrals (i.e. beam and halo neutrals). The evolution of the resulting fast neutral MC marker is calculated again with the collisional radiative model (4.2). Ultimatively, emitted photons of the $3 \rightarrow 2$ transition are calculated and distributed among the lines of sight, that intersect with the current simulation grid cell.

In this context, it is worth to note, that the dominant process is charge exchange into the $n = 3$ state, followed by immediate spontaneous D_α emission. Other processes, e.g. charge exchange into an $n \neq 3$ state and later excitation of the $n = 3$ state, are of higher order and much less probable. This is beneficial for the achievable spatial resolution of the FIDA diagnostic, as one can assume that the FIDA radiation is emitted closely to the initial position of the CX reaction. In particular, the Einstein rate coefficient for the D_α transition is $4.41 \cdot 10^7\ \mathrm{s}^{-1}$. A typical NBI ion with $E = 60$ keV and pitch 0.5 has a parallel velocity of $1.2 \cdot 10^6$ m/s. In this case, D_α light is emitted on average only 2.7 cm away from the initial point, where the charge exchange reaction took place. The spatial resolution of the FIDA diagnostic at ASDEX Upgrade is discussed quantitatively in section 4.2.3.

The FIDASIM code can be used to forward-model synthetic FIDA signals from a given fast-ion distribution function. In this way, it can be tested, if the fast-ion distribution function matches the measurement. However, the FIDA Doppler spectrum can also be interpreted more directly, which we will discuss in the next section.

Interpretation of the FIDA spectra with weight functions

The main physical process which causes the shape of the FIDA spectra is the Doppler-shift. Further effects, like line splitting due to the motional Stark effect cause only a broadening of the emitted spectra of a given neutral, but not a rigid shift. The velocity vector of the fast neutral $\vec{v}_\mathrm{n}$ can be written in the same way as a fast-ion velocity vector (2.1):

$$\vec{v}_\mathrm{n} = v_\parallel \hat{e}_\parallel + v_\perp \cdot (\cos\gamma \hat{e}_{\perp 1} + \sin\gamma \hat{e}_{\perp 2}) \tag{4.5}$$

The difference to a fast ion is that $\vec{v}_\mathrm{n}$ remains constant, because neutrals are not bound to the magnetic field. I.e., they neither gyrate nor follow the field lines, but move in straight lines. If the D_α emission happens closely to the charge exchange reaction position, then $v_\parallel$ and $v_\perp$ are similar to the fast-ion velocity component, and γ is the gyroangle, which the fast ion had in the very moment it underwent the charge exchange.

The Doppler-shift observed by a given line of sight can be written in terms of the pitch and velocity by:

$$\Delta\lambda = \lambda_0 \frac{\vec{v}_\mathrm{n} \cdot \hat{e}_\mathrm{los}}{c} = \mathrm{sgn}\,\Phi \cdot \frac{\lambda_0 v}{c} \left(\xi \cos\Phi + \sqrt{1-\xi^2} \sin\Phi \cos\gamma \right) \tag{4.6}$$

Hereby, we have chosen $\hat{e}_{\perp 1}$ and $\hat{e}_{\perp 2}$ such, that $\hat{e}_{\perp 2} \cdot \hat{e}_\mathrm{los} = 0$ (without loss of generality). Φ is defined as signed angle between the magnetic field vector and the line of sight: $\Phi = \mathrm{sgn}(\hat{e}_\parallel \cdot \hat{e}_\mathrm{los}) \arccos |\hat{e}_\parallel \cdot \hat{e}_\mathrm{los}| \in [-90°, +90°]$. The sign of Φ indicates the direction of the Doppler-shift. The strongest Doppler-shift is seen, if $\vec{v}_\mathrm{n}$ is parallel (or anti-parallel) to the line of sight $\hat{e_\mathrm{los}}$, i.e. $\cos\Phi = \pm\xi$. This means, that $|\Phi|$ is an important parameter, which determines the observed region of the velocity space.

However, besides for $\xi = \pm 1$, there is no one-to-one relation between the Doppler-shift and the 2D velocity coordinates (v, ξ) of the fast ion, because the gyrophase γ plays an important role. A fixed Doppler-shift $\Delta\lambda$ can originate from an entire set of (E, ξ) combinations, due to the gyromotion. Further effects like the Stark-splitting even increase this ambiguity.

The observed region in the velocity space can be quantified with the so-called weight functions W. They are defined such, that a given wavelength bin λ of the FIDA spectrum can be interpreted as an integral over $F(E, \xi)$, weighted with W:

$$FIDA(\lambda) = \int_0^\infty \int_{-1}^{+1} W(\lambda, E, \xi) F(E, \xi)\, \mathrm{d}E \mathrm{d}\xi \tag{4.7}$$

W can be calculated with the FIDASIM code [12]. Approximate analytic derivations for the weight functions are derived in [51]. In fig. 4.4, weight functions for one LOS with $\Phi = 10°$ and four different wavelength bins are shown as an example. It can be seen that all weight functions have a similar shape but cover different energy ranges. Higher Doppler-shifts $\Delta\lambda$ are connected with a weight function at higher energies, and different signs of the Doppler-shift correspond to opposite parts in the velocity space with respect to the pitch $v_\parallel/v$. The weight functions belonging to ± 3 nm (w.r.t. the unshifted D-alpha line $\lambda_0 = 656.1$ nm) typically mark the lower boundary of the FIDA spectrum. At lower Doppler-shifts, other contributions, e.g. from the NBI or the thermal halo neutrals become important or dominate the spectrum. Consequently, we analyze typically only

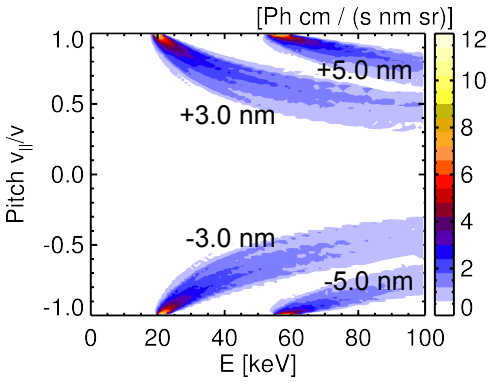

Figure 4.4: Weight functions for the $\Phi \approx 10°$ view (comp. fig. 4.6), for four different Doppler-shifts $\Delta\lambda$ with respect to the D-alpha line $\lambda_0 = 656.1$ nm.

the part of the Doppler-spectrum with $|\Delta\lambda| \gtrsim 3$ nm such that we can only measure the fast-ion velocity space above roughly 20 keV.

The weight functions can be interpreted as lines of sight (or areas of sight) in the velocity space. If enough weight functions are available, a tomographic reconstruction becomes feasible. If the spectrum in fig. 4.6 is binned to 0.1 nm wavelength bins, and if we study Doppler-shifts in a typical range of $\Delta\lambda \in \pm[3, 8]$ nm we get already ≈ 100 measurements and weight functions. However, they have all similar shape and do not cover the entire velocity space (especially the area around pitch 0 is not covered). Therefore, additional FIDA views with different projection angles Φ (i.e. the angle between the LOS and the B-field) are needed, which motivated the diagnostic upgrades carried out within this thesis. In the following sections, we will discuss the setup of the FIDA diagnostic at ASDEX Upgrade and the recent upgrades, which were made.

4.2 Diagnostic setup

4.2.1 Spectrometer

The FIDA diagnostic is based on the spectroscopic analysis of the D-alpha Doppler spectrum. The unshifted D-alpha line is typically very intense and cannot be measured simultaneously with the much weaker FIDA emission due to the limited dynamical range (16 bit) of the CCD-Camera. Therefore, it needs to be blocked. In the previous spectrometer setup (as described in [52]), this was achieved with a high pass interference filter. The drawback of this method is that only one half of the FIDA Doppler-spectrum can be measured (in that case the red-shifted part, comp. fig. 4.2). In order to gain information about the full fast-ion velocity space, it is desirable to measure the full Doppler spectrum. Therefore, a sharp notch filter with a width of approximately 1-2 nm is needed. Since optical filters with these capabilities are rare and expensive, the D-alpha line is instead filtered geometrically with a wire, as it was already succesfully done e.g. in [53, 54]. Therefore, an additional lens is needed to create a sharp image on the wire. The complete setup is shown in fig. 4.5. The light is transferred from the plasma into the spectrometer by a vertically stacked array of glass fibers. It is then made parallel by the first lens and gets reflected and dispersed by the grating. The second lens focuses the light onto

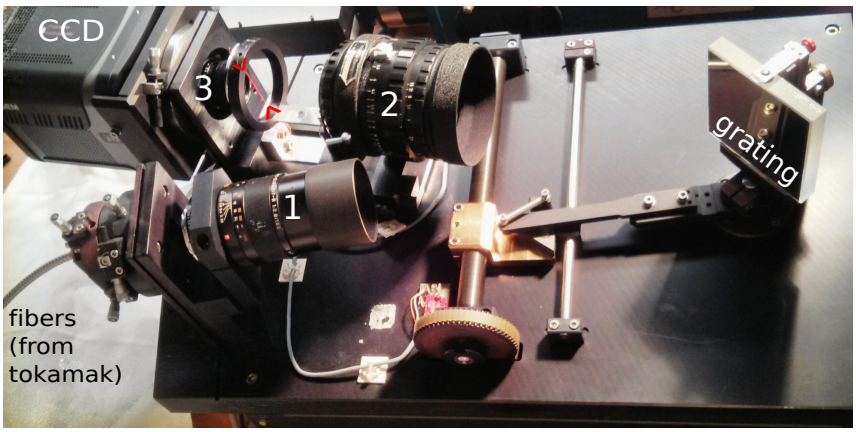

Figure 4.5: The FIDA spectrometer at ASDEX Upgrade. The grating has 2000 lines/mm and the focal lengths of the three lenses are: $f_1 = 180$ mm, $f_2 = 150$ mm and $f_3 = 25$ mm. The wire (to block the D_α-line) is marked with red arrows and has a width of 0.8 mm.

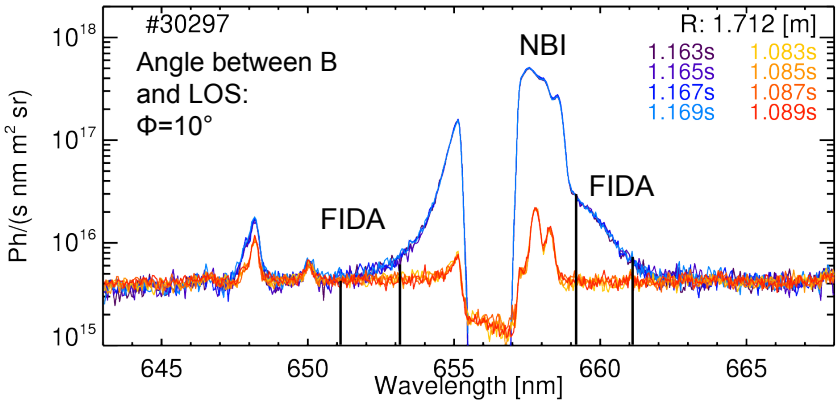

Figure 4.6: D-alpha spectrum measured with the new spectrometer setup. For the wavelengths marked with vertical lines, the corresponding weight functions are shown in fig. 4.4. The red curves correspond to the passive background radiation, measured during a NBI-off phase.

the wire, whose position has to be adjusted such that it blocks the central D-alpha line. Then, the light is focused onto the CCD-chip with the third lens.

The wavelength calibration of the spectrometer is done by measuring the known spectrum of a neon lamp on each spectrometer channel (before and after an experimental campaign). Furthermore, the same neon lamp spectrum is measured on the first spectrometer channel after each tokamak discharge to ensure that the wavelength calibration is valid for every discharge. The neon lamp is located in the spectroscopy laboratory (i.e. close to the spectrometer), and it is assumed that the wavelength does not change on the further optical path from the plasma.

The spectrometer setup as described in [52] has been capable of measuring 16 LOS channels. Within the spectrometer upgrade, this has been extended to 27 channels, which can be measured with a time resolution of 2.5 ms. This increase has been achieved, because the modified optics have been chosen such that the image projected onto the CCD is smaller. Consequently, the observable wavelength range has increased by a similar

factor (≈ 25 nm instead of ≈ 14 nm), which is beneficial for measuring both the blue and red side of the Doppler spectrum. In addition, a second spectrometer with a similar design and 10 channels (20 ms time resolution) has been brought into operation permanently for FIDA measurements, which gives us the possibility to routinely measure 37 lines of sight simultaneously.

A spectrum measured with the upgraded spectrometer is shown in fig. 4.6. The wire-filter is clearly seen, and covers the central D-alpha line entirely, as desired. The beam emission is still visible, and FIDA light can now be observed on both sides of the spectrum. The spectral resolution is 0.21 nm. For comparison, a background spectrum, measured during an NBI-off phase, is shown with the red lines. It is shifted to similar background (evaluated around 665 nm) to allow a shape comparison. It can be seen that the background is mainly a flat line, which can be identified with bremsstrahlung, with some additional impurity lines. The FIDA contribution can hence be well recognized by its shape.

4.2.2 Lines of sight

As described in [52], the FIDA diagnostic at ASDEX Upgrade had already line of sight arrays from three viewing directions: $\Phi \approx 10°, -20°, 70°$ (all aligned on NBI beam Q3). The minus symbol indicates that the observation is done from the opposite direction with respect to the magnetic field, which means that the Doppler spectrum is mirrored with respect to the D-alpha line. Since we are able to measure both sides of the Doppler spectrum, the sign of Φ does not matter for the information, which we get about the velocity space. This line of sight setup has now been extended to five views. The new lines of sight are chosen such that the measurements complement the three existing views in the best possible manner. To determine the optimum new angles Φ_1 and Φ_2 between the lines of sight and the magnetic field, we calculate synthetic spectra for the three existing views and two new views at observation angles Φ_1 and Φ_2 for the fast-ion velocity distribution function of beam Q3. We then calculate tomographic inversions of the synthetic spectra with added noise for the possible combinations of the angles Φ_1 and Φ_2 and compare the inversion with the original function by a figure of merit $Q = |f - f_{\mathrm{tomo}}|^2 \,/\, |f|^2$, where $|\cdot|$ represents the two-norm of a vector holding the function values of f. Optimum viewing angles for the two new views are the global minima of this figure of merit in fig. 4.7 at about 85 and 50 degrees. Local maxima correspond to a poor choice of the new geometry and occur when Φ_1 or Φ_2 are similar to one of the existing viewing angles or similar to each other. We note that the graph is symmetric about the angle bisector $\Phi_1 = \Phi_2$ as Φ_1 and Φ_2 are interchangeable.

Hence, two new viewing arrays with $\Phi \approx -50°$ and $\Phi \approx -85°$ have been installed into ASDEX Upgrade (see fig. 4.8). The $\Phi \approx -50°$ view is equipped with seven radial lines of sight, and the $\Phi \approx -85°$ has five radial lines of sight. The third (middle) LOS of $\Phi \approx -85°$ turned out to have a bad fiber with low transmission, and is not shown in the figure. The exact projection angle changes over the different radial LOS of one view. Figure 4.9 shows an overview of the projection angles of all five views as a function of the major radius R. It can be seen that the angle of one LOS array varies along the plasma radius due to the geometrical arrangement of the viewing chords. It is therefore not possible to achieve an optimal Φ distribution over the whole plasma radius. We have optimized the

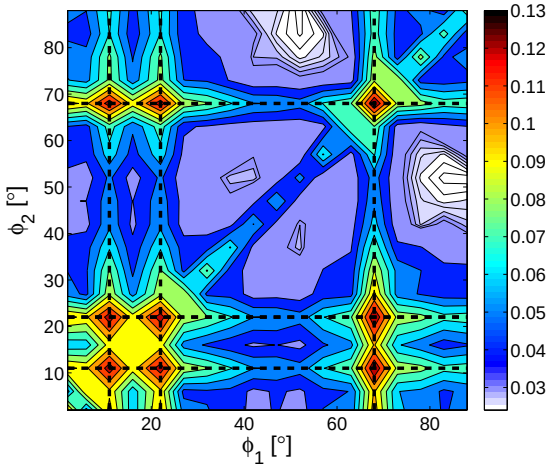

Figure 4.7: Figure of merit $Q = |f - f_{\mathrm{tomo}}|^2 / |f|^2$ between original fast-ion distribution f and calculated tomography f_{tomo}. The tomography has been calculated from five FIDA views: The three existing ones ($\Phi \approx 10°, -20°, 70°$) and two new views Φ_1 and Φ_2. Φ_1 and Φ_2 have been varied to determine the optimal angles for the new views. The angles of the three existing views are marked with dashed lines. The global minimum and hence the optimal angles are found for $\Phi_{1,2} \approx 50°, 85°$. A local minimum is found for $\Phi_{1,2} \approx 40°, 52°$, but it is clearly less optimal than the global minimum.

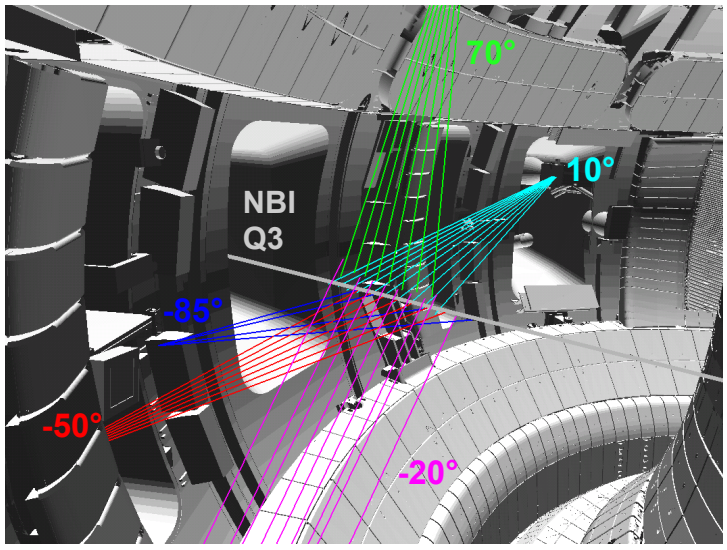

Figure 4.8: 3D visualization of the five FIDA line of sight arrays, along with the approximate angle Φ between the most central line of sight of each array and the local magnetic field. Negative angles indicate that the observation is from the opposite side, and hence the Doppler spectra are mirrored. It can be seen that all lines of sight are well aligned along NBI source Q3.

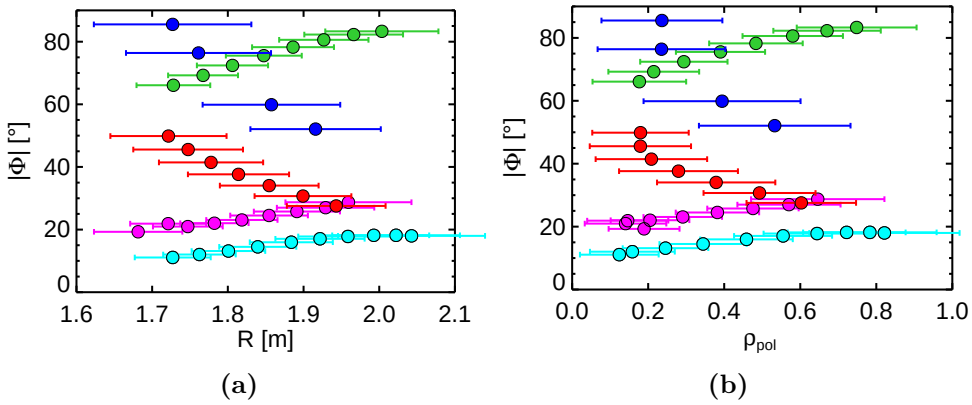

Figure 4.9: Absolute value of the angle between the line of sight and the magnetic field $|\Phi|$, for all lines of sight, plotted as a function of (a) major radius R and (b) normalized poloidal flux radius ρ_{pol}. The error bars correspond to the radial resolution (see section 4.2.3). The five viewing arrays are marked with different colors (corresponding to fig. 4.8). The magnetic axis is located at $R = 1.72$ m.

LOS angles in the plasma center, and the Φ angles mentioned above correspond to the values in the plasma center.

In the default setup, the LOS of the $\Phi = -20°$ view are connected to the spectrometer with 20 ms time resolution, while the other four viewing arrays are connected to the spectrometer with the faster CCD-camera (2.5 ms). If data analysis using all five views is desired, the data from the faster CCD-camera is typically averaged over 20 ms to reduce noise and to have a comparable time range for all measured spectra.

4.2.3 Radial resolution

The radial resolution of a line of sight is mainly determined by the path of the LOS through the NBI beam. The width of the LOS can hereby be neglected in good approximation, and the width of the NBI beam and the surrounding neutral halo is the important quantity. Good radial resolution (in terms of ρ_{pol}) can be achieved if the LOS goes tangential to flux surfaces through the beam.

With the FIDASIM code, the radial resolution can be computed accurately. In particular, the origin of fast ions, which experience a charge-exchange reaction and contribute to the calculated FIDA signal can be calculated and is shown in fig. 4.10. The calculation has been done for typical ASDEX Upgrade discharge parameters and a fast-ion distribution calculated by TRANSP/NUBEAM [19, 20] resulting from 2.5 MW of 60 keV NBI from source Q3. For comparison, the neutral density of NBI and halo is plotted with contour lines. It can be seen that the FIDA measurement volume is localized where the LOS crosses the neutral cloud. However, there is also a significant broadening of the contribution perpendicular to the LOS, which can be explained by finite Larmor radii of the fast ions and finite free mean paths of the fast neutrals.

From these R,z contribution matrices, we can compute a R and ρ histogram. We define our measurement position with its mean-value, and the width of the measurement with the standard deviation of the histogram. Both are shown in figure 4.9, together with the angle of the line of sight towards B. We can see that the $\Phi = 10°$ and $\Phi = 20°$ views have

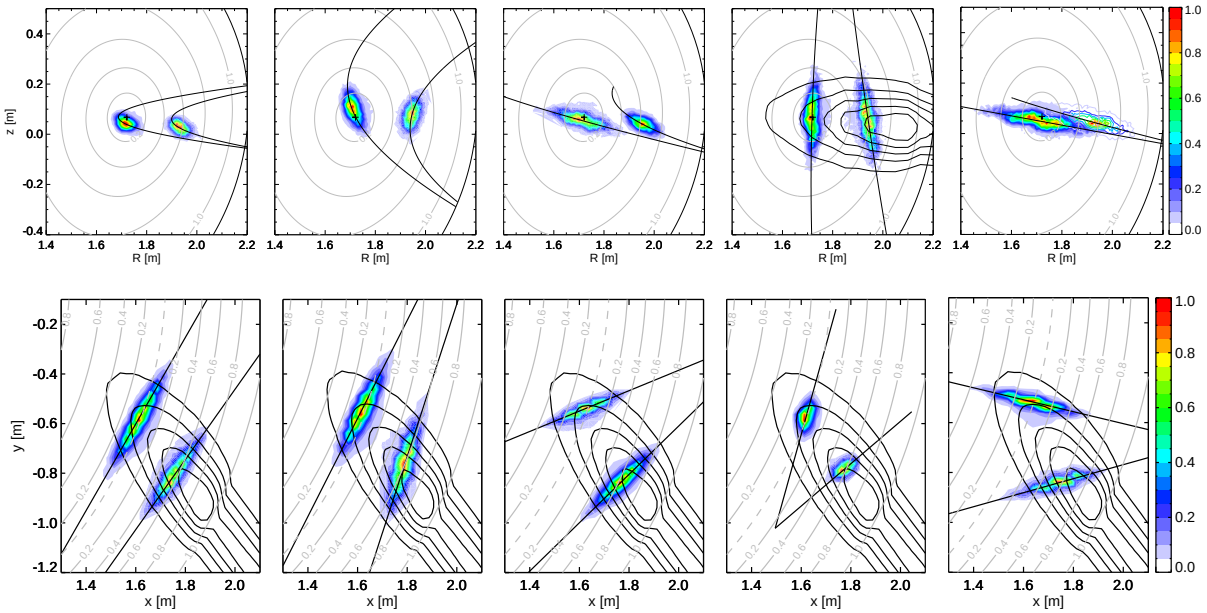

(a) $\Phi \approx 10°$ **(b)** $\Phi \approx -20°$ **(c)** $\Phi \approx -50°$ **(d)** $\Phi \approx 70°$ **(e)** $\Phi \approx -85°$

Figure 4.10: The origin of fast ions, which do a charge-exchange reaction and contribute to the calculated FIDA signal is shown as colored contour on a normalized scale. This can be interpreted as the radial resolution of the FIDA diagnostic. Top: poloidal cross-section, bottom: Top-down view. The geometrical lines of sight are drawn with a continuous line, and normalized poloidal flux radius is shown in gray contours. For comparison, the sum over all neutral densities (i.e. beam + halo neutrals and all atomic states) are drawn with black contours in some of the plots.

the best resolution both in R and ρ because they are very tangential to the flux surfaces. $\Phi = 70°$ has a comparably good R resolution, because its lines of sight are vertical. However, the ρ-resolution is worse, especially in the plasma center, because the neutral beam covers a broad ρ-range there. $\Phi = 50°$ is less tangential as $\Phi = 10°$ and $20°$ and has a ρ resolution comparable to the vertical view. $\Phi = 85°$ has the broadest measurement volume, because it is least tangential to the flux surfaces, and has consequently only five radial lines of sight.

4.2.4 Weight functions of the five FIDA views

The weight functions of all five FIDA views are shown in fig. 4.11 as an example for a positive and a negative Doppler-shift. It can be seen that the 10° view observes ions with high pitches, and the weight functions have a rather narrow shape. The other extreme case is the 85° view, which dominantly observes strongly gyrating fast ions with pitches in a rather broad range around zero. It can be seen that its weight functions are much broader due to the strong influence of the gyromotion on the projected velocity. For the views in between, the shape of the weight functions changes smoothly according to the absolute value of Φ. The weight functions at negative Doppler-shifts are approximately mirror-symmetric with respect to $v_\perp/v$ if compared to the ones at positive Doppler-shifts. In particular, Doppler-shifts $\Delta\lambda$ with $\Delta\lambda \cdot \operatorname{sgn}\Phi > 0$ correspond to FIDA light from co-current fast ions, while $\Delta\lambda \cdot \operatorname{sgn}\Phi < 0$ corresponds to counter-current fast ions.

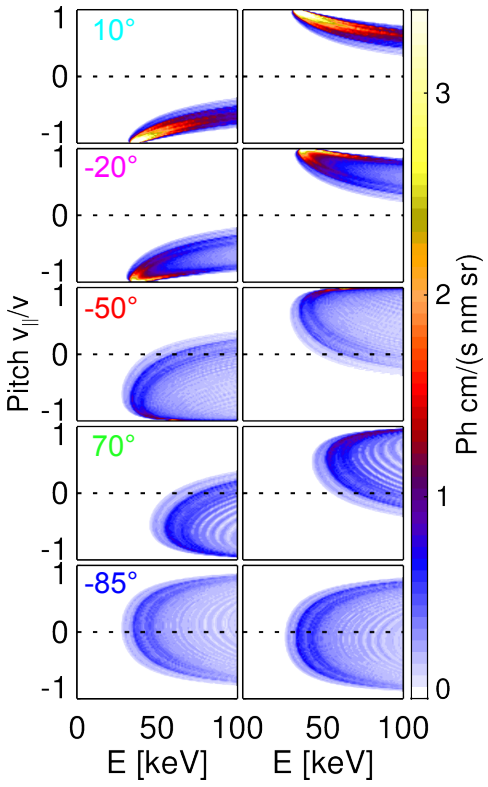

Figure 4.11: Weight functions of the five FIDA views and two Doppler-shifts with $\Delta\lambda = \pm 3.9$ nm. The plots are aligned such that the left column fulfills $\Delta\lambda \cdot \operatorname{sgn}\Phi < 0$, and the right column fulfills $\Delta\lambda \cdot \operatorname{sgn}\Phi > 0$.

4.3 Tomographic reconstruction of the velocity distribution

In order to calculate a tomographic reconstruction of the velocity distribution $f(E, \xi)$, we need to invert eq. 4.7. Therefore, we discretize the equation and stack all measurements in a vector $\vec{s}$, and all pixels of the 2D distribution function $f(E, \xi)$ in a vector $\vec{f}$. They are then connected by a matrix W, which contains the discretized weight functions:

$$\vec{s} = W\vec{f} \tag{4.8}$$

$\vec{s}$ and W are normalized with respect to the noise level σ of the measurement, such that parts of the spectra with good signal-to-noise ratio are considered more strongly. The task is now to calculate the pseudo-inverse W^+ of W, which can be done e.g. by singular value decomposition as shown in [55, 56] or by maximum entropy regularization [57]. A systematic comparison between different inversion methods can be found in [58]. Here, we use a first-order linear regularization, as described in [59]:

$$W^+ = (W^{\mathrm{T}}W + \alpha H)^{-1} W^{\mathrm{T}} \tag{4.9}$$

$$H = \beta\nabla_E^T \cdot \nabla_E + \nabla_\xi^T \cdot \nabla_\xi \tag{4.10}$$

With ∇_E and ∇_ξ we denote matrix representations of the partial derivative in E and ξ direction. To ensure dimensional consistence, the prefactor β is needed. This approach

is equivalent to calculating a least-squares fit, with the additional condition that the solution should be a smooth function, i.e:

$$\text{minimize } \tfrac{1}{2}\left\|W\vec{s}-\vec{f}\right\|^2+\alpha\cdot\vec{f}^{\mathrm{T}}H\vec{f} \tag{4.11}$$

The ratio between both conditions is given by the parameter α. β allows furthermore to adjust the ratio of smoothing in E and ξ direction. We find the tomographic reconstruction $\vec{f}$ then by the matrix multiplication:

$$\vec{f}=W^{+}\vec{s} \tag{4.12}$$

The so calculated tomography $\vec{f}$ can contain negative values. To overcome this non-physical behavior, we have implemented a simple yet effective iterative method: After the first step, the most negative pixels of $\vec{f}$ are determined. For each these pixels (index j), an artificial weight-signal pair is added (i.e. a new row to W and $\vec{s}$ with index i) fulfilling:

$$W_{i,j}=W_0,\ \text{zero elsewhere, and } s_i=0. \tag{4.13}$$

This means that an artificial weight matrix is introduced, which sees just one pixel, and the corresponding signal is set to zero. W_0 is a positive number and should be large with respect to the real weight functions. This forces the selected pixel (which was negative before) to zero. This procedure can be repeated iteratively, until all negative values are eliminated or the most negative value reaches a reasonable threshold close to zero. The underlying assumption of this method is that the velocity-space regions with most negative values of $\vec{f}$ (in the previous iteration step) contain most probably not any fast ions in reality.

5 Experimental results

(Parts of sections 5.1 and 5.2 are published in [48])

5.1 Fast-ion velocity distribution from 60 and 93 keV NBI

In the following section, we investigate the velocity-space accuracy of the tomographic reconstruction by comparing a phase with only 60 keV NBI and a phase with 93 keV beams in addition. We have chosen discharge #30950, which was run with a magnetic field of -2.2 T and a plasma current of 1 MA. It features rather low central electron densities between $1.0 - 3.0 \cdot 10^{19}$ m^{-3}, which leads to low bremsstrahlung and hence a good signal-to-noise ratio of the FIDA signal. The basic time traces are shown in fig. 5.1.

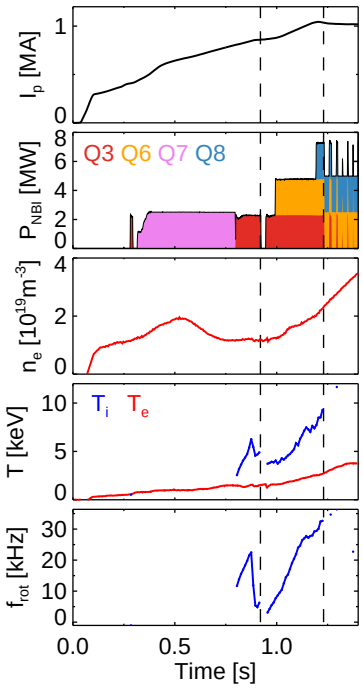

Figure 5.1: Relevant time traces of ASDEX Upgrade discharge #30950. From top to bottom: Plasma current, NBI power, electron density, electron and ion temperature, toroidal plasma rotation frequency. The time traces of the last three correspond to the radial position, where we calculate the FIDA tomography. The two time points, which we have analyzed are marked with vertical dashed lines. Q3 etc. denote the different NBI sources: Q3 is operated with 60 keV injection energy and Q6-8 are operated with 93 keV. Q6-7 are aligned more off-axis and tangential (see fig. 3.2), and hence contribute only weakly to the studied FIDA measurement position in the plasma center.

We have analyzed two time points: 0.92 s with only 60 keV NBI (from Q3), and 1.23s with 93 keV from Q6 and Q8 in addition. In between, there is a short time phase without any beam, which is used to subtract passive FIDA radiation. In fig. 5.2, the

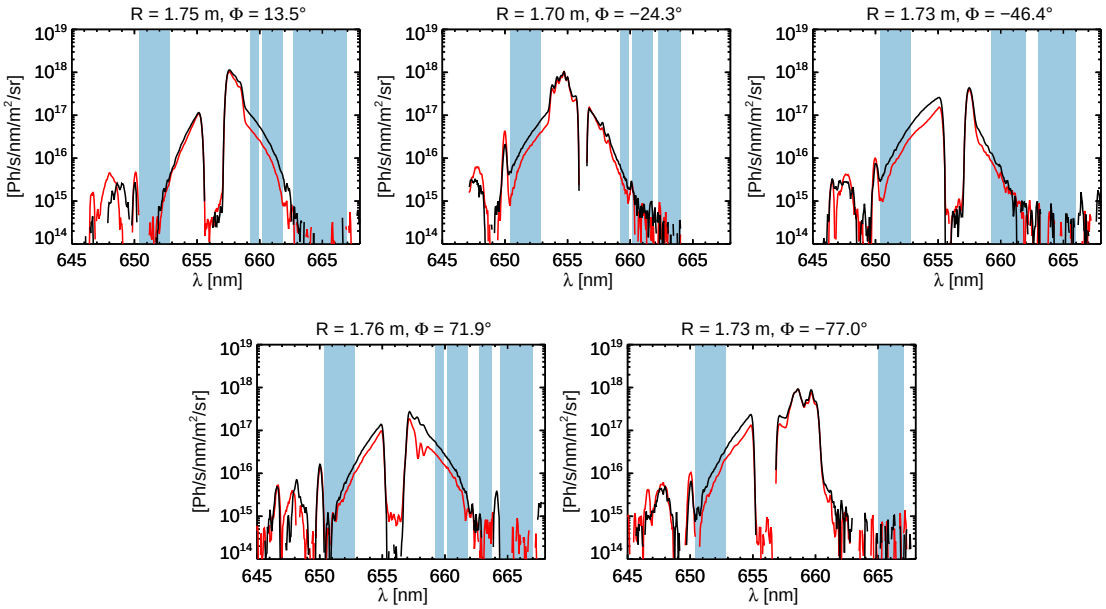

Figure 5.2: FIDA spectra of five views at $t = 0.92$s (60 keV NBI only, red line) and $t = 1.23$s (60 and 93 keV NBI, black line). Passive radiation (measured during a beam-off phase) has been subtracted - therefore, the baselines of the spectra appear very noisy in the logarithmic plot, as it is close to zero. The tomography is calculated from the blue-shaded regions.

FIDA spectra are shown for the two time points for five FIDA views, which measure all approximately at the same radial position in the plasma center ($R = 1.74$ m, $z = 0.07$ m and $\rho_{\mathrm{pol}} = 0.16, 0.10$ for the first/second time point). It can be seen directly from the spectra that the FIDA radiation increases strongly. This can be interpreted with an increase of the fast-ion density - however a quantitative statement cannot be given, because the beam attenuation has also changed due to different plasma parameters in the two time points. With the FIDA tomography, quantitative statements are possible, because this effect is taken into account by calculating separate weight functions for each time point. The presence of 93 keV fast ions should lead to larger Doppler shifts in the spectrum. This effect is visible in some of the spectra, but it is weak, because the 93 keV beams inject less particles than the 60 keV beams (at same power) and the charge exchange cross-sections go down towards higher energies.

We have performed tomographic reconstructions from these spectra. Regions with impurity lines and beam emission are excluded, as-well as the wavelength range [-3.1 nm, +3.1nm] around the D-alpha line, which is dominated by thermal ions, emission from the beam neutrals and passive radiation from the cold plasma edge. In doing so, we make sure that we get mainly information about the fast ions from the spectra. However, this also means that we do not get detailed information about fast ions below ≈ 20 keV. This limit seems to be acceptable, since still a broad region of the energy range is covered (2/3 in the case of 60 keV NBI and even more for 93 keV NBI). In addition, the thermal ions are well-diagnosed by conventional charge-exchange diagnostics.

The result of the tomography is seen in fig. 5.3. For $t = 0.92s$, the tomography yields a velocity distribution which has almost no fast ions above 60 keV. The pitch distribution

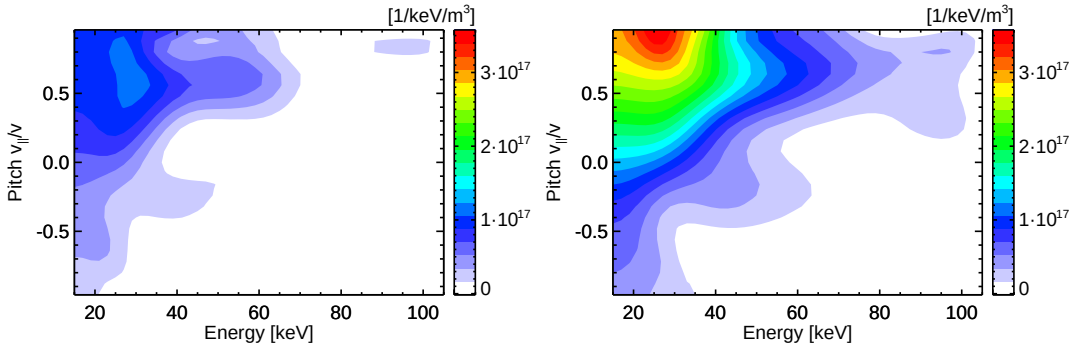

(a) $t = 0.92$ s **(b)** $t = 1.23$ s

Figure 5.3: Tomographic reconstruction of the ion velocity distribution function. The tomography is calculated on a 46x25 grid and has hence 1150 pixels, and 280 measurements (e.g. FIDA wavelength bins) are used.

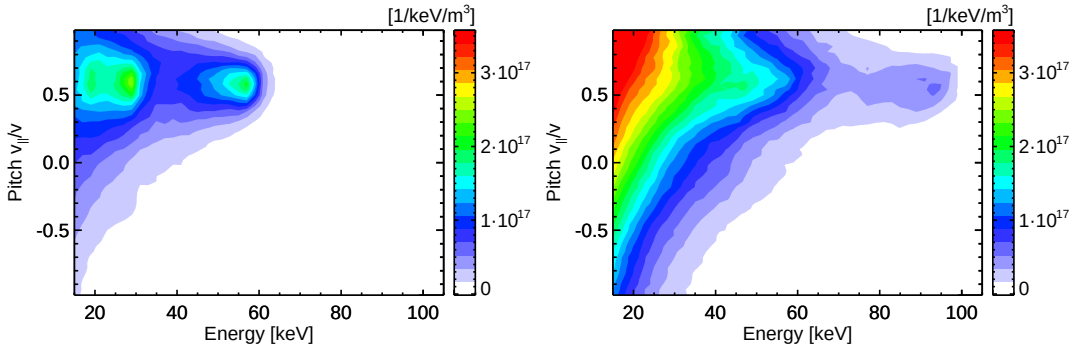

(a) $t = 0.92$ s **(b)** $t = 1.23$ s

Figure 5.4: Fast-ion distribution calculated by NUBEAM/TRANSP. The distribution of thermal deuterium is added according to eq. 2.9.

has a peak at ≈ 0.6, which is perfectly within expectations from the beam geometry. For the second time point, $t = 1.23s$, a clear contribution from fast ions above 60 keV is found. Moreover the fast-ion density increases strongly, which can be expected, because the NBI power is tripled. The tomography is calculated down to energies of 15 keV. It has to be noted that the region between 15 and 24 keV is more weakly covered by weight functions than the higher energy ranges, and the results within this region should be treated with care. This is especially true for 15-20 keV, which is only (partially) covered by some of the perpendicular views, and hence has an extrapolative character.

In fig. 5.4., the fast-ion distribution, calculated by the NUBEAM module in TRANSP [19, 20], is shown. To ensure a realistic comparison with the FIDA tomography, a shifted Maxwellian distribution (2.9) has been added to account for thermal deuterium (with temperature T_i and toroidal rotation v_rot taken from CXRS measurements).

The contour plots show a good agreement, overall. For a more quantitative comparison to the FIDA tomography, we have calculated energy and pitch profiles of the 2D distribution functions by integrating out the other coordinate (fig. 5.5). For the pitch profile, we have integrated over $E > 24$ keV, in order to compare only the trustworthy region of the tomographic reconstruction.

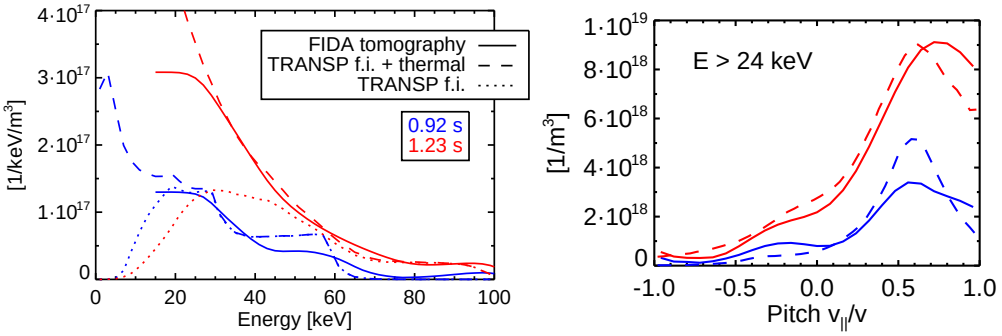

(a) $\int F(E,\xi)\mathrm{d}\xi$ **(b)** $\int_{E>24\ \mathrm{keV}} F(E,\xi)\mathrm{d}E$

Figure 5.5: Energy and pitch profiles calculated from the tomogram and the TRANSP ion distribution. $t = 0.92$ s corresponds to 60 keV NBI, while $t = 1.23$ s has 93 keV NBI in addition. In (a), the energy profile of the TRANSP fast-ion distribution (without thermal deuterium) is plotted for comparison.

In the pitch profiles, a good agreement is found both in absolute values and shape of the profile. The main difference is that the tomography shows less pronounced peaks. This effect is also seen clearly in the contour plots for $t = 0.92$ s (figures 5.3 and 5.4). It might be a consequence of the 1st order regularization, which demands small gradients. For this particular feature of the distribution function, regularization methods, which tend to pronounce peaks more strongly (e.g. Minimum Fisher information [59]), might improve the results. On the other hand, an exact reconstruction of the peaks is not so important from a physical point of view: The peaks are mainly determined by the (well-known) geometry of the NBI, while the interesting physics aspects are found elsewhere in the velocity space (e.g. high energy tails, fast-ion redistribution due to MHD etc.).

The energy profiles show also a good agreement in shape and absolute values. The strong increase of the measured fast-ion density at the second time point fits well to the TRANSP prediction. It can be seen that the thermal ions contribute a significant part to the distribution at $t = 1.23$ s due to high T_i values there and that the agreement is greatly enhanced by adding the thermal component to the TRANSP fast-ion distribution. Differences are found for $t = 0.92$ s: In the region around 50 keV the tomography yields less fast ions, and around 65 keV it yields more fast ions than TRANSP. This might be explainable to some extent with a too strong smoothing of the tomography. At $t = 1.23$ s, the extrapolative character of the tomography at energies below ≈ 24 keV can be seen clearly, and differences to TRANSP occur. For higher energies, the tomography and TRANSP agree very well.

Overall the tomography made from the FIDA data reproduces well the fast-ion distributions of NBI at two different injection energies, and good agreement to TRANSP/NUBEAM is found. The method can therefore be applied to investigate physics mechanisms.

5.2 Fast-ion redistribution by sawtooth crashes

Sawtooth crashes can strongly redistribute fast ions, which has been demonstrated e.g. from FIDA [60] or neutron measurements [61]. However, theoretic models [62–64] predict that the redistribution strength depends on the fast-ion velocity. In particular, fast ions

with high drift velocities are expected to be more weakly redistributed (details are discussed in section 5.2.3). With the improved FIDA setup and the additional views, it is now possible to investigate the velocity dependence of this redistribution experimentally.

5.2.1 Basic physics

Sawtooth crashes are periodic MHD-instabilities, that appear in regions where the safety factor q is below 1 (i.e. typically in the plasma core). In the region with $q < 1$, a (1,1) MHD mode (so-called kink mode) can exist (the so-called sawtooth precursor). During the crash itself, the mode suddenly grows on a fast timescale (of order ≈ 100 µs) and the magnetic field lines reconnect. This leads to a strong particle redistribution in the plasma core (inside the so-called mixing radius). The redistribution results in a mixing, such that temperature and density profiles get flattened. In central measurement channels of e.g. T_e, sawtooth crashes are seen then as a strong signal drop while outside of the so-called inversion radius the signals increase.

Sawtooth crashes can be described more quantitatively with the Kadomtsev model [65]. Therein, the magnetic reconnection of field lines is described with the helical flux Ψ^*. It is defined by introducing helical angle η, that follows the field lines on the resonant surface (here: the $q = 1$ surface, see fig. 5.6). Then, it is given by:

$$\eta = \theta - \varphi, \tag{5.1}$$

where φ is the toroidal and θ the straight field line angle [66, 67] (or in good approximation for the plasma core the poloidal angle).

The component of the magnetic field, which is perpendicular to this coordinate, is called helical field, and can be calculated by subtracting the component parallel to η from the total magnetic field:

$$\vec{B}^* = \vec{B} - (\vec{B} \cdot \hat{e}_\eta)\hat{e}_\eta \tag{5.2}$$

This helical field represents the difference in field line slope with respect to the resonant surface. In the typical situation, the field lines are more strongly curved inside of the resonant surface (i.e. $q < 1$) than outside of it (i.e. $q > 1$). Consequently, the $\vec{B}^*$ goes through zero and changes sign at the resonant surface. The sign change gives rise to magnetic reconnection of field lines which go in opposite direction (illustrated in fig. 5.7).

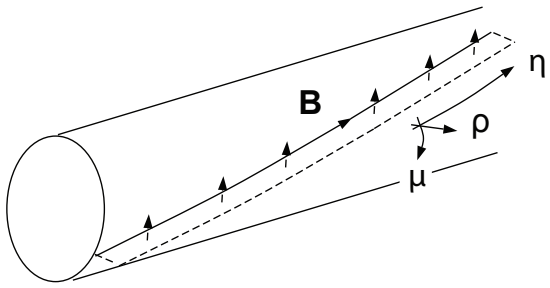

Figure 5.6: The helical angle coordinate η follows the magnetic field lines on the resonant surface. The helical flux Ψ^* is given by an integral of $\vec{B}$ over the dashed surface. [68]

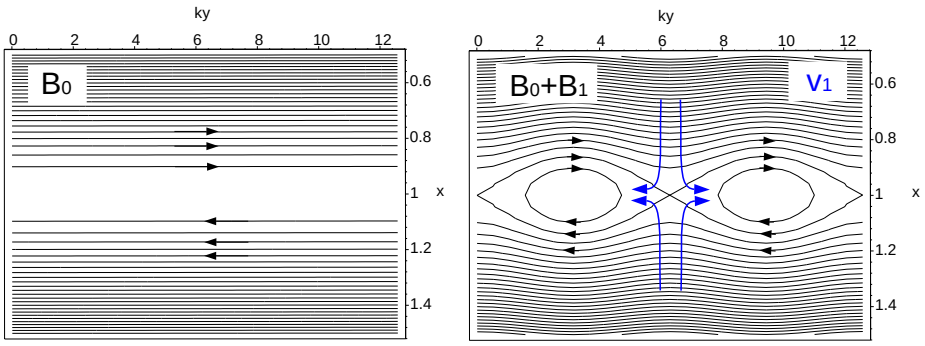

Figure 5.7: Illustration of magnetic reconnection. Magnetic field lines with opposite direction reconnect and form a magnetic island. [68]

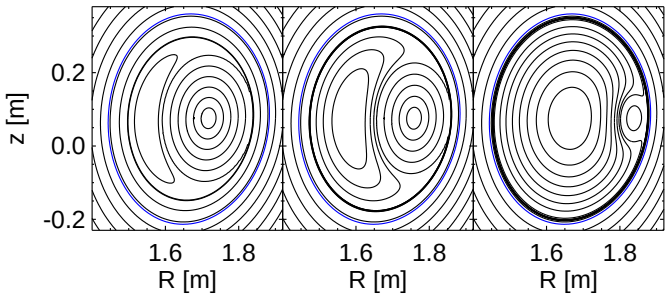

Figure 5.8: Temporal evolution (from left to right) of the helical flux Ψ^* during a sawtooth crash (as described by eq. (1) in [69]). The blue line indicates the sawtooth mixing radius.

The helical flux is defined as surface integral over $\vec{B}$ through the surface A indicated in fig. 5.6 with dashed lines.

$$\Psi^* = \int_A \vec{B} \cdot \mathrm{d}\vec{A} \tag{5.3}$$

Figure 5.8 shows the temporal evolution of the helical flux during a sawtooth crash with contour plots. The magnetic reconnection starts at the initial $q = 1$ surface, and a magnetic island forms. During the crash, magnetic reconnection continues and the island grows rapidly. Eventually, the former plasma center vanishes completely and the magnetic island becomes the new plasma center. The radius within which magnetic reconnection takes place is called mixing radius, and it is indicated in blue. Inside this radius, particles are redistributed and mixed. This is in particular true for thermal ions, which are closely bound to the magnetic field lines. Fast ions have larger orbit widths due to larger drift velocities, and are thus less closely bound to the magnetic field. This may allow some fast ions to escape from the sawtooth redistribution. In the following sections, we will investigate the sawtooth redistribution of fast-ions experimentally, and discuss theoretical interpretations.

5.2.2 Experimental observations

We have analyzed discharge #31557. The discharge was run with a magnetic field of -2.6 T and a plasma current of 1 MA. Fig. 5.9 shows time traces of the central and mid-radius

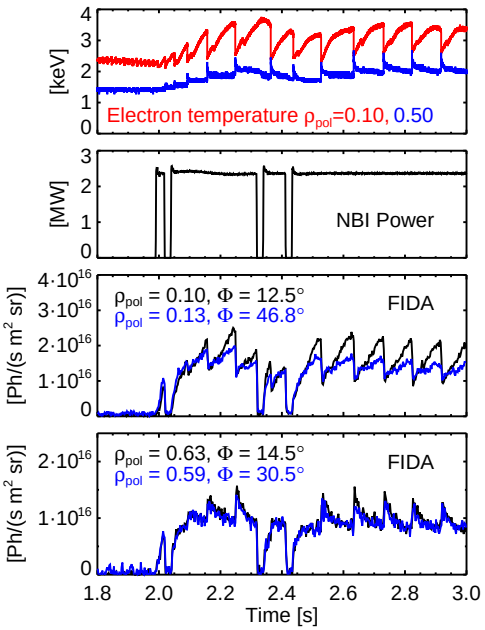

Figure 5.9: Representative timetraces of ASDEX Upgrade discharge #31557. The FIDA raw signals are obtained by integrating the spectra over Doppler-shifts $\Delta\lambda = [3.7, 5.0]$ nm

electron temperature, where strong sawtooth activity can be identified. The mid-radius time trace shows an temperature increase with each sawtooth crash, and hence lies outside of the inversion radius. The time trace of the NBI (Q3) and the FIDA raw signals for central and mid-radius LOS are shown below. The onset of NBI is followed by a rise of the FIDA radiation, which can be identified with the fast-ion density build-up. Later on, the FIDA radiation drops in the plasma center with each sawtooth crash, and rises in the outer lines of sight. This indicates a strong redistribution of the fast ions due to the crash. From the raw signals, it is already observable that the central $\Phi \approx 10°$ LOS, which sees mostly co-current fast ions, measures the strongest sawtooth drop, while the FIDA views, which observe more strongly gyrating fast ions have smaller sawtooth drops. Outside of the inversion, the $\Phi \approx 10°$ projection shows a stronger rise of FIDA radiation than a $\Phi \approx 30°$ projection.

This can be seen more clearly in figure 5.10, where the relative change ((after-before) / before) of the FIDA emission during the sawtooth crash at 2.25s is shown for five FIDA views and for the two radial positions as a function of the mean observed pitch. These observations give the indication, that fast ions with high pitches $v_\parallel/v$ are more strongly expelled from the plasma center than fast ions with low pitches. This can be studied more quantitatively with the FIDA tomography method, described in section 4.3.

We have performed tomographic reconstructions before and after the sawtooth at 2.25s from five FIDA views, which measure all approximately at the same radial position. The calculation was carried out for a set of LOS in the plasma center ($\rho_{\mathrm{pol}} \approx 0.10$) and a second set of five views outside of the sawtooth inversion ($\rho_{\mathrm{pol}} \approx 0.60$). The input spectra for the tomography in the plasma center are shown in fig. 5.11. It can be seen directly that the FIDA contribution in the spectra is significantly lower after the crash - most strongly for the most tangential view ($\Phi = 12.5°$). As in the previous section, regions with impurity lines and beam emission are excluded for the tomography, as well as the

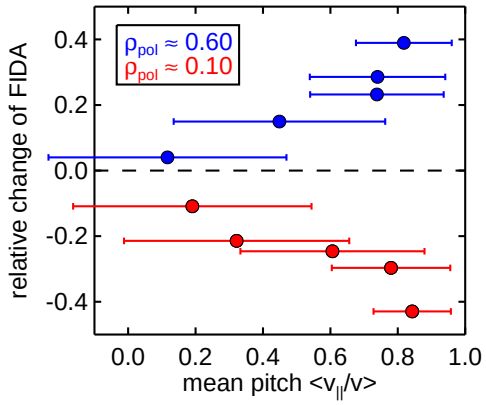

Figure 5.10: Relative change ((after-before) / before) of the FIDA emission ($|\Delta\lambda| = [3.5, 4.5]$ nm) during the sawtooth crash at 2.25s. The x-axis refers to the average pitch, which is observed by the line of sight. It is calculated by integrating the weight functions over the relevant energies (20-60 keV) and wavelength range: $g(\xi) = \int_{\lambda_1}^{\lambda_2} \int_{E_1}^{E_2} W(\lambda, E, \xi) \mathrm{d}\lambda \mathrm{d}E$. The mean value of $g(\xi)$ is plotted as dot, and the standard deviation is shown with error bars. It can be seen clearly that the more tangential FIDA views have a better pitch-resolution than the perpendicular views, which can also be seen in the contour plots of the weight functions (see fig. 4.11).

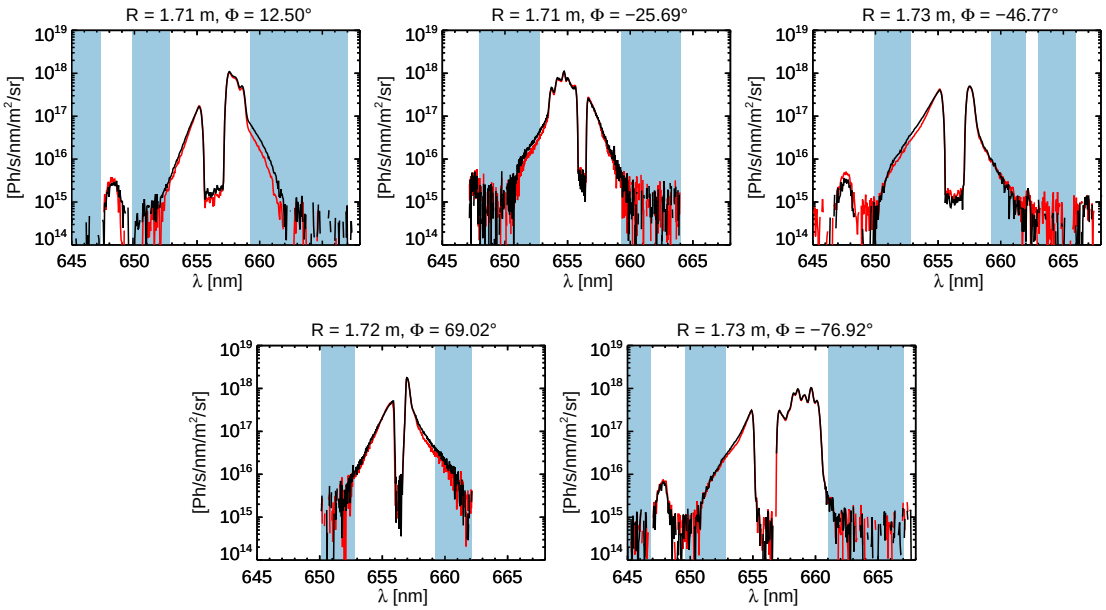

Figure 5.11: FIDA spectra of five views before (black) and after (red) the sawtooth crash. The tomography is calculated from the blue-shaded regions.

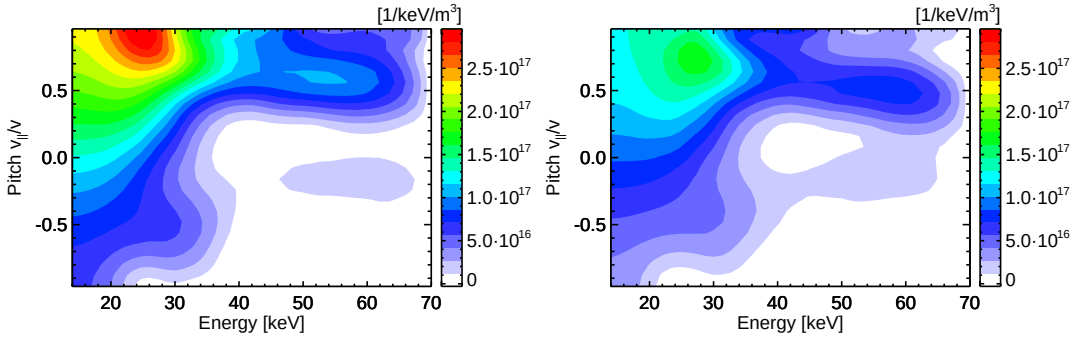

(a) Plasma center $\rho_{\mathrm{pol}} \approx 0.10$

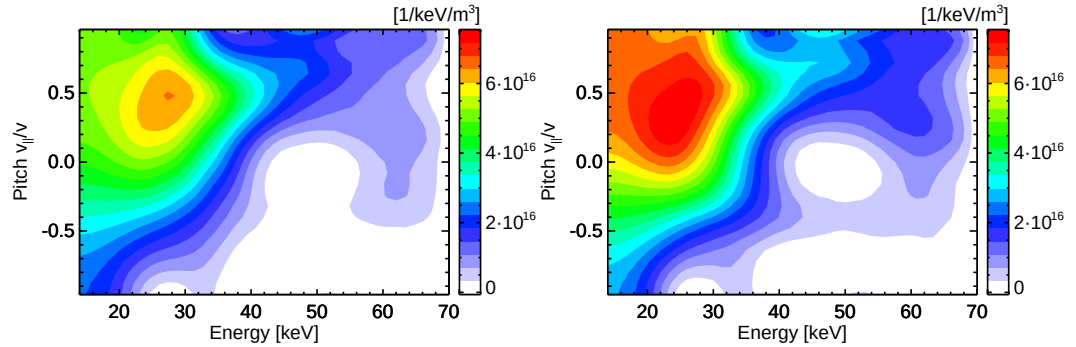

(b) $\rho_{\mathrm{pol}} \approx 0.60$

Figure 5.12: Tomographic reconstruction of $F(E, v_{\parallel}/v)$ from FIDA measurements before (left) and after a sawtooth crash

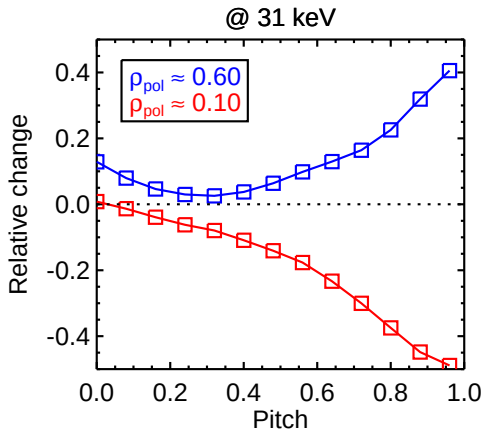

Figure 5.13: Pitch distribution of the relative change of $F(E = 31\ \mathrm{keV}, v_{\parallel}/v)$.

wavelength range [-3.1 nm, +3.1nm] around the D-alpha line, which is dominated by thermal ions.

The results of the tomography are shown in fig. 5.12. From the reconstruction, it is possible to determine the total fast-ion density (of fast ions above 24 keV), and thus quantify the effect of the sawtooth: In the plasma center, it causes a 25% drop of total fast-ion density, while at $\rho_{\mathrm{pol}} = 0.60$ an increase of 19% is observed. With a cut of the fast-ion distribution function at constant energy, we can estimate how this total density

changes are distributed along different pitches (fig. 5.13). It can be seen that fast ions with high pitches are much stronger expelled from the plasma core (-50%), while more strongly gyrating fast ions with pitches close to 0 are much less affected by the sawtooth. This is in accordance with [70], where a FIDA tomography is calculated with singular value decomposition from four FIDA views in the plasma center, and a similar pitch distribution of the density change is found.

Outside of the sawtooth inversion at $\rho_{\mathrm{pol}} = 0.60$, a strong increase is found for fast ions with high pitches (+40%), while at the same time, only little changes are observed for strongly gyrating fast ions with pitches close to 0.

These findings of the tomography are in line with the basic trend, which is already visible in the raw data (as shown in fig. 5.10). However, the tomography allows a more detailed and quantitative study. For example, the influence of the changed beam attenuation due to the strongly changed kinetic profiles is taken into account, because these effects are included in the calculation of the weight functions and separate weight functions are calculated for both time points.

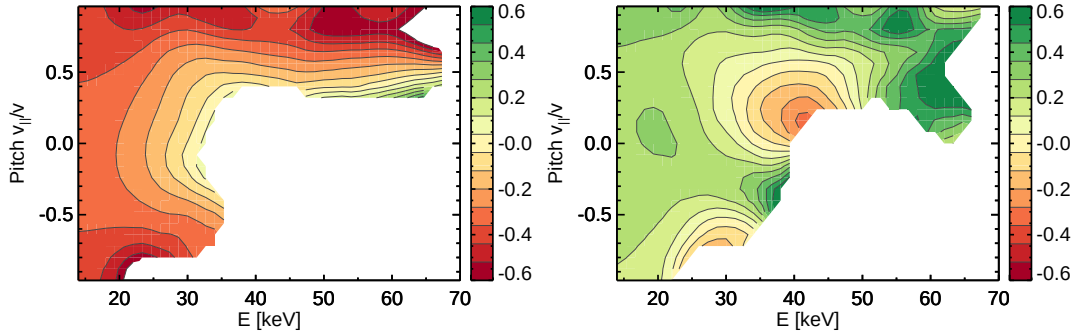

(a) $\rho_{\mathrm{pol}} = 0.10$ **(b)** $\rho_{\mathrm{pol}} = 0.60$

Figure 5.14: Relative change $(F_{\mathrm{after}} - F_{\mathrm{before}})/F_{\mathrm{before}}$ at two different radial positions in and outside of the sawtooth inversion. The relative difference is only well defined, if $F_{\mathrm{before}}(E, \xi)$ is high enough. Therefore, only regions which fulfill $F_{\mathrm{before}}(E, \xi) \geq 0.15 \cdot \max(F_{\mathrm{before}})$ are shown.

We can get a more detailed picture of the redistribution by calculating the relative change for the entire velocity space. This is shown for both radial positions in figure 5.14. The relative difference is only well defined, if $F_{\mathrm{before}}(E, \xi)$ is high enough. Therefore we have calculated it only for regions which fulfill $F_{\mathrm{before}}(E, \xi) \geq 0.15 \cdot \max(F_{\mathrm{before}})$. It can be seen that the absolute value of the relative change is largest for pitches close to +1 for all energies, and weaker for fast ions with pitches around 0. It is hard to make a robust statement for fast ions with very negative pitches, because there are very few fast ions due to to co-current orientation of the neutral beams. At least in the plasma center, it seems that the strength of fast-ion redistribution is more or less symmetrical with respect to $\xi = 0$. For low energies, the pitch dependence of the sawtooth redistribution is rather weak, as it is expected for thermal particles. This pitch dependence seems to increase with energy - and a region around $\xi = 0$ with very weak redistribution is seen towards higher energies. Outside of the inversion radius an overall similar shape of the relative change is found with opposite sign. This can be interpreted such that the ions from the core are redistributed further outside, keeping their energy and magnetic

moment more or less constant. There are some small scale structures visible close to the $F_{\mathrm{before}}(E,\xi) \geq 0.15 \cdot \max(F_{\mathrm{before}})$ boundary, which should be treated with care, since the region close to that boundary has larger uncertainties and the outer measurement position has less fast ions in general. The rather broad region with high redistribution around $E = 60\,\mathrm{keV}, \xi = 0.5$ might be explainable by the fact that the full energy component (60 keV) of the beam is more strongly deposited in the plasma center. Hence, redistribution of those particles towards the mid-radius causes a stronger relative increase there.

5.2.3 Physical interpretation

In the following, we want to discuss briefly a physical interpretation of these findings. Theoretical descriptions of fast-ion sawtooth redistribution can be found in [62–64]. Therein, the evolution of the helical flux Ψ^* is modeled according to the Kadomtsev model [65] with the sawtooth crash duration τ_{cr} as free parameter. The fast temporal change $\dot{\Psi}^*$ of the helical flux during the crash (comp. fig. 5.8) induces an electrical field $\vec{E}$. This results in a radial $\vec{E} \times \vec{B}$-drift (with respect to the minor radius, i.e. from the plasma core to the edge or vice versa), which describes the sawtooth redistribution. This radial drift strongly depends on the helical angle η (defined in eq. (5.1)). Particles, which are closely following the field-lines (e.g. thermal particles, or fast ions with high pitches $|\xi|$), will stay at $\eta \approx const$ and will be strongly redistributed.

In [64], it is shown that the radial $\vec{E} \times \vec{B}$-drift cancels out almost completely when averaging over all η positions. This can be interpreted by a phase-mixing between mode and particles, which prevents particle redistribution. The combined curvature and $\nabla\vec{B}$ drift $\vec{v}_{\mathrm{D}}$ allows such a change of η along a particle orbit:

$$\langle \dot{\eta}_{\mathrm{vD}} \rangle \equiv \omega_{\mathrm{vD}} = \left\langle \frac{\partial\theta}{\partial R} v_{\mathrm{D},R} - \frac{v_{\mathrm{D},\varphi}}{R} + \frac{\partial\theta}{\partial z} v_{\mathrm{D},z} \right\rangle \approx \left\langle \frac{\partial\theta}{\partial z} v_{\mathrm{D},z} \right\rangle \tag{5.4}$$

Hereby, the brackets refer to an average over one poloidal turn of the ion orbit. $v_{\mathrm{D},R}$, $v_{\mathrm{D},\varphi}$ and $v_{\mathrm{D},z}$ are the R, φ and z components of $\vec{v}_{\mathrm{D}}$, whereby the first two can be neglected in good approximation compared to the z component. A particle can escape the sawtooth redistribution, if $|\omega_{\mathrm{vD}}|$ is high enough with respect to the angular frequency $\omega_{\mathrm{cr}} = \pi/\tau_{\mathrm{cr}}$ associated with the sawtooth crash duration τ_{cr} (assuming that half a turn is enough to detach particles [64]). The latter can be estimated from core soft-x-ray signals at $\tau_{\mathrm{cr}} \approx 80\,\mu\mathrm{s}$ (see fig. 5.15a). We have calculated the ratio $|\omega_{\mathrm{vD}}|/\omega_{\mathrm{cr}}$ with an orbit following code, using a CLISTE [5] magnetic equilibrium reconstruction, for the tomography measurement position in the plasma center. It is shown in fig. 5.15b as a function of energy and pitch, along with a classification of the orbits.

It can be seen that $|\omega_{\mathrm{vD}}|/\omega_{\mathrm{cr}} \ll 1$ for strongly passing ions with high $|\xi|$, which is in accordance with the strong redistribution measured at high pitches. In contrast, a broad region around $\xi = 0$ can be seen with $|\omega_{\mathrm{vD}}|/\omega_{\mathrm{cr}} > 1$ and hence a weak sawtooth redistribution. This is in qualitative agreement to the tomography results. Furthermore, it can be seen that $|\omega_{\mathrm{vD}}|/\omega_{\mathrm{cr}}$ increases strongly with the energy (logarithmic scale in fig. 5.15b), which can explain why we measure lower relative changes around $\xi \approx 0$ with increasing energy.

The velocity space region with weak sawtooth redistribution is mostly filled with trapped ions for $\xi < 0$ and with passing, but not axis-encircling, ions for $\xi > 0$ (i.e.

stagnation orbits). For passing ions, this simple model predicts a much lower ω_{vD}. This can be understood directly from equation (5.4): While the drift $v_{\mathrm{D},z}$ remains more or less constant during an orbit, and points always downwards, $\frac{\partial\theta}{\partial z}$ (i.e. the field-line slope w.r.t. z) has a different sign on the high field side than on the low field side (LFS). Passing particles spend approximately equal time on both sides, and hence ω_{vD} is low. In contrast, deeply trapped particles spend more time during their orbit on the LFS, and stagnation orbits stay completely on the LFS - leading to much higher ω_{vD}.

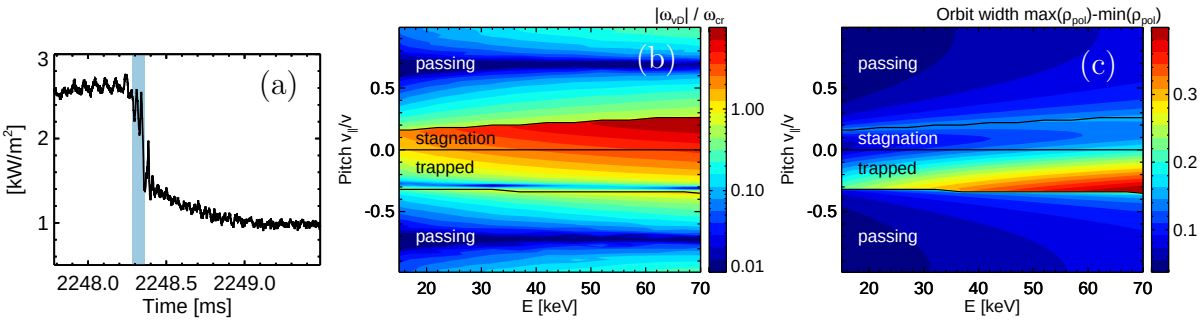

Figure 5.15: (a) Average of two central SXR LOS signals with similar poloidal angle but at different toroidal angle. By the averaging, the signature of the $(1,1)$ mode is reduced and the evolution of the sawtooth itself can be seen more clearly. From the time trace, we can conclude that the sawtooth crash lasts $\tau_{\mathrm{cr}} \approx 80$ µs (blue-shaded area). The latter is in good agreement with the prediction from [71] for collisionless reconnection dynamics. **(b)** Ratio of helical precession $|\omega_{\mathrm{vD}}|$ (calculated for the central position of the tomography) and angular crash frequency ω_{cr}. In the limit of $|q-1| \ll 1$, $|\omega_{\mathrm{vD}}|/\omega_{\mathrm{cr}} \gtrsim 1$ is a criterion that fast ions may escape the reconnection (q being the safety factor). **(c)** Width of the fast-ion orbits in terms of ρ_{pol} ($\max(\rho_{\mathrm{pol}}) - \min(\rho_{\mathrm{pol}})$ along the guiding-center orbit), for the same position as in (b).

Another effect, which can lead to weaker sawtooth redistribution are large orbit widths. However, as fig. 5.15c shows, all orbits with $\xi \in [0;1]$ have comparable widths and hence cannot explain the measured variation of the redistribution in that interval. Only the trapped particles have significantly larger orbit widths, but they are still smaller than the sawtooth mixing radius ($\rho_{\mathrm{pol}} \approx 0.5$). Hence we can conclude that the orbit widths do not play an important role in this particular case.

It has to be noted that these simple considerations can only provide a basic picture of the underlying physics. For example, the influence of the helical $(1,1)$ mode on the particle orbits [72] is neglected here. Nevertheless, a qualitative explanation, why particles with low $|\xi|$ are less affected by the sawtooth can be given, while the exact shape (or the absolute values) of the measured relative change cannot be determined from these basic considerations. For that, more sophisticated modelling is needed (e.g. as described in [62–64]), and the results of the FIDA tomography could allow to verify these models.

5.3 Alfvén eigenmodes

Alfvén eigenmodes (AE) can lead to radial redistribution of particles and in particular, of fast ions. Future fusion reactors will have a large content of fast ions, which provide a potentially strong drive for AEs. For example, the ignition of a fusion reactor is based on plasma heating by fast α-particles, which are created with a birth energy of 3.5 MeV by the D-T fusion reaction. Thus, future burning plasma experiments, such as ITER, may witness strong AE activity, which could result in fast-ion redistributions or losses [73, 74].

In order to keep the plasma ignited, the α-particles must be well confined until they are thermalized. In addition, efficient plasma heating or current drive by NBI and ICRH rely on good fast-ion confinement. Furthermore, fast-ion losses might cause severe damages to the first wall. Thus, fast-ion transport caused by AEs must be investigated and understood.

5.3.1 Basic physics

Shear Alfvén waves are low-frequency (with respect to the ion cyclotron frequency) magneto-hydrodynamic oscillations of the magnetic field lines and the plasma. The inertia is given by the ion mass density and the restoring force is provided by the magnetic field line tension. This leads to a characteristic phase velocity, the so-called *Alfvén velocity*:

$$v_\mathrm{A} = \frac{B}{\sqrt{\mu_0 \sum_i n_i m_i}} \approx \frac{B}{\sqrt{\mu_0 n_\mathrm{e} m_\mathrm{i}/Z_\mathrm{i}}} \tag{5.5}$$

The index i stands for the ion species and the approximation step is exact for a one-species plasma with ion mass m_i or if all ion species have the same charge-to-mass ratio. Shear Alfvén waves are transversal waves that propagate parallel to the magnetic field such that the wave vector $\vec{k}$ is parallel to $\vec{B}$, i.e. $\vec{k} = k_\parallel \hat{e}_\parallel$. The oscillating part of the electric and magnetic field vectors is perpendicular to the static part of the magnetic field (denoted as $\vec{B}$). The angular frequency of shear Alfvén waves is linked to the parallel wave number $k_\parallel$ by the dispersion relation:

$$\omega = |k_\parallel| v_\mathrm{A}. \tag{5.6}$$

Due to the toroidal boundary condition in a tokamak plasma and the poloidal winding of the field lines, the wave number must fulfill a periodicity constraint:

$$k_\parallel = (n - m/q)/\tilde{R} \approx (n - m/q)/R_0. \tag{5.7}$$

Here, m and n are the poloidal and toroidal integer mode numbers, and q is the safety factor on the given field-line. $2\pi\tilde{R}$ is the toroidal periodicity length which can be approximated using the major radius of the magnetic axis R_0. Waves that satisfy this dispersion relation (5.6) are part of the Alfvén *continuum*. Both q and v_A typically vary with the minor radius r. This means, that a shear Alfvén wave with given frequency ω, which fulfills the dispersion relation (5.6&5.7), can only exist on a narrow flux surface. On neighboring flux surfaces, the frequency would already be different. The amplitude profile of such a wave would hence be a very narrow (δ-like) function. This results in a strong damping of

such waves (the damping rate is proportional to $\mathrm{d}/\mathrm{d}r(k_\parallel v_\mathrm{A})$), which is called *continuum damping*.

The wave damping is in concurrence with wave driving mechanisms. For example, energetic particles can deliver energy to the wave. If the wave drive is larger than the damping, an Alfvén wave becomes a plasma instability and is then usually called Alfvén eigenmode (AE). In general, the continuum damping is too strong and cannot be overcome by the fast-ion drive. However, several mechanisms exist that weaken the continuum damping if certain conditions are fulfilled (for example, band gaps can arise in the continuum). The different mechanisms result in a zoo of possible Alfvén eigenmodes. An overview of the different types is given e.g. in [75].

The first type we will discuss is the so-called *reverse shear Alfvén eigenmode* (RSAE). As the name suggests, it can occur in a region of the plasma, where the magnetic shear reverses, i.e. where the q-profile has an extremum. Assuming that the n_e profile is flat (which is a quite good approximation for most tokamak plasmas), the q-extremum leads to $\partial\omega/\partial r = 0$ and a strongly reduced continuum damping around the extremum.

In conventional tokamak scenarious, the q-profile is monotonically decreasing from the edge towards the plasma core. Advanced tokamak scenarios feature non-monotonic q-profiles with a minimum q_min away from the magnetic axis. Consequently, the continuum damping is strongly reduced in the region of low magnetic shear around q_min. Provided sufficient drive (e.g. by fast ions), the Alfvén waves can become unstable and rise in amplitude to form a reverse shear Alfvén eigenmode. The amplitude profile is given by a peaked function centered around the q-profile minimum.

Another mechanism which lowers the continuum damping is the formation of frequency gaps in the continuum. This is a similar effect as the band gaps known from solid state physics. In general, any periodic modulation of the refractive index N gives rise to a band gap [75, 76]. For Alfvén waves in a tokamak, such a modulation is given by the magnetic field strength variation on a field line, which is caused by the toroidal geometry and the resulting $1/R$ decay of the toroidal magnetic field. This causes a periodic change of the phase velocity v_A along a given field line and thus a toroidicity-induced frequency gap.

This is illustrated in fig. 5.16a, where the dispersion relation for Alfvén waves with toroidal mode number $n = 4$ and poloidal mode numbers $m = 4 - 8$ are shown, as they would calculate from eq. (5.6&5.7). This corresponds to a cylindrical tokamak (i.e. aspect ratio $\epsilon = 0$) and it can be seen, that the curves between two neighboring m-numbers cross each other. If toroidicity is included in the corresponding MHD-equations, neighboring modes (with m and $(m + 1)$) are coupled, such that the poloidal mode number m is no longer a good "quantum" number. The crossing of the dispersion relation is removed, and the dispersion relation splits into two branches (at the former crossing), such that a frequency gap forms (fig. 5.16b).

Physically, the formation of the gap can be explained by destructive interference between counter-propagating waves (with m and $m + 1$). The frequency, where the gap occurs can be calculated by the Bragg frequency

$$\omega = v_\mathrm{A}/(2qR_0), \tag{5.8}$$

which is shown in fig. 5.16 with the dashed line.

In the frequency gap, no continuum damping occurs, such that Alfvén eigenmodes can be excited easily. The gaps which we have discussed here are induced by toroidicity, such

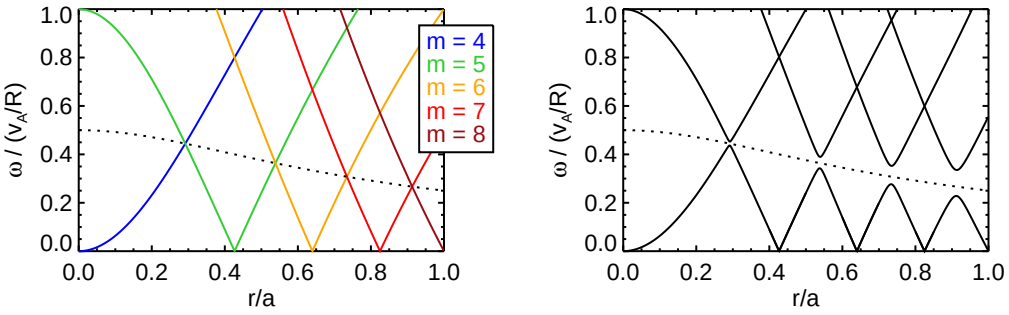

(a) Cylinder $\epsilon = 0$ **(b)** Torus $\epsilon = a/R_0 = 0.5/1.7$

Figure 5.16: Alfvén wave dispersion relation for several waves with toroidal mode number $n = 4$. (a) Cylindrical tokamak, calculated by eq. (5.6&5.7). (b) Including toroidicity (i.e. finite aspect ratio ϵ), calculated with eq. (10) in [77]. The angular Bragg frequency $\omega = v_A/(2qR)$ is shown with a dashed line. The used q-profile is monotonically increasing from 1 to 2. The x-axis is given by the normalized minor radius.

that the resulting Alfvén eigenmodes are called toroidicity-induced Alfvén eigenmodes (TAEs).

As motivated before, any periodic modulation of $v_A \propto B$ results in the formation of frequency gaps which gives rise to AEs, and TAEs are just one example. E.g., other periodic modulations are caused by ellipticity or non-circularity. They give rise to frequency gaps at the crossings between m and $(m + 2)$, or m and $(m + 3)$, respectively. The resulting AEs are abbreviated as EAEs and NAEs. In stellerators, helicity-induced Alfvén eigenmodes (HAEs) have been observed [78].

5.3.2 Experimental recipe

In AUG, Alfvén eigenmodes can be driven unstable by NBI or ICRH. We analyze discharge #30370, where 2.5 MW of 60 keV NBI (Q3) is applied early (from 0.20s on) in the current ramp-up. The corresponding injection velocity is sub-Alfvénic, i.e. smaller than v_A. Representative time traces of the discharge are shown in fig. 5.17. The plasma density remains at relatively low values of $\approx (1.5) \cdot 10^{19}$ m^{-3} such that the fast-ion pressure is a significant contribution to the total plasma pressure. The plasma is initially in limiter configuration, and switches to divertor configuration at ≈0.37 s.

During the early current-ramp up, the q-profile can be reversed, because the plasma current has not yet diffused from the plasma edge into the plasma center. Eventually, the current diffusion will lead to a monotonic q-profile. However, the corresponding time scale is typically in the order of one second, such that the reversed q-profile is sustained during the current ramp-up. This can be enhanced e.g. with counter-current drive, or with early heating (i.e. during the current ramp-up), because high electron temperatures slow down the current diffusion [79]. Here, we use early NBI heating from 0.20s on.

5.3.3 Experimental observations

Figure 5.19 shows fluctuation spectrograms of (a) reflectometry, (b) the fast-ion loss detector (FILD) and (c) electron cyclotron emission (ECE). RSAEs are seen in all three measurements, which proofs that the q-profile is reversed. The RSAEs are recognized

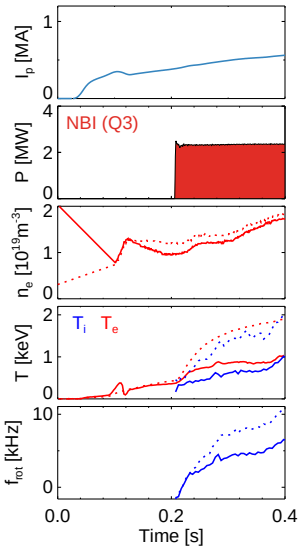

Figure 5.17: Representative timetraces of discharge #30370. Core values are shown with dashed line, while the full lines correspond to mid-radius positions ($R \approx 1.9$ m).

by their characteristic frequency chirping, i.e. they change their frequency rapidly. This is due to the temporal evolution of the q-profile, in particular of its minimum $q_{\min}$. As explained in the physic basics (5.3.1), the RSAEs are localized at the radial position of $q_{\min}$. Hence, their frequency is given by:

$$\omega \approx (n - m/q_{\min}) \cdot v_{\mathrm{A}}/R_0. \tag{5.9}$$

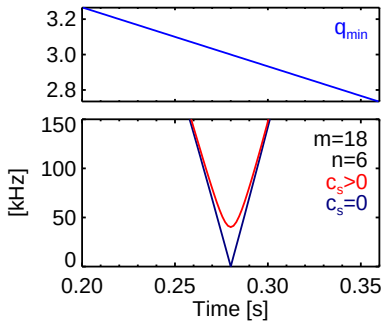

Figure 5.18: Frequency chirping of a RSAE with $m = 18$, $n = 6$ due to varying $q_{\min}$.

$q_{\min}$ decreases with time, as the current is ramped up, and this leads to the rapid change of the RSAE frequency. This is illustrated in fig. 5.18 for $m = 18, n = 6$. It can be seen, that the above formula (5.9) would predict the frequency dropping to zero when $q_{\min} = m/n = 3$, which is not observed in the experiment. To explain this, effects of plasma pressure must be included. In the low-frequency region, this results in a corrected dispersion relation of the form [80]:

$$\omega = \sqrt{\left(n - \frac{m}{q_{\min}}\right)^2 + 2\frac{c_{\mathrm{s}}^2}{v_{\mathrm{A}}^2}} \cdot \frac{v_A}{R_0}, \text{ with the ion sound speed } c_{\mathrm{s}}^2 = \frac{T_e + \frac{7}{4}T_i}{m_{\mathrm{i}}}. \tag{5.10}$$

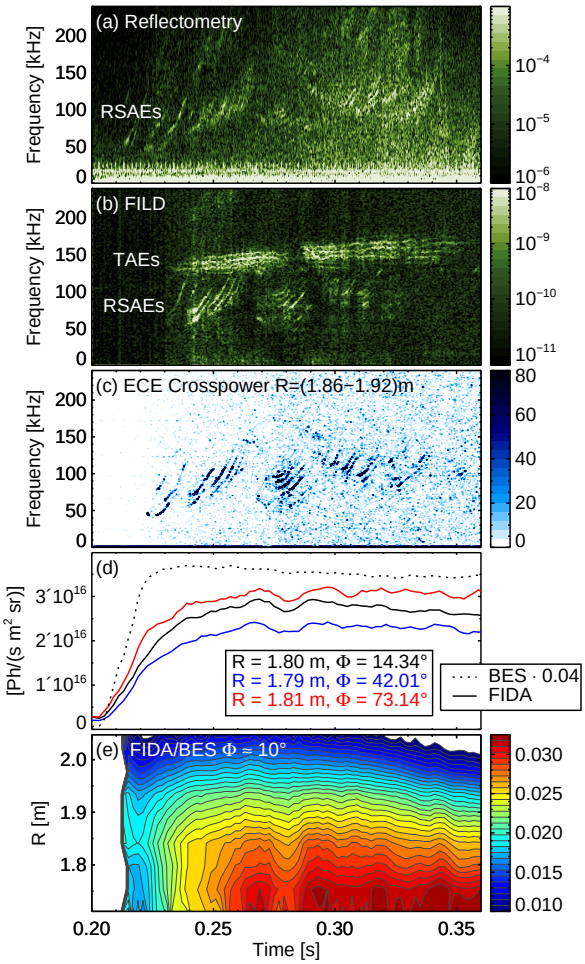

Figure 5.19: Fluctuation spectrograms of (a) reflectometry, (b) fast-ion loss detector (FILD) and (c) electron cyclotron emission (ECE). (d) FIDA and BES raw data. (e) FIDA/BES for all lines of sight of the $\Phi \approx 10°$ viewing array.

This lifts the frequency minimum up to $\sqrt{2}c_s/R_0$ as shown in fig. 5.18 by the red curve. Furthermore, it explains the parabola-like bending of the measured RSAE frequency curves towards lower frequencies. The measured frequencies are additionally shifted by the toroidal plasma rotation, multiplied with the toroidal mode number n.

In contrast to the RSAEs, TAEs do not show such a rapid frequency chirping. As explained before, they are localized in the frequency gaps which exist at the position, where the dispersion relation of m and $(m+1)$ waves (with same n) would cross in cylinder geometry. The crossing position can be calculated by setting $\omega(m,n) = \omega(m+1,n)$ using (5.6&5.7). The solution of this equation delivers: $q = (m+1/2)/n)$. I.e., a TAE with given mode numbers m, n is localized close to the flux surface with this q-value. When the q-profile changes, the TAE changes its position to stay at the same q-value. The TAE frequency can be approximated with the Bragg frequency (5.8) and it changes only if v_A changes. In the analyzed discharge, TAEs are seen only in the FILD spectrogram. The other fluctuation measurements may have too little sensitivity to resolve the TAEs or measure at other spatial positions. The TAEs show only a very slow increase in frequency

(compared to the RSAEs), which can be explained by the increasing electron density ($v_A \propto \sqrt{1/n_e}$).

At $t \approx 0.28$ s, a so-called RSAE *cascade* can be seen altogether in fig. 5.19(a-c): Several RSAEs with similar chirping behavior are appearing at the same time. RSAE cascades appear, when q_{min} passes through an integer value, because then, many modes can exist that fulfil $m/n = q_{min}$. In particular, any toroidal mode number n is possible. The modes with different n appear in the measured spectrograms with shifted frequencies (due to the toroidal plasma rotation). From [81] we can infer that q_{min} goes through a value of three at this time point, because the timing of the current-ramp and heating are similar for the given discharge and the discharge analyzed in [81].

In Figure 5.19(d) time traces of FIDA raw signals are shown for three different projection angles at $R \approx 1.80$ m. The fast-ion density build-up can be seen clearly after the beam is switched on at 0.202 s. During the RSAE cascade at 0.28 s, a clear signal drop of about 10% is observed by all three projection angles. After the RSAEs have disappeared in the spectrograms, the FIDA signal recovers back to the pre-cascade level. At the same time, the beam emission (BES, shown with the dashed line for one line of sight) does not change significantly during this time interval. Hence, the FIDA signal drop must be caused by a fast-ion density drop at the respective radial position. Figure 5.19(e) shows a contour plot, of the measured FIDA/BES signal ratio for all radial lines of sight of the $\approx 10°$ viewing array. At 0.28s, a drop of the fast-ion density is measured in all central lines of sight, up to a major radius of ≈ 1.95 m (the magnetic axis is located at 1.66 m, according to CLISTE).

These observations can be interpreted by a redistribution of the central fast-ion density due to the RSAE cascade. Since the RSAEs are seen also in FILD signals, a fraction of the redistributed fast-ions is lost entirely. However, due to the missing absolute calibration of the FILD, this fraction cannot be quantified. It is interesting to note, that the TAEs (measured by FILD) are disappearing synchronized with the drop of the central fast-ion density. They reappear when the FIDA signals recover to their pre-cascade level. This could be interpreted such that the lowered fast-ion density does not provide enough drive to destabilize the TAEs. As the fast-ion density increases after the cascade, they are driven unstable again and reappear in the spectrogram.

5.3.4 Mode characterization

In the following section, we will investigate the RSAE mode numbers and radial structure. Figure 5.20 shows Fourier-analyzed data from the ECE imaging diagnostic at ASDEX Upgrade. Here, two modes are shown: Fig. 5.20a corresponds to the RSAE starting at ≈72 kHz and fig. 5.20b corresponds to the next higher RSAE starting at ≈82 kHz. For both modes, three contour plots are shown: The total amplitude ($\Delta T_e/T_e$), and the amplitude of the sine and cosine component of the Fourier analysis. It can be seen that both modes have an amplitude of roughly $\Delta T_e/T_e \approx 1.5\%$ and are localized at $R \approx 1.89$ m at the mid-plane. For comparison, we have overlayed contours of ρ_{pol} and the straight field line angle θ^*.

From the sine and cosine Fourier components, the poloidal structure of the modes is seen directly. The poloidal mode number m can be estimated by e.g. counting the difference in θ^* between two neigbboring peaks with same sign. If this difference is denoted with $\Delta\theta^*$, m calculates then simply as $m = \Delta\theta^*/360°$. At the beginning of the RSAE

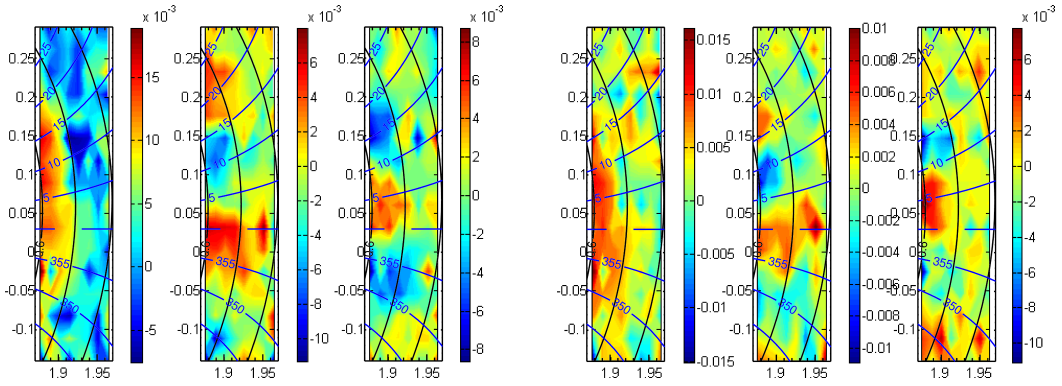

(a) ≈72 kHz **(b)** ≈82 kHz

Figure 5.20: Fourier analysis of ECE imaging data (colors), carried out for two RSAE modes. Overlaid are contours of ρ_{pol} and the straight field line angle θ^*. The x and y-axis are given by $R\,[\mathrm{m}]$ and $z\,[\mathrm{m}]$, respectively, and the colorbars show $\Delta T_e/T_e$.

cascade, $q_{\mathrm{min}} = m/n$ is 3, which implies that m must be a multiple of three. Taking this into account, we find $\Delta\theta^* = 24°, m = 15, n = 5$ for fig. 5.20a and $\Delta\theta^* = 20°, m = 18, n = 6$ for fig. 5.20b. As an overview, we have written the toroidal mode number n in fig. 5.21 next to the corresponding mode. It is within expectations, that modes with higher n appear at higher frequencies due to toroidal plasma rotation. Consequently, it can be concluded, that the modes with higher frequencies have $n = 7$ and 8 as indicated in the plot.

The mode amplitude and radial position can be also determined by the 1D ECE system. Fig. 5.19(c) shows a cross-power spectrogram of four neighboring ECE channels in the range of $R = 1.86 - 1.92$ m (at $z = 0.07$ m). Hence, all modes which are visible in that contour plot lie in this spatial region. This can be further analyzed by considering the spectrograms of the individual ECE channels, which are shown in fig. 5.21.

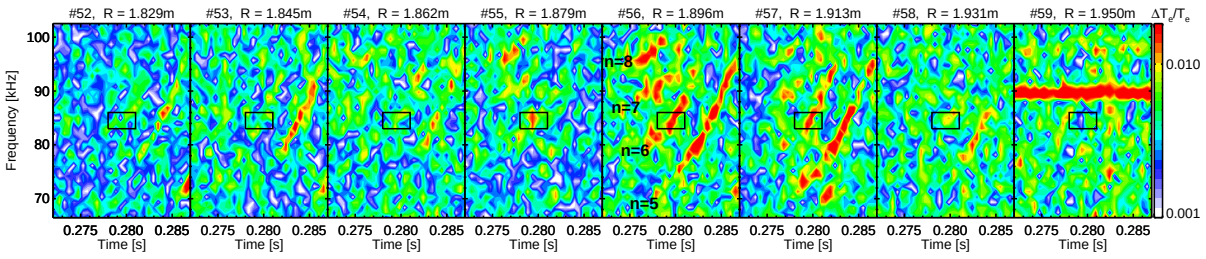

Figure 5.21: Spectrograms of neighboring individual ECE channels.

The RSAEs are most clearly visible in the channels #56-57. By integrating over an appropriate frequency-time window for each mode, we can determine radial profiles. In fig. 5.21, the chosen region for the $n = 6$ mode is shown as an example. The calculated radial profiles of the modes with $n = 5 - 8$ are shown in fig. 5.22. All four modes have a very similar radial extension. The amplitude peak is located at $R = 1.895$ m, which is in good agreement with the ECE imaging data. It can be concluded, that the minimum of the q-profile must lie at the same radial position.

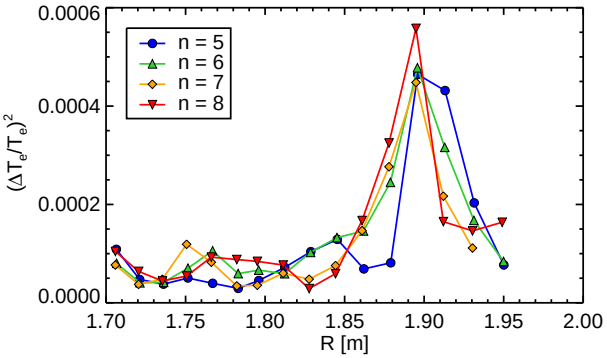

Figure 5.22: Radial profile of the RSAEs at 0.28 s.

5.3.5 FIDA tomography

To further quantify the fast-ion density drop due to the RSAE cascade, we have computed FIDA tomographies before the RSAE (at 0.268s-0.276s) and during the RSAE cascade (at 0.276s-0.284s), where the FIDA signal drop is visible in the raw data. In this discharge, three FIDA viewing directions are available. We have analyzed the data from the three lines of sight shown in fig. 5.19d, which are all located at $R \approx 1.80$ m.

Figure 5.23 shows the reconstructed fast-ion velocity distribution for the two time points. For both time points, the maximum of the velocity distribution is located at approximately 60 keV and pitch $\xi = 0.7$, which is in agreement with the NBI injection energy and geometry. The velocity distribution increases towards the half and third injection energy component (30 and 20 keV), but the tomography is not able to separate the peaks, which is in line with previous considerations (e.g. in section 5.1). In general, the shape of the reconstructed distribution is in agreement with basic expectations of a NBI slowing down distribution (comp. section 2.2.3).

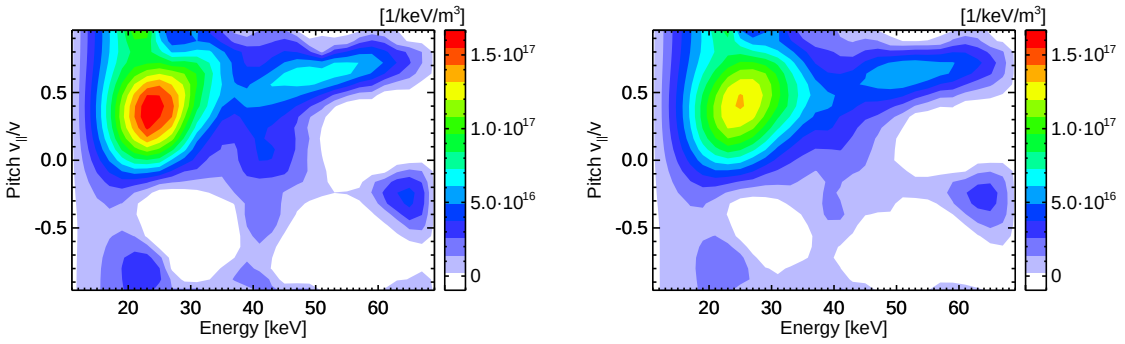

(a) Before the RSAE cascade (0.268s-0.276s) **(b)** During the RSAE cascade (0.276s-0.284s)

Figure 5.23: FIDA tomography from three lines of sights located at $R \approx 1.80$ m.

The absolute values however decrease clearly during the RSAE cascade, which is in line with the basic trend visible in the raw data. With the tomography, the fast-ion density drop can be quantified. In particular, the total integral over the reconstruction and hence the fast-ion density decreases by 10% ($3.09 \cdot 10^{18}$ m^{-3} vs. $2.77 \cdot 10^{18}$ m^{-3}). Here, the shape of the distribution function does not change strongly. Instead, the absolute values go down rather uniformly. Particular regions with increased or decreased fast-ion redistribution

are not clearly seen. It should be noted however, that changes with a very small structure in the velocity space can possibly not be resolved by the FIDA tomography, due to its limitations in energy and pitch-resolution.

5.4 Acceleration of deuterium beam ions by 2nd harmonic ICRH

5.4.1 Introduction

The coupling of radio frequency (RF) waves to ions is an important physics aspect for future fusion devices. In ITER, 2^{nd} harmonic ion cyclotron resonance heating of tritium is one of the foreseen ICRF schemes, along with He-3 minority heating [82]. The 2^{nd} harmonic heating has the benefit that it can accelerate the main ion species directly. However, it is only efficient for ions with large Larmor radii with respect to the RF wave length (as discussed in chapter 2). In addition, He-3 is very expensive, such that its usage must be reduced to an absolute minimum (e.g. for the plasma start-up phase, when the ions are cold and Larmor radii are small). Thus, it is important to understand the physics of 2nd harmonic heating for the success of future fusion devices such as ITER.

At ASDEX Upgrade, the Larmor radii of D beam ions (i.e. from 60 keV NBI) are large enough for effective 2^{nd} harmonic absorption. Hence, 2^{nd} harmonic absorption can be studied by experimental investigation of the further acceleration of those beam ions. This has already been demonstrated at many tokamaks [83, 84, and references therein]. Many measurements of the ICRH acceleration have been carried out using neutral particle analyzers [85] or measurement of the neutron rates created by D-D fusion. In addition, neutron spectroscopy has become a valuable tool [86], because the neutron energy spectrum yields information about the velocity distribution of the initial fusion reactants (i.e. the deuterium ions). Fast ions that are so strongly accelerated by ICRH, such that their orbits are no longer confined, can be measured with fast-ion loss detectors [87]. In addition, gamma-ray measurements [88, 89] and collective Thomson scattering [90] have been used to detect ion acceleration by ICRH.

With the FIDA diagnostic, first observation of beam-ion acceleration by ICRH harmonics has been reported in [84]. The FIDA diagnostic has the advantage that it can provide both a very well spatially localized measurement and a decent energy resolution. The recent upgrades to the FIDA diagnostic at ASDEX Upgrade towards five viewing directions allow even a tomographic reconstruction of the 2D velocity space distribution at well-defined spatial measurement positions. In section 5.1, we have demonstrated that FIDA tomography is well able to distinguish between 60 and 93 keV NBI. Hence, the diagnostic capabilities allow to measure ICRH-induced acceleration of 60 keV NBI above the injection energy. In the following section, we present the first observations of 2nd harmonic beam ion acceleration with FIDA tomography. These results are then compared to theoretical predictions by TORIC-SSFPQL and TORIC/TRANSP.

5.4.2 Preliminary considerations

At the 2nd harmonic ICRH resonance, hydrogen is also resonant at the fundamental cyclotron frequency. The hydrogen concentration cannot be controlled directly. At ASDEX Upgrade, a typical hydrogen concentration of 5% is present in the machine, which is measured by mass-separated neutral particle analyzers [45]. This gives rise to hydrogen

minority ICRH heating, which is in competition with 2nd harmonic absorption by D beam ions.

In terms of the FIDA diagnostic, the resulting fast hydrogen distribution F_{H} has to be considered, because the H_α emission ($\lambda_{0,\mathrm{H}} = 656.28$ nm) lies very close to the D_α line $\lambda_{0,\mathrm{D}} = 656.10$ nm. Thus, the FIDA technique cannot distinguish between fast deuterium and fast hydrogen ions, but will measure a sum of both contributions. In the presence of ICRH, the hydrogen distribution can be assumed to be entirely non-Maxwellian and hydrogen should be considered entirely as fast-ion species. This must be compared then to the fast D ion density, which has typical concentrations of 10%. Thus, we will further investigate the contribution of fast H to the FIDA signal.

To further quantify this, we have computed weight functions $W_{\mathrm{H,D}}$ both for hydrogen and deuterium with the FIDASIM code, which are defined such that the FIDA signal is given by:

$$FIDA(\lambda) = \iint W_{\mathrm{H}}(\lambda, E, \xi) F_{\mathrm{H}}(E, \xi) \mathrm{d}E \mathrm{d}\xi + \iint W_{\mathrm{D}}(\lambda, E, \xi) F_{\mathrm{D}}(E, \xi) \mathrm{d}E \mathrm{d}\xi \quad (5.11)$$

To calculate them, the FIDASIM code had to be slightly adapted, because it was used only for deuterium before. These adaptations were however straight forward: In particular, the cross-sections in the collisional radiative model are valid for all hydrogen isotopes, such that only the difference in the ion mass has to be considered. The calculation results for a Dopplershift of 4.95 nm are shown in figure 5.24. It can be seen that the weight functions for H and D lie exactly on top of each other (both in shape and absolute values), when plotted as a function of pitch ξ and $E/m = v^2/2$. This can be understood easily: The

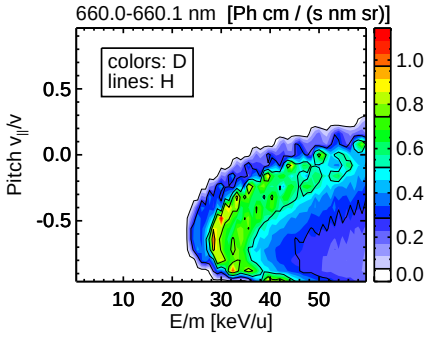

Figure 5.24: Comparison between weight functions for hydrogen and deuterium.

Doppler-shift is proportional to the velocity v. In addition, all cross-sections considered by FIDASIM depend on the relative velocities between the reactants (charge exchange, ion-impact ionization/excitation and electron-impact ionization/excitation).

So, the weight functions for H and D are equal with respect to equal Doppler-shift $W_{\mathrm{H}}(\lambda - \lambda_{0,\mathrm{H}}) = W_{\mathrm{D}}(\lambda - \lambda_{0,\mathrm{D}})$. If the small difference between the H_α and D_α wavelength is neglected ($\lambda_{0,\mathrm{H}} \approx \lambda_{0,\mathrm{D}}$), the FIDA signal can be directly interpreted as a sum of the H and D fast-ion distribution function:

$$FIDA(\lambda) \approx \iint W_{\mathrm{D}}(\lambda, \tfrac{E}{m}, \xi) \cdot \left(F_{\mathrm{H}}(\tfrac{E}{m}, \xi) + F_{\mathrm{D}}(\tfrac{E}{m}, \xi) \right) \mathrm{d}\tfrac{E}{m} \mathrm{d}\xi \quad (5.12)$$

This assumption allows to calculate meaningful FIDA tomographies in the presence of both fast H and fast D. Hereby, it is important to calculate the tomography in terms

of E/m, which can then be interpreted as sum of H and D. Within this work, we will assume $\lambda_0 = \lambda_{0,\mathrm{D}}$. This means that the D contribution to the FIDA signal will be analyzed exactly, while the H contribution will enter into the tomography with an offset of 0.18 nm. Compared to the spectral resolution of the spectrometer (0.21 nm) and compared to the absolute value of analyzed Doppler-shifts ($\approx$ 3 nm - 7 nm) this seems to be acceptable. Furthermore, the H distribution is expected to have a rather smooth, almost Bi-maxwellian shape, for which such an offset is less important than for the D beam ion distribution.

5.4.3 FIDA tomography in the plasma center

We have analyzed discharge #30809, which features a toroidal field of $B_\mathrm{t} = -2.4$ T and plasma current of $I_\mathrm{p} = 1.0$ MA. The ICRH frequency is 36.5 MHz and the resonance layer is located at $R \approx 1.69$ m (neglecting Doppler shifts), i.e. very close to the magnetic axis. Representative time traces of the discharge are shown in fig. 5.25. The rather low electron density ($n_\mathrm{e} \approx 2.5 \cdot 10^{19}$ m^{-3}) leads to low bremsstrahlung, which is very beneficial for the FIDA signal-to-background ratio. The plasma shows strong sawtooth oscillations with rather long periods in the range of 120 ms. In order to have nearly steady-state conditions, we chose time points just before a sawtooth crash. We have compared $t = 4.60$ s with 2.4 MW NBI + 2.0 MW ICRH and $t = 4.48$ s with 2.4 MW NBI only (the time-points are indicated with dashed lines in fig. 5.25).

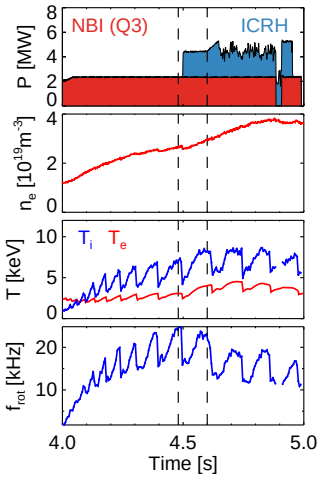

Figure 5.25: Representative timetraces for discharge #30809. The analyzed time points are marked with dashed lines.

FIDA data from four viewing arrays are available for this discharge. Figure 5.26 gives an overview of the approximate FIDA measurement positions used for this analysis. The measurement position is determined by the overlap between the lines of sight and the neutrals from the neutral beam Q3 (calculated by FIDASIM). The local angle Φ between the magnetic field and the lines of sight is indicated by the color coding. In order to calculate a FIDA tomography, the measurements with different angle Φ at similar position are grouped together, as it is indicated by the boxes. In this section, we will discuss in detail the results of the FIDA tomography at the innermost box, and in the next section we will discuss the profiles calculated from all measurement positions.

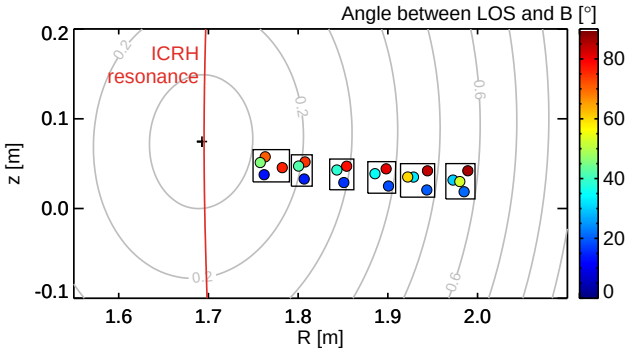

Figure 5.26: FIDA measurement points in the poloidal cross-section. With grey lines, contours of ρ_{tor} are show (at 4.60s).

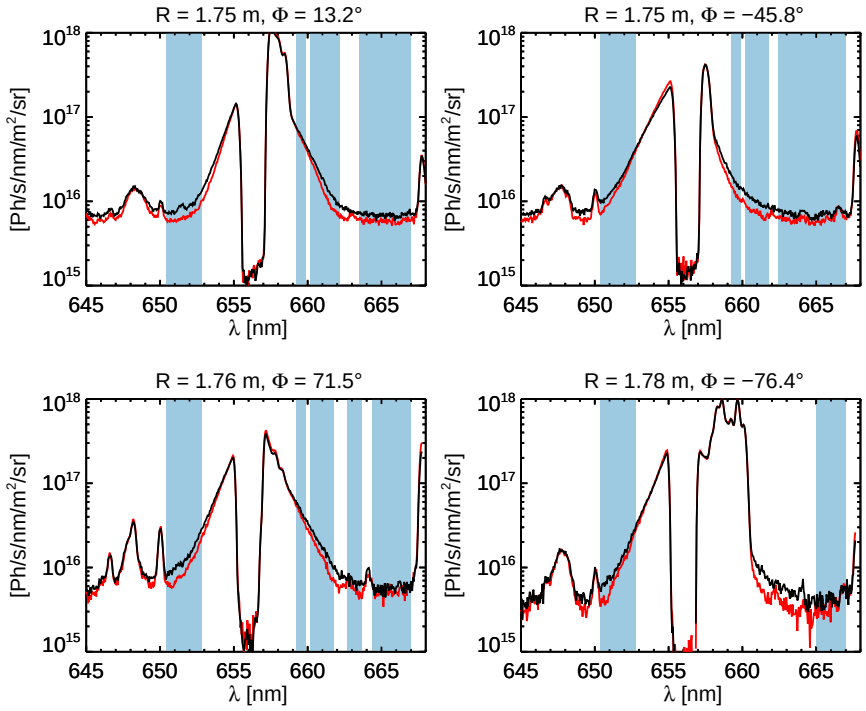

Figure 5.27: FIDA spectra of the four center-most lines of sight at $t = 4.48$s (NBI only, red line) and $t = 4.6$s (NBI+ICRH, black line). The tomography is calculated from the blue-shaded regions.

The spectra which are used for the inner-most tomography position are shown in fig. 5.27. Fast ions with the NBI injection energy (60 keV) can have a maximum Doppler-shift of 5.2 nm, which corresponds to 661.3 nm on the right and 650.9 nm on the left side of the D-alpha line. In the NBI-only phase, FIDA light is measured only within these boundaries. In the NBI+ICRH phase, tails above these boundaries are visible, which indicates that fast ions above the injection energy are present and that the FIDA diagnostic is sensitive enough to measure them.

The tomographic reconstruction of the velocity space is calculated from the blue-shaded areas. The background due to bremsstrahlung is assumed to be a flat line. It is evaluated at 665-667 nm and subtracted from the spectra. The result of the tomography is shown in

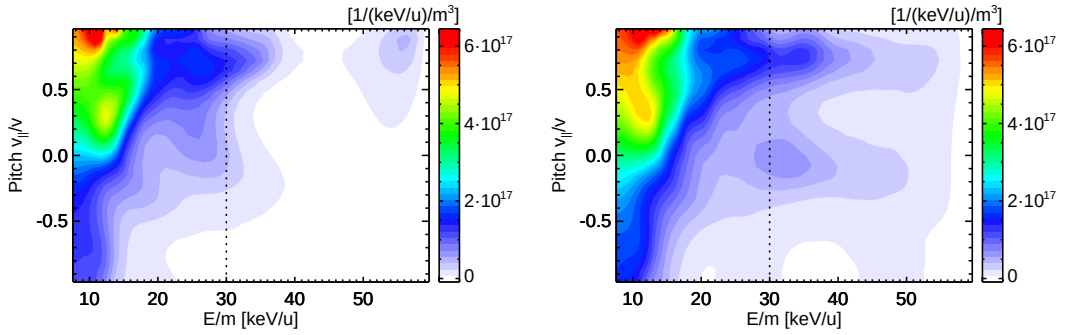

(a) 4.48s (NBI only) **(b)** 4.60s (NBI+ICRH)

Figure 5.28: FIDA tomography at $\rho_{\mathrm{tor}} = 0.12$ (on the low field side).

fig. 5.28. Here, the NBI full injection energy (30 keV/u) is marked with a dashed line. In the NBI phase ($t = 4.48$ s), the tomography yields mainly fast ions with energies below the injection energy, as expected. In the presence of ICRH (4.60 s), two high energy tails are clearly seen. The stronger tail appears at pitches ≈ 0.7, and can be identified as beam ions, which are further accelerated.

A second, weaker high energy tail is seen at pitches -0.3 to 0.0. Particles within this region are on trapped orbits, as shown in the orbit classification plot fig. 5.29. This is

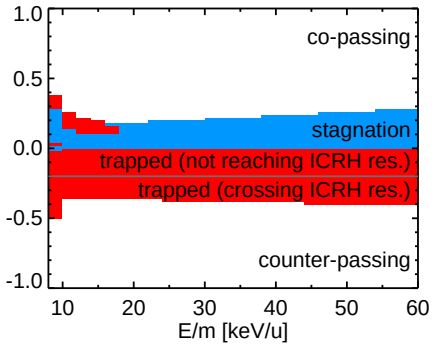

Figure 5.29: Classification of the fast-ion orbits which pass through the measurement position ($\rho_{\mathrm{tor}} = 0.12$ on the low field side).

in agreement with the well-known effect of "resonance localization" ([35, 36] and section 2.4.3): Trapped ions, which have their banana tips close to the ICRH resonance layer, are most effectively accelerated, because the parallel velocity is low close to the tips. Thus, such ions spend a longer fraction of their orbit within the resonance position. This effect leads to the well-known rabbit-ear shape of the fast ion distribution function (as described also in section 2.4.3). In fig. 5.29, the velocity space region for trapped orbits, which have their banana tip at the resonance layer, is shown with a line, and it coincides well with the second high energy tail in the tomography. This tail can originate both from hydrogen and deuterium, because both species are subject to the resonance localization. In fact, for deuterium the resonance localization effect might be even stronger: The low $v_{\parallel}$ close to the banana tip goes along with high $v_{\perp}$ and hence large Larmor radii, which makes second harmonic absorption more effective. We can conclude that the tomography results are qualitatively in line with basic theoretical considerations.

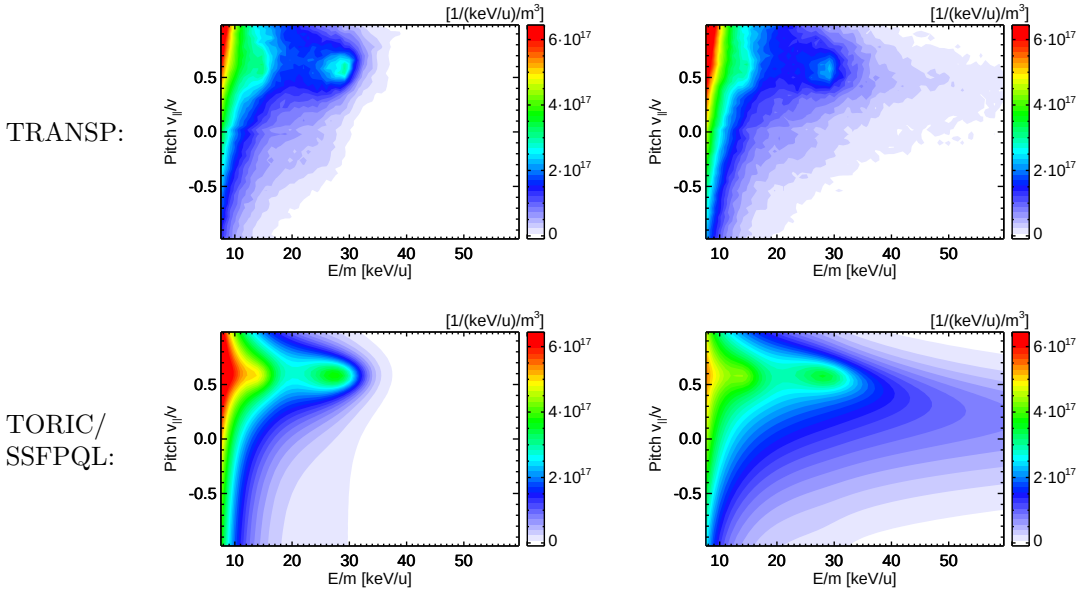

(a) 4.48s (NBI only) **(b)** 4.60s (NBI+ICRH)

Figure 5.30: Calculated D distribution functions by TRANSP (top row) and TORIC/SSFPQL (bottom row).

5.4.4 Comparison with theory

Code overview

In the following, we turn to a quantitative comparison with predictions with the TORIC-SSFPQL code and the TORIC MC kick operator in TRANSP/NUBEAM. TORIC-SSFPQL gives the steady-state H and D distribution as output. The NBI source (i.e. the deposition) is calculated by SINBAD. The main limitations of the code package are, that the Fokker-Planck part SSFPQL neglects all orbit effects, i.e. it assumes zero orbit width and does not consider particle trapping. The latter has the consequence that TORIC-SSFPQL cannot predict realistic pitch distributions, especially when particle trapping is important. Nevertheless, the energy distribution can be compared to experimental signals.

The TRANSP/NUBEAM package delivers only the fast D (i.e. beam ion) distribution function. Hereby, all orbit effects are taken into account by a Monte Carlo approach, and the effect of 2nd harmonic ICRH is modeled by applying kicks to the Monte Carlo markers during their pass through the resonance layer. With this approach, it is also able to model dynamical processes (and not only the steady-state solution). To get the full D distribution function, we add the thermal D distribution modeled by a shifted Maxwellian (2.9). For hydrogen, only parallel and perpendicular temperatures are given in the output, such that we model the H distribution function with a Bi-Maxwellian.

Deuterium

The calculated fast D distribution function are shown in fig. 5.30 for both codes. In the NBI phase, fairly good agreement between both codes is seen. The FIDA tomography (fig. 5.28a) shows less pronounced peaks and a more smoothed out velocity distribution.

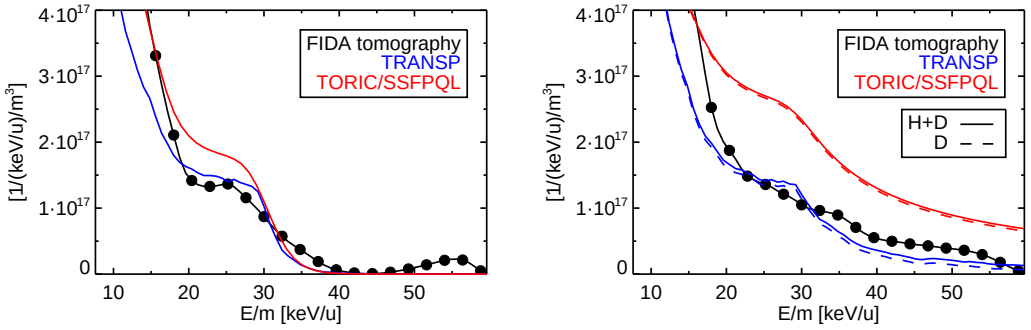

(a) 4.48s (NBI only) **(b)** 4.60s (NBI+ICRH)

Figure 5.31: Energy profiles $\int F(E/m, \xi)\mathrm{d}\xi$. Every third pixel of the tomographic reconstruction is plotted with a dot.

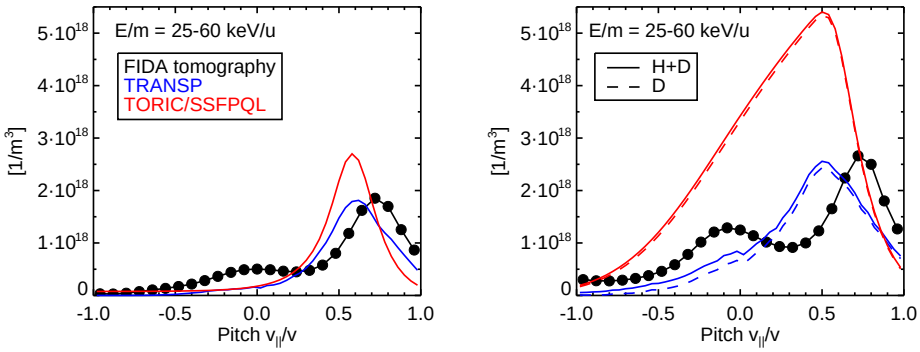

(a) 4.48s (NBI only) **(b)** 4.60s (NBI+ICRH)

Figure 5.32: Pitch profiles $\int_{25\ \mathrm{keV/u}}^{60\ \mathrm{keV/u}} F(\frac{E}{m}, \xi)\mathrm{d}\frac{E}{m}$.

This has been observed already in previous analysis ([48], previous sections). It can be explained by the 1st order Tikhonov regularization, which is used to calculate the tomography and which favors solutions with low gradients. Since the peaks carry mostly geometric information about the NBI setup and the interesting physics aspects lie elsewhere in the velocity space, this seems to be an acceptable limitation. Towards very high energies, a small localized peak in the tomography is seen, which is most likely an artefact due to measurement noise or small impurity lines.

To allow a more quantitative comparison, we compute energy and pitch profiles (figures 5.31 and 5.32) by integrating out the other coordinate, respectively. Both energy and pitch profiles show good agreement. In the energy profile, it can be seen again clearly that the FIDA tomography tends to smooth the energy step at the highest injection energy (30 keV/u). In the simulation, this is a rather sharp step, with a very weak high-energy tail due to collisional velocity diffusion. In general however, the absolute values between tomography and simulation match quite well, especially if one integrates over the region around the step. This can be seen in the pitch profile (fig. 5.32), for which we have integrated over E=25-60 keV/u. The NBI injection peak differs in the tomography by a shift of ≈ 0.1 in pitch, which is within the uncertainties of the tomographic reconstruction. Towards $\xi = 0$, a second small peak appears in the reconstruction, which could be explained by trapped particles.

We turn now to the NBI+ICRH phase. Contour plots of the calculated D distribution function for the considered measurement position in the plasma center are shown in fig. 5.30. TORIC-SSFPQL predicts a much stronger second harmonic high energy tail than TRANSP. The TRANSP high energy tail is located at same pitch as the beam injection peaks, in accordance with the stronger high energy tail seen in the tomography. A second high energy tail (as seen in the FIDA tomography) is hardly visible in the contour plot. In the pitch profile (fig. 5.32), calculated by integration over the high-energy range (25 keV/u - 60 keV/u), it can be seen that TRANSP predicts at least a strong increase at $\xi \approx -0.1$ compared to the NBI only case. Thus, also TRANSP predicts an increased phase-space density corresponding to trapped fast ions with their banana tip close to the resonance, but this enhancement is smaller than in the FIDA tomography.

In the energy profiles (fig. 5.31), the acceleration of beam ions is clearly seen in the FIDA tomography by a high energy tail. For comparison, the FIDA tomography goes to zero at ≈ 40 keV/u in the NBI-only phase. The deuterium energy profile calculated by TRANSP and TORIC/SSFPQL are shown with dashed lines in blue and red, respectively. The TRANSP prediction is below the FIDA tomography, while the TORIC/SSFPQL is too high. However, for a fair comparison, the hydrogen contribution to the FIDA tomography must be added. It is already plotted in figures 5.31 and 5.32, and we will discuss it in details in the next section.

The hydrogen contribution

The TORIC/SSFPQL code gives the hydrogen distribution function directly as output, while TRANSP yields only parallel and perpendicular temperatures. The respective profiles are shown in fig. 5.33 for the considered time point (4.6s). For comparison, the parallel and perpendicular temperatures of TORIC/SSFPQL are shown with a dashed line. They are defined via the average energies of the distribution function: $T_\parallel = 2\langle E_\parallel \rangle$ and $T_\perp = \langle E_\perp \rangle$. The ICRH accelerates hydrogen mainly in the core region between $\rho_{\mathrm{tor}} = 0.0 - 0.4$. Here, the predicted $T_\perp$ from TORIC/SSFPQL is about a factor of two higher than from TRANSP, while $T_\parallel$ is similar.

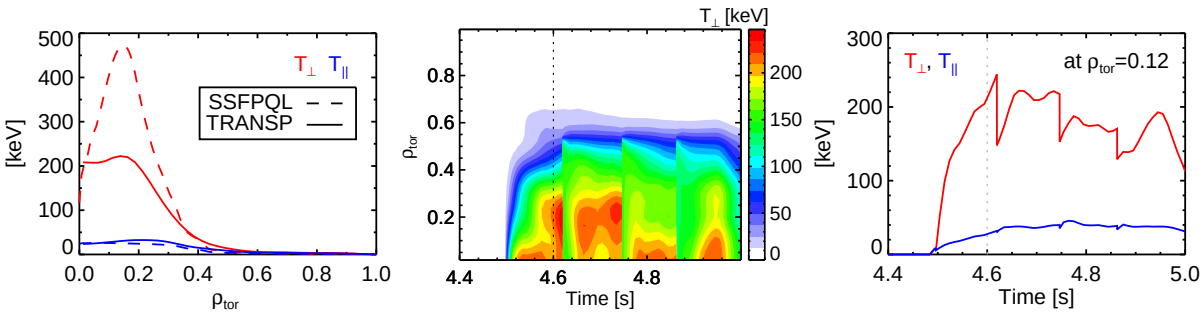

Figure 5.33: Perpendicular and parallel hydrogen temperatures $T_\perp$ and $T_\parallel$. From left to right: Profiles at 4.6s; contour plot of the temporal evolution of the $T_\perp$-profile (TRANSP); time traces at $\rho_{\mathrm{tor}} = 0.12$ (TRANSP).

A possible explanation for this deviation could be that the considered time point (4.6s) is too close to the ICRH switch-on at 4.5s, such that a steady state is not reached yet

(as it is assumed by TORIC/SSFPQL). However, the temporal evolution of the hydrogen temperatures, as calculated by TRANSP and shown in fig. 5.33, do not support this explanation. The considered time point lies well after the strong rise of the temperatures, and the temperatures do not get significantly higher later on. Hence, steady state conditions can be assumed for 4.6s and results from results from TRANSP and TORIC/SSFPQL can be compared. It should be noted that both codes use a similar total ICRH power. In fact, TORIC/SSFPQL predicts a lower hydrogen heating power than TRANSP (1.25 MW vs. 1.61 MW, compare also fig. 5.39) in favor of stronger D heating.

The values of $T_{\parallel}$ and $T_{\perp}$ from TRANSP can be used to model the H distribution function with a Bi-Maxwell-Boltzmann distribution. For the considered measurement position ($\rho_{\mathrm{tor}} = 0.12$ on the low field side), this is shown in fig. 5.34 in comparison to the TORIC/SSFPQL H distribution function. The general shape of the Bi-Maxwellian

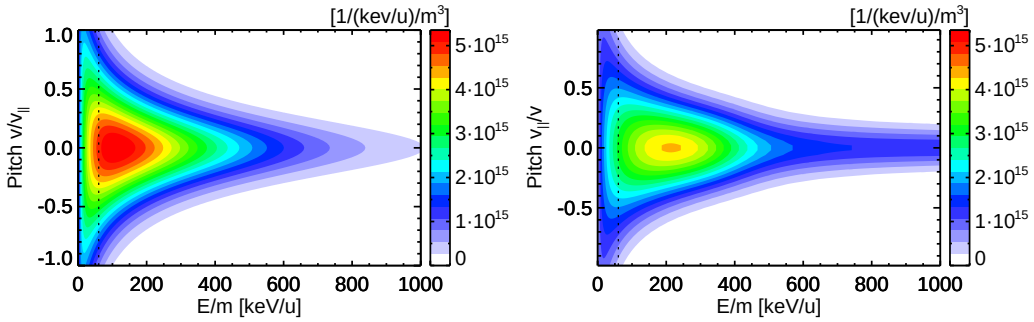

(a) TRANSP (Bi-Maxwellian) **(b)** TORIC/SSFPQL

Figure 5.34: Hydrogen distribution functions. The FIDA tomography observes only the small region on the left of the dashed line.

matches well with the TORIC/SSFPQL calculation. It has to be noted, that both distribution functions do not include orbit effects, (e.g. particle trapping), which would lead to resonance localization and the typical rabbit-ear shape. The velocity space region which is observed by the FIDA tomography (< 60 keV/u) is indicated with a dashed line. Due to high $T_{\perp}$, a large fraction of hydrogen is located at much higher energies, which are no longer observable by the FIDA diagnostic, because the charge exchange cross-sections decrease strongly. The part which is observable, shows a rather broad pitch distribution. Hence, for high hydrogen temperatures, the hydrogen contribution to the FIDA tomography can be considered as a smoothly spread background, but well localized peaks or high energy tails in the tomography cannot be explained by hydrogen. The H contribution gets weaker with increasing H temperatures, because the phase space density is then lowered in the FIDA energy region (< 60 keV/u).

The sum of hydrogen and deuterium is shown in the energy and pitch profiles (figures 5.31 and 5.32) with full lines. For TRANSP, the hydrogen contribution is stronger than for TORIC/SSFPQL, because of its lower H temperatures. Nevertheless, hydrogen cannot explain the difference between TRANSP and the tomography, which suggests that TRANSP is underestimating the D acceleration by second harmonic ICRH in the observed energy range.

In this section, we have demonstrated that the FIDA tomography is able to detect an ICRH-induced high energy tail in the center-most measurement position. TRANSP predicts a weaker and TORIC/SSFPQL a stronger tail. In the next section, we will investigate the other, more-outward radial positions, for which FIDA tomographies can be calculated, and study the radial dependence.

5.4.5 Radial dependence

We have calculated FIDA tomographies at six different radial positions (all on the low field side). The lines of sight, which have been grouped for each position, are indicated in fig. 5.26 by boxes. All radial positions have at least three FIDA views, and half of them (like the center-most one, which we have discussed in the previous section) have an additional fourth FIDA view. Contour plots of the reconstructed fast-ion velocity distribution are shown in fig. 5.35 for all positions, and the NBI-only and NBI+ICRH phase.

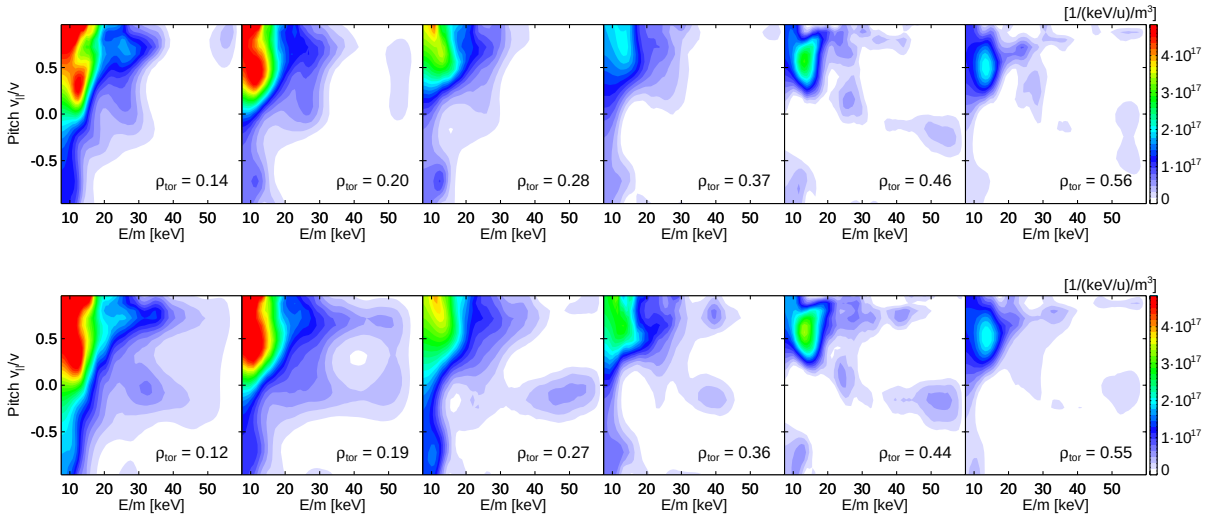

Figure 5.35: FIDA tomographies at different radial positions. Top: 4.48s (NBI only), bottom: 4.60s (NBI+ICRH)

In the NBI only phase, all radial positions show mainly fast ions below the injection energy (30 keV/u), as it is expected. Also, the reconstructed distribution is aligned around $\xi \approx 0.6$, which is very well in agreement with the geometry of NBI Q3. Moreover, the basic shape of the distribution function is in agreement with the theoretical prediction, plotted in figure 5.36. Above the injection energy some randomly distributed small peaks are visible which can be identified as artefacts. Most artefacts are seen in the two outer-most radial positions. This can be explained because these channels have the worst signal-to-noise ratio, since the fast-ion density is much lower in those channels. In addition, most of the artefacts appear towards high energies $E/m > 50$ keV. This might be explainable by the fact that the absolute values of the FIDA weight functions (which yield how many photons are emitted by a given fast ion) decreases towards high energies, because the charge exchange cross-sections go down. Hence, a small perturbation in the FIDA signal gets translated into more fast ions in the tomography towards higher energies. The area below 50 keV is much less affected by artefacts, and is well suited for the physics analysis.

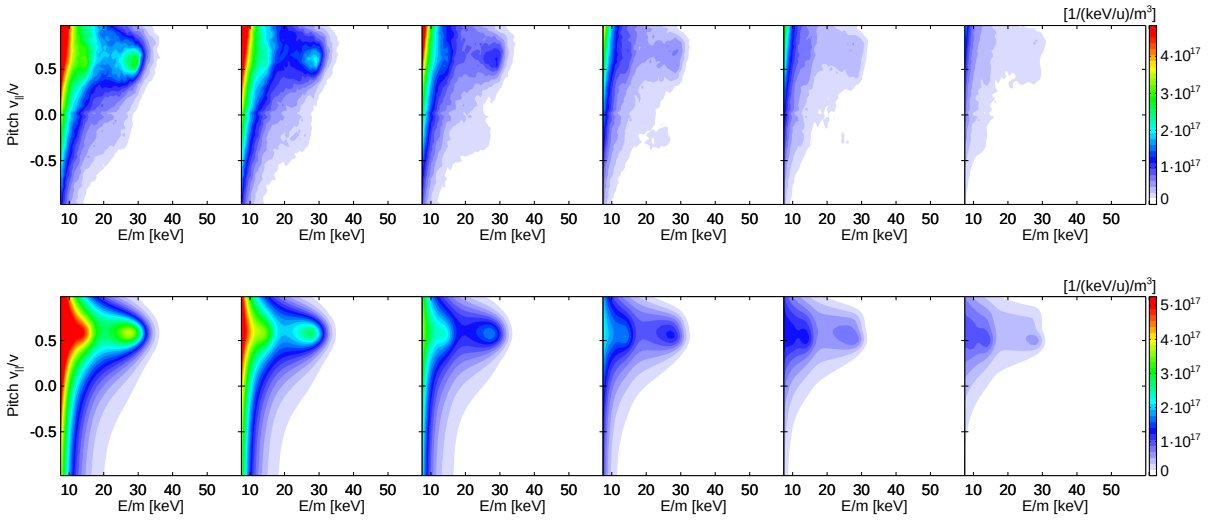

Figure 5.36: Calculated D fast-ion distribution from TRANSP (top) and TORIC/SSFPQL (bottom) in the NBI-only phase (4.48s).

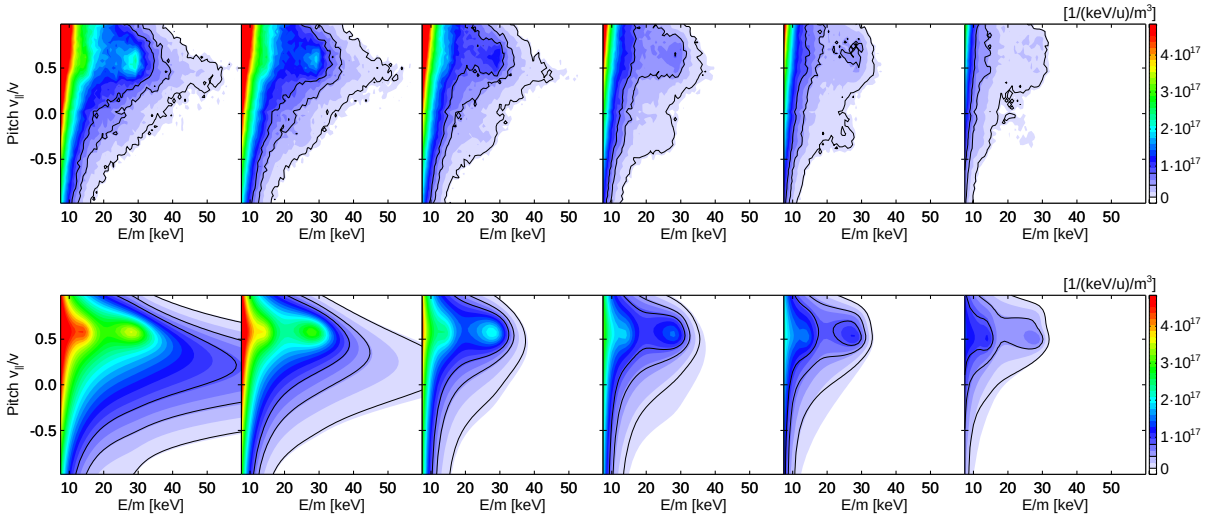

Figure 5.37: Calculated H+D fast-ion distribution from TRANSP (top) and TORIC/SSFPQL (bottom) in the NBI+ICRH phase (4.60s). The color scale refers to the sum of hydrogen and deuterium. For comparison, the first, third and fifth contour line are drawn in black for the sole deuterium distribution.

In the NBI+ICRH phase, high energy tails above the injection energy are clearly seen in the two center-most positions. The tails get weaker in the two intermediate radial positions ($\rho_{\mathrm{tor}} = 0.27$ and $\rho_{\mathrm{tor}} = 0.36$). In the two outermost positions ($\rho_{\mathrm{tor}} = 0.46$ and $\rho_{\mathrm{tor}} = 0.55$), only weak structures are left, which cannot be clearly distinguished from artefacts anymore.

The contour plots of the calculated deuterium distribution by TRANSP and TORIC-SSFPQL are shown in fig. 5.36 and 5.37. To compare simulation results and FIDA tomography quantitatively, we compute radial profiles by integrating in the velocity space over an energy region of interest I and over all pitches: $\int_I \int_{-1}^{+1} F(\frac{E}{m}, \xi) \mathrm{d}\frac{E}{m} \mathrm{d}\xi$. We define two such regions of interest: $I_1 = [20, 35]$ keV/u and $I_2 = [35, 50]$ keV/u. The first interval

corresponds to the highest energy component of the beam ions, such that we can compare radial profiles of the full-energy beam ion density. The upper boundary of the interval has been chosen such, that we integrate over the area, where the step at the injection energy is typically smeared out in the FIDA tomography (comp. fig. 5.31). The second interval $I_2 = [35, 50]$ keV is aligned then towards high energies, and measures the fast-ion density in high energy tails, well above the NBI injection energy. The upper boundary is set to 50 keV/u to avoid picking up artefacts which are visible in the tomography above this boundary.

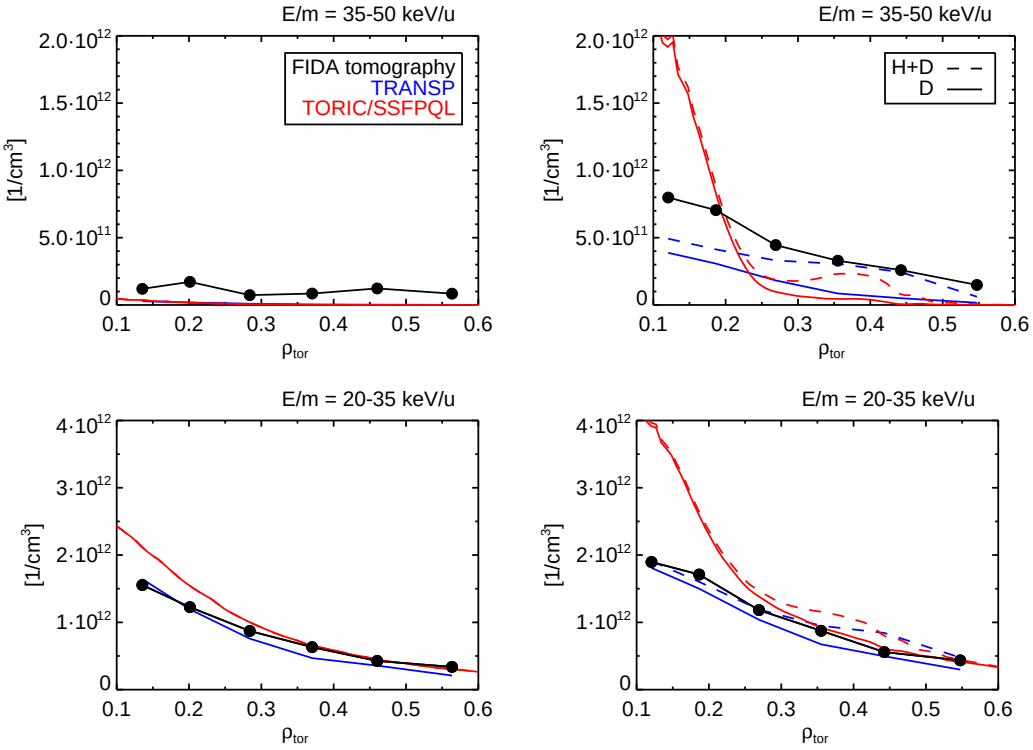

(a) 4.48s (NBI-only) **(b)** 4.60s (NBI+ICRH)

Figure 5.38: Radial fast-ion profiles.

The resulting profiles for both the NBI-only and NBI+ICRH phases are shown in fig. 5.38. For the NBI-only phase, excellent agreement is found between the beam-ion density (I_1) of TRANSP and the FIDA tomography. The SSFPQL solution appears to be more strongly peaked, such that the inner-most point is higher. The high energy region (I_2) shows a FIDA tomography close to zero, as it is expected. This shows, that this energy region is indeed mostly free of tomography artefacts, such that it is well suited for studying high energy tails.

In the NBI+ICRH phase, again good agreement is found between TRANSP and the FIDA tomography for the beam ions in the interval $I_1 = [20, 35]$ keV. The hydrogen contribution is very small compared to the beam ions, and does not change the picture significantly. As in the NBI-only phase, the TORIC/SSFPQL prediction shows good agreement in the outer plasma, but appears higher and more strongly peaked towards the plasma center. In the NBI+ICRH phase, this deviation is even higher than in the NBI-only phase.

In the high energy region I_2, the FIDA tomography shows a peaked profile. This is within expectations, since the ICRH resonance layer is situated close to the magnetic axis. Also, this proofs that passive FIDA light (from the plasma edge) does not contribute significantly to the signal, as it would be visible in all lines of sight. It can furthermore be seen, that the TRANSP prediction is lower than the measured value for the three central positions, also if the hydrogen contribution is taken into account (plotted with the dashed line). This is in line the results, which we have found for the inner-most radial position in the previous section. For $\rho_{\mathrm{tor}} > 0.3$ good agreement is found between the FIDA tomography and the H+D estimate from TRANSP. The TORIC/SSFPQL result shows a different radial behavior: At $\rho_{\mathrm{tor}} = 0.12$, the high energy tail is much higher than the FIDA tomography, as discussed already in the previous section. At $\rho_{\mathrm{tor}} = 0.19$, the TORIC/SSFPQL is in agreement with the FIDA tomography, and further out it is lower and goes faster to zero (also in comparison to TRANSP).

To some extent this might be explainable by the zero-orbit-width approximation which is assumed in TORIC/SSFPQL. Taking into account the orbit widths should lead to a broadening of the profile, which could improve the agreement with the experimental data. In a very rough approximation, this argument can be checked by comparing the radial integrals over the I_2-profiles. Here, the differential volume $\mathrm{d}V/\mathrm{d}\rho_{\mathrm{tor}}$ must be taken into account, which is very small close to the magnetic axis and is increasing with ρ_{tor}. If we integrate over $\rho_{\mathrm{tor}} = [0.0, 0.49]$, the integral between the FIDA tomography and TORIC/SSFPQL (H+D) match each other, and both yield $\approx 1.46 \cdot 10^{18}$ fast ions (in the energy interval I_2). This result suggests, that the agreement between the FIDA tomography and TORIC/SSFPQL could be improved, if an additional broadening mechanism (such as finite orbit widths) would be taken into account.

In contrast, the integral over the TRANSP H+D curve yields $\approx 1.12 \cdot 10^{18}$ fast ions, which is ≈77% of the FIDA tomography and thus significantly lower. This might be explainable by the fact that TRANSP distinguishes between thermal and "fast" deuterium (i.e. beam ions). Figure 5.39 shows the distribution of absorbed ICRH power among the

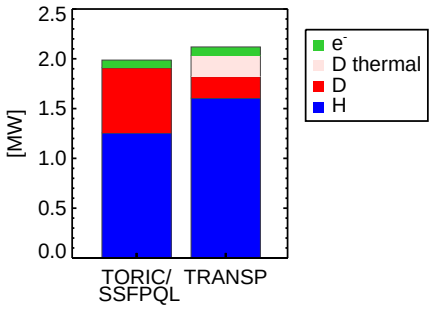

Figure 5.39: Calculated ICRH absorption power for the different particle species. The TRANSP code separates between thermal and fast deuterium ion, while SSFPQL treats them uniformly and consistently.

different plasma species. Absorption by electrons is weak for both codes and does not play an important role. In general, TRANSP predicts, that fewer ICRH power is absorbed by deuterium (2nd harmonic) than TORIC/SSFPQL. In addition, TRANSP separates the 2nd harmonic absorption for thermal and beam ions. The latter is calculated with the MC Kick operator, and appears in the beam-ion distribution function, which we use

for comparison with the FIDA tomography. Due to high T_i, 2nd harmonic absorption is also quite efficient for the thermal D population. In fact, TRANSP predicts slightly more power absorption by thermal deuterium than fast deuterium. However, this thermal contribution is missing in the comparison with the FIDA tomography. TRANSP uses the power for the power balance evaluation, but the thermal D distribution is still considered to be "thermal", i.e. Maxwellian. Deviations from a Maxwellian shape (e.g. high energy tails) are neglected. As mentioned previously, we add the thermal deuterium distribution function to the beam-ion distribution function for the comparison with the FIDA tomography. Nevertheless, high energy tails originating from the acceleration of thermal D are not included in this approach, as they are not given in the TRANSP output. This could explain, why in the TRANSP prediction is lower than the FIDA tomography.

It is interesting to note that in the region around $\rho_\mathrm{tor} \approx 0.35 - 0.40$, the hydrogen contribution is increased both in the TRANSP and TORIC/SSFPQL results. Since we have assumed a constant hydrogen concentration of 5% in the whole plasma, and the electron density is rather flat in the core region, this can only be explained by the hydrogen temperature profiles (fig. 5.33): At $\rho_\mathrm{tor} \approx 0.35 - 0.40$, the perpendicular hydrogen temperature falls down to values in the range of $T_\perp \approx 50\,\mathrm{keV}$. Hence, a much larger fraction of the H distribution function lies in the energy region observed by the FIDA tomography. Further outward, the hydrogen contribution vanishes as H temperatures approach thermal levels, and further inwards the H temperatures are too high, such that only a small fraction of their velocity distribution intersects with the FIDA tomography energy range.

5.4.6 Comparison with other fast-ion measurements

In this section, we want to compare how the effect of 2^nd harmonic ICRH on the beam ion distribution is measured by other fast-ion diagnostics.

Neutral particle analyzer

Fig. 5.40 shows measurements of the recently installed active neutral particle analyzer (aNPA) [46] for the same time points as above. Here, the NPA detector measures fast-ions with pitches $\xi \approx 0.6$ and is mainly sensitive to energies above 40 keV. Lower energies are blocked by an aluminum foil. During discharges an increasing noise level - likely due to heating up of the detector - can obscure also particles with higher energies, in the presented case up to 60 keV. In comparison to the measurement, we show the theoretical prediction from TRANSP and TORIC/SSFPQL both for H and D. They are calculated by forward-modeling the distribution functions with FIDASIM, which is equipped with a synthetic NPA diagnostic. The aNPA is not absolutely calibrated, such that the forward-modeled prediction needs to be scaled to allow a shape comparison. Hereby, we have matched absolute values of the NBI-only simulations to the experiment at around 65 keV, and used the same scale factor for the NBI+ICRH simulations.

In the NBI-only phase, both codes predict a much steeper fall-off above the injection energy than it is measured. This feature is regularly observed with the active neutral particle analyzer [46], and it is not yet understood if it is a diagnostic effect or it carries real physics. In any case, it could be excluded that it is neither background nor noise, because the signal vanishes completely in phases without NBI or ICRH.

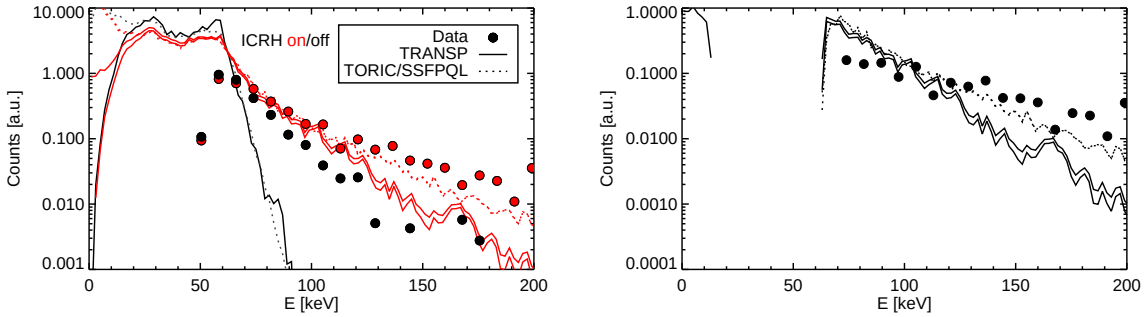

(a) 4.48s (NBI-only, black) and 4.60s (NBI+ICRH, red)

(b) Difference between both time points

Figure 5.40: Measurements from the active neutral particle analyzer in comparison with theoretical prediction. For the NBI+ICRH phase, the calculated D fluxes and the H+D fluxes are both shown. For TRANSP, the H+D fluxes are identified by the higher line. For TORIC/SSFPQL, the D fluxes are already so high that the H+D fluxes are almost identical.

In the NBI+ICRH phase, an increase of the measured high-energy tail is observed. Forward-modeling suggests that the hydrogen contribution to the NPA flux is low, such that we can interpret this as a confirmation of deuterium acceleration due to 2$^{\text{nd}}$ harmonic ICRF absorption. The measured high energy tail is flatter than the prediction by both codes, whereby the agreement with TORIC/SSFPQL is better. This finding holds also, if the difference between the NBI-only phase and NBI+ICRH phase is considered (fig. 5.40b).

Neutron rates

Another diagnostic principle, which is very sensitive to fast deuterium ions, is the measurement of neutrons resulting from the D-D fusion reaction. An advantage of this method is, that no contribution from hydrogen has to be considered, as hydrogen does not produce neutrons (neither in H+H nor in H+D reactions).

Fig. 5.41 shows the raw data of three different neutron rate measurements, labeled as FIS2, FIS3 (two fission chambers with different sensitivity) and NES (a recently installed neutron spectrometer [47]). All three detectors do not have a proper absolute calibration, such that we had to match the signal by applying constant factors, which was done in the NBI-only phase at 4.48s. The temporal evolution of FIS2 and NES agrees nicely in the NBI-only phase. FIS3 seems to suffer from a constant off-set or background, since it is not zero at 4s, where the NBI was switched on initially. At the ICRH switch-on at 4.5s, all detectors see a strong increase of their signal, which indicates that the deuterium beam ions are accelerated to higher energies. However, FIS2 and FIS3 show a much more rapid increase of their signal than NES. Later-on, FIS2 stays at lower signal levels than FIS3, which indicates that FIS2 is out of its proportionality regime and saturates.

Fig. 5.41 shows a comparison of the NES signal to theoretical prediction by TRANSP and TORIC/SSFPQL. The latter calculates only the steady state solution, which is shown with dots for the two time-points. TRANSP calculates the full temporal evolution of the neutron rate. To compare measurement and theory, the uncalibrated measurements were

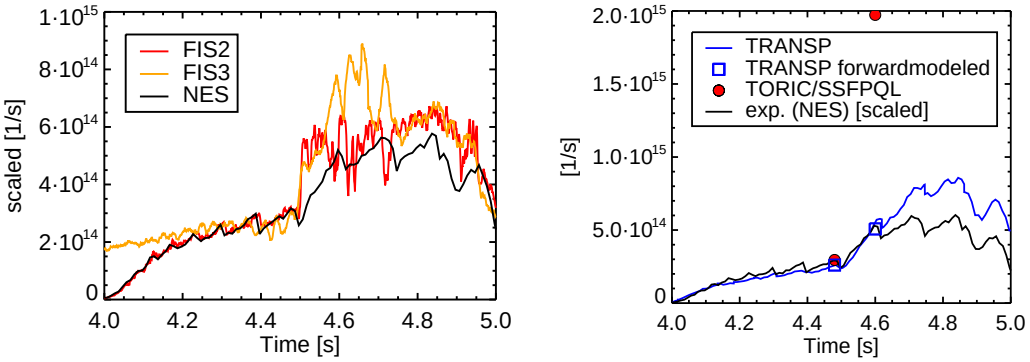

Figure 5.41: Neutron measurements. Left: Signal of three different Neutron detectors. Right: Comparison of the NES signal with theoretical predictions. All experimental signals are scaled to match the TRANSP prediction at ≈ 4.48 s.

scaled to the TRANSP prediction at 4.4s. It should be noted, that the codes calculate the volume integrated neutron rate, while the diagnostic measures a line integrated neutron rate (along its line of sight). To take this into account, we have used a synthetic NES diagnostic, which is able to forward model synthetic signals (shown with blue symbols) from the TRANSP output.

The signal rising rate of NES after the ICRH switch-on matches well with the TRANSP prediction. This gives the very strong suggestion that the very rapid signal increase measured by FIS2 and FIS3 is not real, but rather a spurious signal which might be linked to the ICRH onset. Hence, NES appears to be the best signal to benchmark the theoretical predictions, which has also been observed in other discharges.

Both theoretical codes predict very similar neutron rates in the NBI-only phase. With respect to that, TRANSP predicts a neutron enhancement in the NBI+ICRH phase at 4.6s of a factor of two, which is in reasonable agreement with the measured data. The calculation including diagnostic effects (based on forward-modeling) is shown with blue symbols, and it fits even slightly better to TRANSP. In contrast, TORIC/SSFPQL predicts a much stronger increase (factor ≈ 7), which is not in line with the measurement.

In the analysis of the FIDA tomography, we have seen that TORIC/SSFPQL predicts too strongly peaked fast-ion density profiles. The neutron rate is proportional to the quadratic fast-ion density, such that this might explain, why TORIC/SSFPQL seems to over-predict the neutron rate.

Furthermore, we have concluded from the FIDA tomography that TRANSP a weaker fast-deuterium high energy tail at the two inner-most FIDA measurement positions. The fact that the total neutron rate agrees quite well with TRANSP predictions must not be a contradiction, because the neutron rate measurement integrates both over real and velocity space, and thus might not be sensitive enough for such small and localized deviations.

It should be noted, that the neutron rate is reduced by increasing Z_{eff}. This is problematic for the analysis of neutron rates, because the temporal evolution of Z_{eff} cannot be measured reliably. For the TRANSP calculations, we have assumed that it is time-invariant. In TORIC/SSFPQL, impurities are not considered at all and the plasma is assumed to consist purely of hydrogen and deuterium. It might be that the impurity content increases after switching on ICRH, due to sputtering induced by the antenna

currents and fields. This is often observed in ASDEX Upgrade experiments. In addition, no ECRH is used in this discharge to counter-act a possible impurity accumulation. This has to be kept in mind when drawing quantitative conclusions from the neutron rate.

5.4.7 Conclusions

In this section, we have demonstrated that the FIDA tomography is a valuable tool to analyze 2nd harmonic ICRH beam ion acceleration. We have discussed that the tomography yields a sum of the hydrogen and deuterium distribution as function of E/m and the pitch ξ. In the plasma center, the tomography yields distinct high energy peaks, which we could interpret as deuterium ions, accelerated by 2nd harmonic ICRH absorption. In contrast, the hydrogen distribution function is expected to have a rather broad and uniform shape in the considered energy range.

Furthermore, we have presented FIDA tomographies at six radial positions in total. This is in particular the first time, that a profile of the velocity distribution is reconstructed from measurements. The high energy tails are only seen in the center-most channels, where the ICRH deposition is expected.

Comparisons have been carried out with numerical simulations from the TRANSP code and TORIC/SSFPQL code and other fast-ion diagnostics. TORIC/SSFPQL predicts more strongly peaked fast-ion profiles as measured by FIDA. This results in an overestimated neutron rate, where the fast-ion density enters quadratically. Energy spectra measured with the NPA (and thus integrated over a broad region in the plasma center) show reasonable agreement.

TRANSP predicts a slightly weaker high energy tail than measured by the FIDA tomography, especially in the plasma center. This is in accordance with observations made in NPA measurements. At the same time, we find good agreement between FIDA and TRANSP for the beam-ion part of the fast-ion distribution function. The neutron rate predicted by TRANSP matches quite well with experimental measurements. This could be interpreted such, that the neutron production is dominated by the fast ions around or below the NBI injection energy, for which we have found good agreement to FIDA as well.

6 Summary and outlook

This thesis focuses on the physical behavior of fast ions in tokamak plasmas. This is an important field of research for the success of future fusion devices such as ITER and DEMO, because external heating mechanisms (in particular: neutral beam injection, ion cyclotron heating) and the ignition of a fusion plasma (heating by fusion α-particles) rely on fast ions that transfer their energy to the bulk plasma by collisions. In addition, fast ions are utilized to drive plasma currents non-inductively (e.g. neutral beam current drive) or to increase and maintain plasma rotation. Within this thesis, work has been carried out both on modeling aspects and experimental observations.

A new model to calculate the NBI fast-ion distribution rapidly has been developed. It is based on a combination of existing codes and existing analytic solutions. The neutral beam deposition is calculated with the FIDASIM code. An orbit code is then used to average the deposition over the first fast-ion orbit, such that basic orbit effects (e.g. particle trapping and profile broadening due to finite orbit widths) are taken into account. Finally, the slowing down distribution of the injected fast ions is calculated with an analytic solution of the Fokker-Planck equation. From the fast-ion distribution, important profiles can be calculated, such as pressure and current-drive profiles. These profiles are used e.g. to improve the reconstruction of the magnetic equilibrium. The model is benchmarked with the more sophisticated but slower TRANSP/NUBEAM code, and good agreement is found.

The experimental work utilizes mainly the FIDA (Fast-ion D-alpha) diagnostic, which is based on spectroscopic observation of the Doppler-shifted D-alpha light, originating from fast ions after charge exchange reactions. Here, the shape of the Doppler spectrum yields information about the fast-ion velocity distribution. Observation from different angles (with respect to the magnetic field) corresponds to observation of different velocity space regions.

A major upgrade of the diagnostic has been carried out with the goal to enable the tomographic reconstruction of the 2D fast-ion velocity distribution from the FIDA raw signals, under a wide range of plasma parameters. To do so, the spectrometer design was refurbished. In particular, a former high-pass interference filter was replaced with a wire to filter the bright, unshifted D-alpha line. This allows to measure both the blue- and red-shifted part of the Doppler spectrum instead of just one part and thus doubles the information about the velocity space for a given line of sight. In addition, two new optical heads have been installed in ASDEX Upgrade. Their position and viewing angle were chosen in such a way to complement the existing three viewing arrays in an optimal way in the plasma center.

These diagnostic upgrades allow the tomographic reconstruction of the 2D fast-ion velocity distribution at several radial positions on the low-field side. A tomography code has been implemented based on 1st order Tikhonov regularization. The velocity space accuracy of the tomography is then tested in a MHD-quiescent plasma and a comparison between 60 keV and 93 keV NBI. Here, the tomography is found to be well able to distinguish between both injection energies, and determine the expected pitch distributions.

A comparison to TRANSP/NUBEAM shows good agreement. This proves the reliability of the FIDA tomography results and allows us to investigate physical questions.

The FIDA tomography is applied to study the velocity-space dependence of fast-ion redistribution during sawtooth crashes. Here, it is found, that fast ions with high energies and pitches close to zero are less affected by the sawteeth than fast ions with high pitches or lower energies. This is in good agreement with theoretical considerations, which explain these observations by the fact that ions with high energies and pitches close to zero have large drift velocities (compared to their parallel velocity) and are thus weaker bound to the magnetic field lines. This allows a part of these ions to escape from the redistribution during the sawtooth crash.

Furthermore, fast-ion transport induced by Alfvén eigenmodes is studied. The current-ramp up of a discharge with early NBI heating is analyzed, where the q-profile is still reversed. The NBI fast-ions destabilize reversed shear Alfvén eigenmodes (RSAEs) and toroidicity-induced Alfvén eigenmodes (TAEs) which are both seen in fluctuation diagnostics. Synchronized with a RSAE cascade, where at least four RSAEs appear simultaneously, the FIDA radiation is observed to drop in all radial measurement positions inside the RSAE localization. With the FIDA tomography, the signal drop can be related to a fast-ion density drop of 10%. In the tomography, the fast-ion density drop appears rather uniformly in the velocity space. Certain regions with a strongly increased or decreased effect of the RSAEs are not identified. This measurement will serve as an important benchmark case for modeling codes that will be used to extrapolate the result to future machines.

Finally, we investigate the acceleration of fast deuterium ions by 2nd harmonic ion cyclotron resonance heating. Therefore, a phase within a discharge with NBI only is compared to a phase with NBI+ICRH. In this ICRH scenario, hydrogen is resonant at the first harmonic. Since a residual hydrogen concentration of about 5% is typically present at ASDEX Upgrade, it absorbs ICRH power in competition with deuterium and needs to be considered in the data analysis. We show that the FIDA tomography can be interpreted as sum of the deuterium and hydrogen distribution function, if it is written as function of E/m. In the NBI+ICRH phase, the tomographic reconstructions in the plasma center yield two distinct high-energy tails above the NBI energy, which are not present in the NBI-only phase. Basic theoretical considerations suggest, that the hydrogen distribution function is much broader in the considered energy range. Hence, hydrogen can contribute to the total integral over the peaks, but the well-defined shape of the peaks suggest that they originate mainly from deuterium.

In total, we calculate tomographic reconstructions at six radial positions that span a broad range of the plasma. This is the first time that a radial profile ($f(E, \xi, \rho)$ of the fast-ion distribution function is reconstructed from FIDA measurements. The high-energy tails vanish in the outer-most radial positions, which is in agreement with the expected ICRH deposition position.

A comparison to theory is carried out with predictions from the TRANSP/TORIC and TORIC/SSFPQL codes. In the NBI-only phase good agreement can be concluded between both codes and experimental observations. In the ICRH phase, TORIC/SSFPQL predicts a too strongly peaked fast-ion profile, which could be caused by missing orbit effects in the code. This results also in a strong over-prediction of the neutron rate. In contrast, TRANSP/TORIC is able to predict the ICRH-induced neutron rate en-

hancement in good agreement with measurements. The FIDA tomography allows a more detailed comparison (i.e. spatially and velocity-space resolved). This reveals that the high-energy tails (above the NBI energy) are under-estimated by TRANSP/TORIC in the very plasma center. For lower energies (around and below the NBI energy) good agreement is found.

Outlook

In this thesis, we have established and verified the technique of reconstructing the fast-ion velocity distribution by tomographic inversion, and presented several physical studies.

Within this work, we have neglected the spatial extension of the FIDA measurement volumes during the tomography process. Instead, we have combined views at similar radial positions and assumed that they measure at the same spatial position. The reasonable results and good agreement to TRANSP in MHD-quiescent NBI cases justify these assumptions. By applying this 2D tomography independently at several radial positions, we are able to infer $f(E, \xi)$ at each of these positions, and thus get already something similar to a 3D distribution function $f(E, \xi, \rho_{\mathrm{tor}})$

Nevertheless, an improvement could be possible by extending the tomography itself with a radial coordinate (e.g. ρ_{tor}). Consequently, the weight functions W would become functions of ρ_{tor} (and thus 3D functions for each wavelength), and the tomography would yield directly a 3D distribution function $f(E, \xi, \rho_{\mathrm{tor}})$. Some prerequisites were already carried out. To calculate the radial dependence of the weight functions, only a very small modification of FIDASIM was necessary, and exemplary results are shown in fig. 6.1. Here, we assume a radial ρ_{tor}-grid with 10 bins (ranging from 0 to 1), and show $W(E, \xi)$ for a single line of sight of the 10° view at all radial positions, were it is non-zero. The finite radial resolution leads to the fact, that it is non-zero in four ρ_{tor}-bins (yet strongly peaked in the $\rho_{\mathrm{tor}} = 0.15$ bin, note the different color scales). Furthermore, the shape changes slightly over the different radial positions. This is due to the change of the local angle Φ between the magnetic field and the line of sight along a given line of sight. The conventional weight functions used for the 2D tomography average over these changes, and are given as a sum over all radial positions.

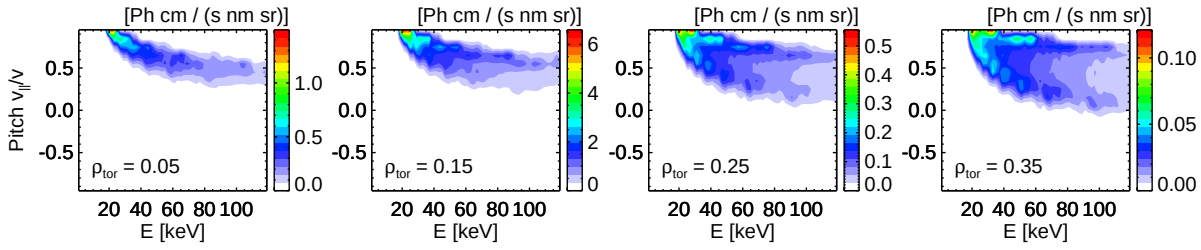

Figure 6.1: Radially dependent weight function for a central line of sight of the 10° view.

An overview of the 3D weight functions for all lines of sight is given in fig. 6.2. Here, the local value of Φ is shown as function of the ρ_{tor}-bin. The integral $\iint W \mathrm{d}E\mathrm{d}\xi / \sum_{\rho_{\mathrm{tor}}} \iint W \mathrm{d}E\mathrm{d}\xi$ (i.e. how much the radial bin contributes to the total signal) is indicated both with the symbol size and color. It can be seen that not all lines of sight feature such a strong variation of Φ. The example shown previously in fig. 6.1 features in fact one of the strongest variations. The different radial resolutions can also be seen (comp. also to fig. 4.9).

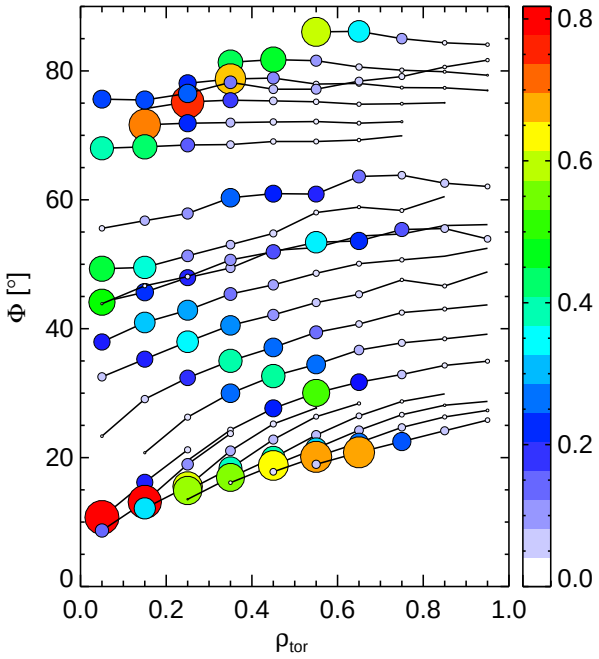

Figure 6.2: Overview over the shape (projection angle Φ) and radial distribution ($\iint W \mathrm{d}E\mathrm{d}\xi / \sum_{\rho_{\mathrm{tor}}} \iint W \mathrm{d}E\mathrm{d}\xi$, symbol color and size) of the 3D weight functions for all FIDA lines of sight. Symbols belonging to the same line of sight are connected with lines.

The drawback of this 3D technique is that the complexity and calculation time increases non-linearly. In first calculation attempts, the 3D tomography took ≈10 minutes versus < 1 second for the 2D tomography. Calculating n independent 2D tomographies just takes the n-fold calculation time of a single 2D topography. Also the preparation of the input spectra is much more complex, if 35 FIDA spectra (instead of five) have to be checked simultaneously for e.g. impurity lines or calibration issues. Since the 2D tomography yields useful results, it might be more beneficial to further exploit this technique first. Nevertheless, the 3D tomography might be an interesting option for future applications. A major advantage of the fully 3D technique would be for example, that other fast-ion diagnostics with less localized measurements (such as passive NPAs or neutron spectra) could be included.

In section 6.4 we have demonstrated for the first time, that it is possible to reconstruct the velocity distributions at several radial positions and thus get a 3D fast-ion distribution $f(E, \xi, \rho_{\mathrm{tor}})$. This could be used to directly derive important profiles from the FIDA measurements, such as the fast-ion density, fast-ion pressure or fast-ion current profiles. It should be noted however, that the FIDA measurement positions are on the low field side. For realistic calculation of the profiles, a flux-surface averaged f would be necessary. Thus, it might be necessary to post-process the reconstruction with an orbit code, to calculate an appropriate flux-surface average. An alternative would be, to re-formulate the tomography in terms of constants of motion (e.g. E, μ, P_φ).

It might be desirable to automatize the tomography procedure, to calculate tomographies for a large number of time points within one shot, or build even databases with many discharges. At the present stage, the spectra must be checked manually for impurity lines (and those must be excluded from the inputs) and the background must be sub-

tracted properly. The weight function must be calculated with FIDASIM for each time point, which requires a preparation of the FIDASIM inputs and a typical calculation time of at least one hour for one time point and all lines of sight. In order to calculate many time points, this calculation time must be decreased significantly, which could be done by using analytic approximations, as presented in [51]. In principle, it should be possible automatize these steps, e.g. develop automatic impurity line detection algorithms etc. However, this will require a considerable amount of work and careful checking, to ensure that the automatization produces reasonable results.

Finally, the tomography could be improved by combining other fast-ion diagnostics [91]. Therefore, the main requirement is, that the measurement can be described by weight functions, similar as the FIDA measurement. For example, the collective Thomson scattering (CTS) diagnostic can be included into the 2D tomography rather straightforwardly, because it has very similar properties as FIDA (e.g. good spatial localization). This has been demonstrated already in [92]. Diagnostics which have a significantly lower spatial resolution, such as passive NPAs or neutron spectroscopy could be included in a 3D tomography, because there finite radial widths of the measurement positions can be included. In addition, some of these diagnostics do not have an absolute calibration (yet), such that they provide mainly information about the shape of the distribution function. For the tomography, however, absolute values are necessary. They could be fitted iteratively in comparison with absolutely calibrated diagnostics (such as FIDA and CTS), such that the shape information from these diagnostics can be included.

Nevertheless, we have demonstrated in this thesis, that already in its present state, the FIDA tomography is a valuable tool for physics studies. These studies can be pursued: E.g., the velocity-dependence of sawtooth redistribution could be studied in other parts of the velocity space by populating them with different fast-ion sources (i.e. different NBI geometries and injection energy, or ICRH).

The presented experimental observations of fast-ion redistribution due to Alfvén eigenmodes could be used, to benchmark theoretical models such as LIGKA/HAGIS [93–97]. Furthermore, the effect of Alfvén eigenmodes could be studied in the current flat-top, which would allow experimental investigations under steady-state conditions. However, the corresponding plasma scenarios have yet to be developed. The dependence of 2nd harmonic ICRH on parameters like the ion Larmor radius, the heating power or the collisionality could be analyzed by parameter scans.

In addition, the enhanced diagnostic capabilities can be further exploited, to address other important issues of fast-ion physics. E.g., fast-ion transport due to other MHD-instabilities, such as neoclassical tearing modes could be investigated.

Danksagung / Acknowledgments

An erster Stelle möchte ich mich herzlich bei meinem akademischen Betreuer Prof. Hartmut Zohm bedanken, der es mir nun schon zum dritten Mal (nach Bachelor- und Masterarbeit) ermöglicht hat, eine Studienarbeit am IPP unter seiner Leitung durchzuführen. Durch seinen Überblick und sein enormes Fachwissen war er dabei immer eine große Hilfe.
Weiterhin bedanke ich mich bei meinem Gruppenleiter Dr. François Ryter, der jederzeit ein offenes Ohr für Fragen und neue Pläne hatte. Danke auch für die Hilfe bei der Planung und Programmierung der Experimente.
Mein größter Dank gilt Dr. Benedikt Geiger für die hervorragende Betreuung während dieser Arbeit. Er hatte immer Zeit für Fragen und Diskussionen und war in vielerlei Hinsicht ein großes Vorbild.

Furthermore, I would like to thank Tomas Odstrčil, for sharing his expertise in tomographies with me and pointing me to the appropriate literature. In addition, I thank the DTU-Team (in particular Prof. Mirko Salewski and Dr. Asger Schou Jacobsen) for the fruitful and ongoing collaboration on velocity-space tomography techniques.
A big thanks goes to Dr. Roberto Bilato for his great efforts in doing the TORIC-SSFPQL calculations and the fruitful discussions during the development of the fast-ion model.
My gratitude goes also to Dr. Michael van Zeeland, for making his orbit calculation code available at ASDEX Upgrade.
An dieser Stelle möchte ich mich auch bei Dr. Giovanni Tardini bedanken, für die enorme Hilfe bei der Erstellung der TRANSP Simulationen sowie die Bereitstellung der Neutronendaten.
Bei Dr. Philip Schneider bedanke ich mich für die Daten der Neutralteilchenanalysatoren und die hilfreichen Diskussionen über die Diagnostik und schnelle Ionen.
Dr. Ivo Classen danke ich für die Auswertung der ECE-Imaging Daten.
Weiterhin bedanke ich mich bei Dr. Manolo García-Muñoz, Nora Lazányi, Joaquin Galdon und dem gesamten FILD-Team für die gute Zusammenarbeit auf dem Gebiet der schnelle-Ionen Physik und die Bereitstellung der FILD-Daten.

Außerdem möchte ich mich herzlich bei alljenen bedanken, die am Einbau der neuen FIDA-Optikköpfe beteiligt waren. Im Besonderen bedanke ich mich bei:
- Sven Klink, Klaus Sauerer und Maximilian Pichl für das Verlegen der Glasfasern in der AUG Torushalle.
- Peter Bischoff für das Schleiffen der Glasfasern, insbesondere auch für das schnelle Reparieren, wenn durch die Ungeschicklichkeit der Physiker wieder einmal eine Glasfaser gebrochen ist.
- Michael Rolffs für das Zusammenbauen der Optikköpfe und die Hilfe bei der Installation im Gefäß.
- Wolfgang Zeidner für die Hilfe bei der Bestimmung der möglichen Optikkopfpositionen, sowie die Vermessung der Sichtlinien mit dem FARO-Arm.
- An dieser Stelle nochmals bei Dr. Benedikt Geiger, der bei der Planung der Optikköpfe maßgeblich mitgeholfen hat, und nicht zuletzt immer die Brotzeit spendiert hat, ohne die die nächtlichen Einbauarbeiten im Torus eine zähe Angelegenheit geworden wären.

Weiterhin gilt mein Dank dem gesamten Team der Werkstatt und Galvanik, die den Bau der Spektrometerbauteile und Optikköpfe ermöglicht haben, sowie der gesamten Gefäßmannschaft.
Dr. Thomas Pütterich, Dr. Eleonora Viezzer and Marco Cavedon danke ich dafür, dass wir zwölf freie Steckplätze an deren Vakuumdurchführung benutzen durften. Danke auch an Marco fürs Einsetzen seiner Kletterfähigkeiten an ASDEX Upgrade, als er mir beim Installieren der Glasfasern an die Vakuumdurchführung in der Torushalle geholfen hat.

Danke an das gesamte Spektroskopie-Team für die gute Zusammenarbeit im Labor und bei den Kalibrationsarbeiten, insbesondere auch an Dr. Ralph Dux und Dr. Eleonora Viezzer, die mir einmal freitags bis spät in die Nacht zur Seite standen, um einen Optikkopf fertig zu kalibrieren. Alexander Bock, Dr. Matthias Reich und David Rittich danke ich für die gute Zusammenarbeit beim Betreiben des MSS-Spektrometers.

A big thanks goes also to my colleagues from Lisbon and Padua for the good time we had during the European PhD network. Also, I would like to thank Prof. Hartmut Zohm for enabling this great experience and useful lecture series.

Abschließend möchte ich mich beim gesamten ASDEX-Upgrade Team für die gute Zusammenarbeit und hervorragende Arbeitsatmosphäre bedanken.

Bibliography

[1] D. Merkl. *'Current Holes' and other Structures in Motional Stark Effect Measurements*. Dissertation, TU München, 2004.

[2] M. Sokoll. MHD-Instabilitäten in magnetisch eingeschlossenen Plasmen und ihre tomographische Rekonstruktion im Röntgenlicht. Technical Report 1/309, IPP, Garching, Germany, April 1997. URL: `http://edoc.mpg.de/get.epl?fid=63289&did=438832&ver=0`.

[3] R. Lüst and A. Schlüter. Axialsymmetrische magnetohydrodynamische Gleichgewichtskonfigurationen. *Zeitschrift für Naturforschung A*, 12(10):850–854, 1957.

[4] V. Shafranov. Plasma equilibrium in a magnetic field. *Reviews of Plasma Physics*, 2:103, 1966.

[5] P.J. McCarthy, P. Martin, W. Schneider. The CLISTE interpretive equilibrium code. *IPP Report 5/85*, Max-Planck-Institut für Plasmaphysik, Garching, Germany, 1999.

[6] I. H. Hutchinson. *Principles of plasma diagnostics*. Cambridge university press, 2005.

[7] V. Kiptily, F. Cecil, O. Jarvis, M. Mantsinen, S. Sharapov, L. Bertalot, S. Conroy, L. Ingesson, T. Johnson, K. Lawson, et al. γ-ray diagnostics of energetic ions in JET. *Nuclear Fusion*, 42(8):999, 2002.

[8] H. Bindslev, J. Hoekzema, J. Egedal, J. Fessey, T. Hughes, and J. Machuzak. Fast-ion velocity distributions in JET measured by collective Thomson scattering. *Physical Review Letters*, 83(16):3206, 1999.

[9] C. Hellesen, M. Albergante, E. A. Sundén, L. Ballabio, S. Conroy, G. Ericsson, M. G. Johnson, L. Giacomelli, G. Gorini, A. Hjalmarsson, et al. Neutron spectroscopy measurements and modeling of neutral beam heating fast ion dynamics. *Plasma Physics and Controlled Fusion*, 52(8):085013, 2010.

[10] W. Heidbrink, K. Burrell, Y. Luo, N. Pablant, and E. Ruskov. Hydrogenic fast-ion diagnostic using Balmer-alpha light. *Plasma physics and controlled fusion*, 46(12):1855, 2004.

[11] M. Garcia-Munoz, H.-U. Fahrbach, H. Zohm, et al. Scintillator based detector for fast-ion losses induced by magnetohydrodynamic instabilities in the ASDEX upgrade tokamak. *Review of Scientific Instruments*, 80(5):053503, 2009.

[12] W. Heidbrink, D. Liu, Y. Luo, E. Ruskov, and B. Geiger. A code that simulates fast-ion D-alpha and neutral particle measurements. *Comm. Comp. Physics*, 8, 2010.

[13] B. Geiger. *Fast-ion transport studies using FIDA spectroscopy at the ASDEX Upgrade tokamak*. Phd thesis, LMU München, 2013. also IPP report 10/46. URL: http://edoc.ub.uni-muenchen.de/15367/.

[14] T. H. Stix. Heating of toroidal plasmas by neutral injection. *Plasma Physics*, 14(4):367, 1972. URL: http://stacks.iop.org/0032-1028/14/i=4/a=002.

[15] J. D. Huba. NRL: Plasma formulary. Technical report, DTIC Document, 2004.

[16] J. G. Cordey and W. G. F. Core. Energetic particle distribution in a toroidal plasma with neutral injection heating. *Physics of Fluids*, 17(8), 1974.

[17] R. J. Goldston, D. McCune, H. Towner, S. Davis, R. Hawryluk, and G. Schmidt. New techniques for calculating heat and particle source rates due to neutral beam injection in axisymmetric tokamaks. *Journal of computational physics*, 43(1):61–78, 1981.

[18] R. Fowler, J. Smith, and J. Rome. FIFPC - a Fast Ion Fokker-Planck Code. *Computer Physics Communications*, 13(5):323 – 340, 1978. URL: http://www.sciencedirect.com/science/article/pii/0010465578900309, doi:http://dx.doi.org/10.1016/0010-4655(78)90030-9.

[19] R. Hawryluk and et al. An Empirical Approach to Tokamak Transport. *in Physics of Plasmas Close to Thermonuclear Conditions*, 1:19–46, 1980.

[20] A. Pankin, D. McCune, R. Andre, G. Bateman, and A. Kritz. The tokamak Monte Carlo fast ion module NUBEAM in the National Transport Code Collaboration library. *Computer Physics Communications*, 159(3):157 – 184, 2004.

[21] C. Fiore, S. Medley, G. Hammett, R. Kaita, A. Roquemore, and S. Scott. Ion temperature from tangential charge exchange neutral analysis on the Tokamak Fusion Test Reactor. *Nuclear Fusion*, 28(8):1315, 1988. URL: http://stacks.iop.org/0029-5515/28/i=8/a=001.

[22] Y. Feng, B. Wolle, and K. Hübner. New, simplified technique for calculating particle source rates due to neutral beam injection into tokamaks. *Computer physics communications*, 88(2):161–172, 1995.

[23] M. Kraus. Heiz- und Stromprofile bei Neutralteilcheninjektion in Tokamakplasmen. Diplomarbeit, Technische Universität München, Germany, 2010.

[24] J. D. Gaffey. Energetic ion distribution resulting from neutral beam injection in tokamaks. *Journal of Plasma Physics*, 16:149–169, 10 1976. URL: http://journals.cambridge.org/article_S0022377800020134, doi:10.1017/S0022377800020134.

[25] M. Brambilla and R. Bilato. Simulation of ion cyclotron heating of tokamak plasmas using coupled Maxwell and quasilinear-Fokker-Planck solvers. *Nuclear Fusion*, 46(7):S387, 2006. URL: http://stacks.iop.org/0029-5515/46/i=7/a=S01.

[26] J. Wesson and D. J. Campbell. *Tokamaks*, volume 149. Oxford University Press, 2011.

[27] V. L. Yakimenko. Absorption of waves in a plasma (Quasilinear approximation). *Soviet Physics JETP*, 17(5), 1963.

[28] C. F. Kennel and F. Engelmann. Velocity space diffusion from weak plasma turbulence in a magnetic field. *Physics of Fluids*, 9(12):2377, 1966.

[29] T. H. Stix. Fast-wave heating of a two-component plasma. *Nuclear Fusion*, 15(5):737, 1975. URL: `http://stacks.iop.org/0029-5515/15/i=5/a=003`.

[30] T. H. Stix. *Waves in plasmas*. Springer Science & Business Media, 1992.

[31] M. Porkolab. Plasma heating by fast magnetosonic waves in Tokamaks. *AIP Conference Proceedings*, 314(1), 1994.

[32] J. C. Hosea. Foundations of ICRF heating - A historical perspective. *AIP Conference Proceedings*, 314(1), 1994.

[33] R. Dendy, R. Hastie, K. McClements, and T. Martin. A model for ideal m= 1 internal kink stabilization by minority ion cyclotron resonant heating. *Physics of Plasmas (1994-present)*, 2(5):1623–1636, 1995.

[34] Y. O. Kazakov, I. Pusztai, T. Fülöp, and T. Johnson. Poloidal asymmetries due to ion cyclotron resonance heating. *Plasma Physics and Controlled Fusion*, 54(10):105010, 2012. URL: `http://stacks.iop.org/0741-3335/54/i=10/a=105010`.

[35] J. Y. Hsu, V. S. Chan, R. W. Harvey, R. Prater, and S. K. Wong. Resonance Localization and Poloidal Electric Field due to Cyclotron Wave Heating in Tokamak Plasmas. *Phys. Rev. Lett.*, 53:564–567, Aug 1984. URL: `http://link.aps.org/doi/10.1103/PhysRevLett.53.564`, `doi:10.1103/PhysRevLett.53.564`.

[36] G. W. Hammett. *Fast ion studies of ion cyclotron heating in the PLT tokamak*. PhD thesis, Princeton University, 1986.

[37] M. Brambilla. Numerical simulation of ion cyclotron waves in tokamak plasmas. *Plasma Physics and Controlled Fusion*, 41(1):1, 1999.

[38] M. Brambilla. Quasi-linear ion distribution function during ion cyclotron heating in tokamaks. *Nuclear fusion*, 34(8):1121, 1994.

[39] R. Bilato, M. Brambilla, O. Maj, L. Horton, C. Maggi, and J. Stober. Simulations of combined neutral beam injection and ion cyclotron heating with the TORIC-SSFPQL package. *Nuclear Fusion*, 51(10):103034, 2011.

[40] M. Brambilla and R. Bilato. Advances in numerical simulations of ion cyclotron heating of non-Maxwellian plasmas. *Nuclear Fusion*, 49(8):085004, 2009.

[41] A. Herrmann and O. Gruber. ASDEX Upgrade-introduction and overview. *Fusion Science and Technology*, 44(3):569–577, 2003.

[42] R. Pitts, S. Carpentier, F. Escourbiac, T. Hirai, V. Komarov, S. Lisgo, A. Kukushkin, A. Loarte, M. Merola, A. S. Naik, R. Mitteau, M. Sugihara, B. Bazylev, and P. Stangeby. A full tungsten divertor for ITER: Physics issues and design status. *Journal of Nuclear Materials*, 438, Supplement:S48 – S56, 2013. Proceedings of the 20th International Conference on Plasma-Surface Interactions in Controlled Fusion Devices. URL: http://www.sciencedirect.com/science/article/pii/S0022311513000160, doi:http://dx.doi.org/10.1016/j.jnucmat.2013.01.008.

[43] T. Hirai, F. Escourbiac, S. Carpentier-Chouchana, A. Fedosov, L. Ferrand, T. Jokinen, V. Komarov, A. Kukushkin, M. Merola, R. Mitteau, R. Pitts, W. Shu, M. Sugihara, B. Riccardi, S. Suzuki, and R. Villari. ITER tungsten divertor design development and qualification program. *Fusion Engineering and Design*, 88(9–10):1798 – 1801, 2013. Proceedings of the 27th Symposium On Fusion Technology (SOFT-27); Liège, Belgium, September 24-28, 2012. URL: http://www.sciencedirect.com/science/article/pii/S0920379613004420, doi:http://dx.doi.org/10.1016/j.fusengdes.2013.05.010.

[44] H. Murmann, S. Götsch, H. Röhr, H. Salzmann, and K. H. Steuer. The Thomson scattering systems of the ASDEX upgrade tokamak. *Review of Scientific Instruments*, 63(10), 1992.

[45] R. Bartiromo, G. Bracco, M. Brusati, G. Grosso, S. Mantovani, B. Tilia, and V. Zanza. Design and calibration of the JET neutral particle analyzer. *Review of Scientific Instruments*, 58(5), 1987.

[46] P. A. Schneider, H. Blank, B. Geiger, K. Mank, S. Martinov, F. Ryter, M. Weiland, A. Weller, and the ASDEX Upgrade Team. A new compact solid-state neutral particle analyser at ASDEX Upgrade: Setup and physics modeling. *Review of Scientific Instruments*, 86(7), 2015. URL: http://scitation.aip.org/content/aip/journal/rsi/86/7/10.1063/1.4926886, doi:http://dx.doi.org/10.1063/1.4926886.

[47] G. Tardini, A. Zimbal, B. Esposito, F. Gagnon-Moisan, D. Marocco, R. Neu, H. Schuhmacher, and the ASDEX Upgrade Team. First neutron spectrometry measurements in the ASDEX Upgrade tokamak. *Journal of Instrumentation*, 7(03):C03004, 2012. URL: http://stacks.iop.org/1748-0221/7/i=03/a=C03004.

[48] M. Weiland, B. Geiger, A. S. Jacobsen, M. Reich, M. Salewski, T. Odstrčil, and the ASDEX Upgrade Team. Enhancement of the FIDA diagnostic at ASDEX Upgrade for velocity space tomography. *Plasma Physics and Controlled Fusion*, 58(2):025012, 2016. URL: http://stacks.iop.org/0741-3335/58/i=2/a=025012.

[49] A. Einstein. Zur Quantentheorie der Strahlung. *Physikalische Zeitschrift*, 18:121–128, 1917.

[50] M. Van Zeeland, J. Yu, N. Brooks, W. Heidbrink, K. Burrell, R. Groebner, A. Hyatt, T. Luce, N. Pablant, W. Solomon, et al. Active and passive spectroscopic imaging in the DIII-D tokamak. *Plasma Physics and Controlled Fusion*, 52(4):045006, 2010.

[51] M. Salewski, B. Geiger, D. Moseev, W. W. Heidbrink, A. S. Jacobsen, S. B. Korsholm, F. Leipold, J. Madsen, S. K. Nielsen, J. Rasmussen, M. Stejner, M. Weiland, and the ASDEX Upgrade Team. On velocity-space sensitivity of fast-ion D-alpha spectroscopy. *Plasma Physics and Controlled Fusion*, 56(10):105005, 2014. URL: http://stacks.iop.org/0741-3335/56/i=10/a=105005.

[52] B. Geiger, R. Dux, R. McDermott, S. Potzel, M. Reich, F. Ryter, M. Weiland, D. Wünderlich, ASDEX Upgrade team, and M. Garcia-Munoz. Multi-view fast-ion D-alpha spectroscopy diagnostic at ASDEX Upgrade. *Review of Scientific Instruments*, 84(11):113502, 2013.

[53] Y. Luo, W. W. Heidbrink, K. H. Burrell, D. H. Kaplan, and P. Gohil. Measurement of the D_α spectrum produced by fast ions in DIII-D. *Review of Scientific Instruments*, 78(3):–, 2007. URL: http://scitation.aip.org/content/aip/journal/rsi/78/3/10.1063/1.2712806, doi:http://dx.doi.org/10.1063/1.2712806.

[54] M. Podestà, W. W. Heidbrink, R. E. Bell, and R. Feder. The NSTX fast-ion D-alpha diagnostic. *Review of Scientific Instruments*, 79(10), 2008.

[55] M. Salewski, B. Geiger, S. Nielsen, H. Bindslev, M. García-Muñoz, W. Heidbrink, S. Korsholm, F. Leipold, F. Meo, P. Michelsen, D. Moseev, M. Stejner, G. Tardini, and the ASDEX Upgrade team. Tomography of fast-ion velocity-space distributions from synthetic CTS and FIDA measurements. *Nuclear Fusion*, 52(10):103008, 2012. URL: http://stacks.iop.org/0029-5515/52/i=10/a=103008.

[56] M. Salewski, B. Geiger, A. Jacobsen, M. García-Muñoz, W. Heidbrink, S. Korsholm, F. Leipold, J. Madsen, D. Moseev, S. Nielsen, J. Rasmussen, M. Stejner, G. Tardini, M. Weiland, and the ASDEX Upgrade Team. Measurement of a 2D fast-ion velocity distribution function by tomographic inversion of fast-ion D-alpha spectra. *Nuclear Fusion*, 54(2):023005, 2014. URL: http://stacks.iop.org/0029-5515/54/i=2/a=023005.

[57] M. Salewski, B. Geiger, W. W. Heidbrink, A. S. Jacobsen, S. B. Korsholm, F. Leipold, J. Madsen, D. Moseev, S. K. Nielsen, J. Rasmussen, L. Stagner, D. Steeghs, M. Stejner, G. Tardini, and M. Weiland. Doppler tomography in fusion plasmas and astrophysics. *Plasma Physics and Controlled Fusion*, 57(1):014021, 2015. URL: http://stacks.iop.org/0741-3335/57/i=1/a=014021.

[58] A. S. Jacobsen, L. Stagner, M. Salewski, B. Geiger, W. W. Heidbrink, S. B. Korsholm, F. Leipold, S. K. Nielsen, J. Rasmussen, M. Stejner, H. Thomsen, M. Weiland, and the ASDEX Upgrade team. Inversion methods for fast-ion velocity-space tomography in fusion plasmas. *Plasma Physics and Controlled Fusion*, 58(4):045016, 2016. URL: http://stacks.iop.org/0741-3335/58/i=4/a=045016.

[59] M. Anton, H. Weisen, M. J. Dutch, W. von der Linden, F. Buhlmann, R. Chavan, B. Marletaz, P. Marmillod, and P. Paris. X-ray tomography on the TCV tokamak. *Plasma Physics and Controlled Fusion*, 38(11):1849, 1996. URL: http://stacks.iop.org/0741-3335/38/i=11/a=001.

[60] B. Geiger, M. Weiland, A. Mlynek, M. Reich, A. Bock, M. Dunne, R. Dux, E. Fable, R. Fischer, M. Garcia-Munoz, J. Hobirk, C. Hopf, S. Nielsen, T. Odstrcil, C. Rapson, D. Rittich, F. Ryter, M. Salewski, P. A. Schneider, G. Tardini, and M. Willensdorfer. Quantification of the impact of large and small-scale instabilities on the fast-ion confinement in ASDEX Upgrade. *Plasma Physics and Controlled Fusion*, 57(1):014018, 2015. URL: http://stacks.iop.org/0741-3335/57/i=1/a=014018.

[61] J. A. Lovberg, W. W. Heidbrink, J. D. Strachan, and V. S. Zaveryaev. Neutron sawtooth behavior in the PLT, DIII-D, and TFTR tokamaks. *Physics of Fluids B: Plasma Physics*, 1(4):874–892, 1989. URL: http://link.aip.org/link/?PFB/1/874/1, doi:10.1063/1.859012.

[62] Y. Kolesnichenko and Y. Yakovenko. Theory of fast ion transport during sawtooth crashes in tokamaks. *Nuclear Fusion*, 36(2):159, 1996. URL: http://stacks.iop.org/0029-5515/36/i=2/a=I04.

[63] Y. I. Kolesnichenko, V. V. Lutsenko, Y. V. Yakovenko, and G. Kamelander. Theory of fast ion transport induced by sawtooth oscillations: Overview and new results. *Physics of Plasmas*, 4(7), 1997.

[64] F. Jaulmes, E. Westerhof, and H. de Blank. Redistribution of fast ions during sawtooth reconnection. *Nuclear Fusion*, 54(10):104013, 2014. URL: http://stacks.iop.org/0029-5515/54/i=10/a=104013.

[65] B. B. Kadomtsev. On disruptive instability in tokamaks. *Soviet Journal of Plasma Physics*, 1:710–715, October 1975.

[66] J. W. Connor and R. J. Hastie. The effect of shaped plasma cross sections on the ideal internal kink mode in a tokamak. Technical Report CLM-M106, Culham Laboratory, 1985.

[67] M. Schittenhelm and H. Zohm. Analysis of coupled MHD modes with Mirnov probes in ASDEX Upgrade. *Nuclear Fusion*, 37(9):1255, 1997. URL: http://stacks.iop.org/0029-5515/37/i=9/a=I06.

[68] H. Zohm. MHD-Gleichgewichte und Stabilität heißer Fusionsplasmen. Vorlesungsskript, IPP Garching/LMU München, 2004.

[69] F. Porcelli, E. Rossi, G. Cima, and A. Wootton. Macroscopic Magnetic Islands and Plasma Energy Transport. *Phys. Rev. Lett.*, 82:1458–1461, Feb 1999. URL: http://link.aps.org/doi/10.1103/PhysRevLett.82.1458, doi:10.1103/PhysRevLett.82.1458.

[70] B. Geiger, M. Weiland, A. Jacobsen, D. Rittich, R. Dux, R. Fischer, C. Hopf, M. Maraschek, R. McDermott, S. Nielsen, T. Odstrcil, M. Reich, F. Ryter, M. Salewski, P. Schneider, and G. Tardini. Fast-ion transport and neutral beam current drive in ASDEX Upgrade. *Nuclear Fusion*, 55(8):083001, 2015. URL: http://stacks.iop.org/0029-5515/55/i=8/a=083001.

[71] L. Zakharov, B. Rogers, and S. Migliuolo. The theory of the early nonlinear stage of m=1 reconnection in tokamaks. *Physics of Fluids B*, 5(7), 1993.

[72] D. Pfefferlé, J. Graves, W. Cooper, C. Misev, I. Chapman, M. Turnyanskiy, and S. Sangaroon. NBI fast ion confinement in the helical core of MAST hybrid-like plasmas. *Nuclear Fusion*, 54(6):064020, 2014. URL: `http://stacks.iop.org/0029-5515/54/i=6/a=064020`.

[73] L. Chen and F. Zonca. Theory of Alfvén waves and energetic particle physics in burning plasmas. *Nuclear Fusion*, 47(10):S727, 2007. URL: `http://stacks.iop.org/0029-5515/47/i=10/a=S20`.

[74] N. Gorelenkov, H. Berk, R. Budny, C. Cheng, G.-Y. Fu, W. Heidbrink, G. Kramer, D. Meade, and R. Nazikian. Study of thermonuclear Alfvén instabilities in next step burning plasma proposals. *Nuclear Fusion*, 43(7):594, 2003. URL: `http://stacks.iop.org/0029-5515/43/i=7/a=313`.

[75] W. Heidbrink. Basic physics of Alfvén instabilities driven by energetic particles in toroidally confined plasmas. *Physics of Plasmas (1994-present)*, 15(5):055501, 2008.

[76] L. Rayleigh. XVII. On the maintenance of vibrations by forces of double frequency, and on the propagation of waves through a medium endowed with a periodic structure. *The London, Edinburgh, and Dublin Philosophical Magazine and Journal of Science*, 24(147):145–159, 1887.

[77] G. Y. Fu and J. W. Van Dam. Excitation of the toroidicity-induced shear Alfvén eigenmode by fusion alpha particles in an ignited tokamak. *Physics of Fluids B Plasma Physics*, 1(10):1949, 1989.

[78] K. T. et al. MHD instabilities and their effects on plasma confinement in Large Helical Device plasmas. *Nuclear Fusion*, 44(2):217, 2004. URL: `http://stacks.iop.org/0029-5515/44/i=2/a=001`.

[79] T. J. J. Tala, V. V. Parail, A. Becoulet, C. D. Challis, G. Corrigan, N. C. Hawkes, D. J. Heading, M. J. Mantsinen, S. Nowak, and contributors to the EFDA-JET work programme. Impact of different heating and current drive methods on the early shape q -profile evolution in JET. *Plasma Physics and Controlled Fusion*, 44(7):1181, 2002. URL: `http://stacks.iop.org/0741-3335/44/i=7/a=309`.

[80] B. N. Breizman, M. S. Pekker, S. E. Sharapov, and J. E. contributors. Plasma pressure effect on Alfvén cascade eigenmodes. *Physics of Plasmas*, 12(11), 2005. URL: `http://scitation.aip.org/content/aip/journal/pop/12/11/10.1063/1.2130692`, `doi:http://dx.doi.org/10.1063/1.2130692`.

[81] M. Garcia-Munoz, I. Classen, B. Geiger, W. Heidbrink, M. V. Zeeland, S. Äkäslompolo, R. Bilato, V. Bobkov, M. Brambilla, G. Conway, S. da Graça, V. Igochine, P. Lauber, N. Luhmann, M. Maraschek, F. Meo, H. Park, M. Schneller, G. Tardini, and the ASDEX Upgrade Team. Fast-ion transport induced by Alfvén eigenmodes in the ASDEX Upgrade tokamak. *Nuclear Fusion*, 51(10):103013, 2011. URL: `http://stacks.iop.org/0029-5515/51/i=10/a=103013`.

[82] D. W. Swain and R. H. Goulding. ITER ion cyclotron system: Overview and plans. *Fusion Engineering and Design*, 82(5):603–609, 2007.

[83] W. Heidbrink and G. Sadler. The behaviour of fast ions in tokamak experiments. *Nuclear Fusion*, 34(4):535, 1994. URL: http://stacks.iop.org/0029-5515/34/i=4/a=I07.

[84] W. W. Heidbrink, Y. Luo, K. H. Burrell, R. W. Harvey, R. I. Pinsker, and E. Ruskov. Measurements of fast-ion acceleration at cyclotron harmonics using Balmer-alpha spectroscopy. *Plasma Physics and Controlled Fusion*, 49(9):1457, 2007. URL: http://stacks.iop.org/0741-3335/49/i=9/a=008.

[85] J. Hosea, S. Bernabei, P. Colestock, S. Davis, P. Efthimion, R. Goldston, D. Hwang, S. Medley, D. Mueller, J. Strachan, et al. Fast-wave heating of two-ion plasmas in the Princeton Large Torus through minority-cyclotron-resonance damping. *Physical Review Letters*, 43(24):1802, 1979.

[86] C. Hellesen, M. G. Johnson, E. A. Sundén, S. Conroy, G. Ericsson, E. Ronchi, H. Sjöstrand, M. Weiszflog, G. Gorini, M. Tardocchi, T. Johnson, V. Kiptily, S. Pinches, S. Sharapov, and J.-E. Contributors. Neutron emission generated by fast deuterons accelerated with ion cyclotron heating at JET. *Nuclear Fusion*, 50(2):022001, 2010. URL: http://stacks.iop.org/0029-5515/50/i=2/a=022001.

[87] D. Darrow, C.-S. Chang, S. Zweben, R. Budny, H. Herrmann, E. Jaeger, R. Majeski, M. Murakami, C. Phillips, J. Rogers, G. Schilling, J. Stevens, and J. Wilson. ICRF-induced DD fusion product losses in TFTR. *Nuclear Fusion*, 36(1):1, 1996. URL: http://stacks.iop.org/0029-5515/36/i=1/a=I01.

[88] V. Kiptily, F. Cecil, O. Jarvis, M. Mantsinen, S. Sharapov, L. Bertalot, S. Conroy, L. Ingesson, T. Johnson, K. Lawson, S. Popovichev, and contributors to the EFDA-JET Workprogramme. γ-ray diagnostics of energetic ions in JET. *Nuclear Fusion*, 42(8):999, 2002. URL: http://stacks.iop.org/0029-5515/42/i=8/a=308.

[89] V. Kiptily, J. Adams, L. Bertalot, A. Murari, S. Sharapov, V. Yavorskij, B. Alper, R. Barnsley, P. de Vries, C. Gowers, L.-G. Eriksson, P. Lomas, M. Mantsinen, A. Meigs, J.-M. Noterdaeme, F. Orsitto, and J. E. contributors. Gamma-ray imaging of D and 4 He ions accelerated by ion-cyclotron-resonance heating in JET plasmas. *Nuclear Fusion*, 45(5):L21, 2005. URL: http://stacks.iop.org/0029-5515/45/i=5/a=L01.

[90] H. Bindslev, S. K. Nielsen, L. Porte, J. A. Hoekzema, S. B. Korsholm, F. Meo, P. K. Michelsen, S. Michelsen, J. W. Oosterbeek, E. L. Tsakadze, E. Westerhof, and P. Woskov. Fast-Ion Dynamics in the TEXTOR Tokamak Measured by Collective Thomson Scattering. *Phys. Rev. Lett.*, 97:205005, Nov 2006. URL: http://link.aps.org/doi/10.1103/PhysRevLett.97.205005, doi:10.1103/PhysRevLett.97.205005.

[91] M. Salewski, B. Geiger, S. Nielsen, H. Bindslev, M. García-Muñoz, W. Heidbrink, S. Korsholm, F. Leipold, J. Madsen, F. Meo, P. Michelsen, D. Moseev, M. Stejner, G. Tardini, and the ASDEX Upgrade Team. Combination of fast-ion diagnostics in velocity-space tomographies. *Nuclear Fusion*, 53(6):063019, 2013. URL: http://stacks.iop.org/0029-5515/53/i=6/a=063019.

[92] A. Jacobsen, M. Salewski, B. Geiger, S. Korsholm, F. Leipold, S. Nielsen, J. Rasmussen, M. Stejner, and M. Weiland. Benchmark and combined velocity-space tomography of fast-ion D-alpha spectroscopy and collective Thomson scattering measurements. *Plasma Physics and Controlled Fusion*, 58(4):042002, 2016. URL: http://stacks.iop.org/0741-3335/58/i=4/a=042002.

[93] S. Pinches, L. Appel, J. Candy, S. Sharapov, H. Berk, D. Borba, B. Breizman, T. Hender, K. Hopcraft, G. Huysmans, and W. Kerner. The HAGIS self-consistent nonlinear wave-particle interaction model. *Computer Physics Communications*, 111(1–3):133 – 149, 1998. URL: http://www.sciencedirect.com/science/article/pii/S0010465598000344, doi:http://dx.doi.org/10.1016/S0010-4655(98)00034-4.

[94] P. Lauber, S. Günter, A. Könies, and S. Pinches. LIGKA: A linear gyrokinetic code for the description of background kinetic and fast particle effects on the MHD stability in tokamaks. *Journal of Computational Physics*, 226(1):447 – 465, 2007. URL: http://www.sciencedirect.com/science/article/pii/S0021999107001660, doi:http://dx.doi.org/10.1016/j.jcp.2007.04.019.

[95] M. Brüdgam. *Nonlinear Effects of Energetic Particle Driven Modes in Tokamaks*. PhD thesis, Technische Universität München, 2010.

[96] M. Schneller, P. Lauber, M. García-Muñoz, M. Brüdgam, and S. Günter. Nonlinear alfvénic fast particle transport and losses. *Journal of Physics: Conference Series*, 401(1):012022, 2012. URL: http://stacks.iop.org/1742-6596/401/i=1/a=012022.

[97] M. Schneller, P. Lauber, R. Bilato, M. García-Muñoz, M. Brüdgam, S. Günter, and the ASDEX Upgrade Team. Multi-mode Alfvénic fast particle transport and losses: numerical versus experimental observation. *Nuclear Fusion*, 53(12):123003, 2013. URL: http://stacks.iop.org/0029-5515/53/i=12/a=123003.